Modelling salt intrusion in an estuarine tidal network

Inge van Tongeren

Supervisor: H.E. de Swart

July 2019

Abstract

An estuary is a semi-enclosed body of water, in which fresh water, from rivers and salt water, originating from the ocean, meet. In an estuarine tidal network this occurs in multiple branches. Understanding (the processes influencing) salt intrusion in tidal networks is of major importance, due to its effects on ecosystems and because of the problems salt intrusion can cause for the availability of fresh water and agriculture. There are various studies that use numerical simulation models to reproduce realistic salinity profiles, however in order to gain more fundamental knowledge more simple, semi-analytical models are needed.

In this study an idealised, tidally averaged model (originally formulated for a single channel configuration) is generalized to an estuarine network. This model describes export of salt by river flow and import of salt by density-driven flow and horizontal diffusion. Besides the distribution of salt and salt transport between the channels, the model also calculates the distribution of river water over the different channels. The model is used to investigate the effect of different factors, such as tidal velocity, river flow and channel geometry on salt intrusion. The model is applied to a prototype estuarine network consisting of the South Channel, South Passage and North Passage of the Yangtze Estuary.

It is concluded that, for the present-day situation, dry season and spring tide, salt intrusion is larger in the South Passage than in the North Passage. The most important reason for this is that the South Passage is funnel-shaped and the North Passage is straight. Due to the funnel-shape, river flow is weaker near the ocean as the river transport is distributed over a larger area there. The larger salt intrusion in the South Passage results in a salt transport from the South Passage to the North Passage. Furthermore, it is found that there is slightly more river transport through the South Passage than through the North Passage (except for high river discharge during neap tide). These findings generally agree with field data and results from numerical studies. A noticeable difference is that the model underestimates salt intrusion and stratification.

It was found that the river transport in all channels decreases, when river discharge decreases. This leads to a larger salt intrusion in the South Passage and North Passage, as less salt is transported away by river flow. Likewise, salt transport from the South Passage to the North Passage increases for decreasing river discharge. This is explained by the increase in salt intrusion in the South Passage.

Furthermore, salt intrusion generally increases when tidal currents increase, due to an increase in horizontal diffusion. An exception to this relation is the situation with high river discharge. For this situation, in the North Passage, more salt intrusion is found for neap tide than for spring tide, due to a stronger density-driven flow during neap tide. Net salt transport from the South Passage to the North Passage practically disappears during neap tide. This is explained by the weaker salt intrusion in the South Passage during neap tide.

Finally the effect of the Deepwater Navigation Channel (DNC) on salt dynamics has been investigated. Only geometric changes due to the DNC are taken into account and low river discharge during spring tide is considered. Before the DNC, the North Passage had a funnel-shape and was 1 m shallower than it is today. A smaller river transport through the North Passage was found for the present-day situation than before the DNC. The reason is that there is less space for river water in the North Passage nowadays. Moreover, the straightening of the North Passage also caused a decrease in salt intrusion. This decrease in salt intrusion is larger for the North passage than for the South Passage. In the North Passage, this decrease in salt intrusion is explained by an increase in river flow, as the river transport has to flow through a smaller surface area near the ocean. In the South Passage an increase in river transport lead to the decrease in salt intrusion. The decrease in salt intrusion, due to the DNC, results in a decrease in salt transport from the South Passage to the North Passage.

Contents

Chapter 1

Introduction

1.1 Overall context

This study examines the problem of salt intrusion in an estuarine tidal network. First, it will be explained what an estuarine network is and why this problem is important. To begin with, estuaries are systems near the coast were fresh water (originating from for example a river) and salt water imported from the sea meet (see *Chen* [2018]). A sketch of an estuary is given in in Figure 1.1a. There are multiple definitions of an estuary. A definition that is often used is that of *Cameron and Pritchard* [1963]. They define an estuary as "a semi-enclosed body of water which has a free connection with the open sea and within which sea water is measurably diluted with fresh water derived from land drainage". This definition holds for temperate estuaries, where freshwater input is provided by rivers (see *Geyer* [2010] and *Chen* [2018] for more information). The most important source of mixing is generated by tidal currents moving over the rough bottom (see e.g. *Geyer* [2010]). Estuaries can be well mixed, partially mixed or strongly stratified, depending on the strength of the river discharge (see *Valle-Levinson* [2010] for more details). Examples of estuaries are the Thames estuary, the Chesapeake Bay and the Columbia river estuary in the United States (see Figure 1.1b).

Figure 1.2 schematically shows the physics behind the subtidal (that is tidally-averaged) flow in a single channel estuary. At the landward boundary of the estuary, the river provides a fresh water flow into the estuary. Due to the low density of this water, it tends to stay close to the surface. The tidally averaged surface height is larger near the river and smaller near the sea and because the system tries to flatten this gradient, there will be a fresh water flow seaward (left dark blue arrow in the figure). On the sea side pressure increases faster from the

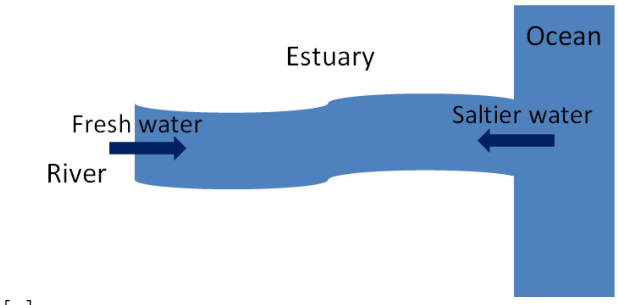

[a]

[b]

Figure 1.1: Sketch of an estuary ([a]) and the Columbia river estuary in the United States ([b]). The map of the Columbia river estuary originate from *Bourrichon* (`https://commons.wikimedia.org/wiki/File:Columbia_estuary_map-fr.svg`).

surface to the bottom than on the river side.[1] This results in an baroclinic pressure gradient that is zero at the surface and increases towards the bottom. Due to this pressure gradient seawater is forced into the estuary and there is a landward flow of relatively salt water near the bottom of the estuary (right dark blue arrow in the figure). The river flow and the density driven flow (the flow driven by horizontal density gradient, also called the exchange flow) together form the gravitational circulation (see *Valle-Levinson* [2011]). For more information on the gravitational circulation, see *Geyer and MacCready* [2014] and *Geyer* [2010].

In an estuarine network the river water flows trough different branches that make up the total estuarine system (see *Alebregtse and de Swart* [2016]). Examples of such estuarine networks are the Amazon estuary (Brasil), the Pearl river

[1] This can be understood by considering hydrostatic balance ($\frac{\partial p}{\partial z} = -\rho g$, see *Cushman-Roisin and Beckers* [2011]) and taking into account that the density of water is larger near the sea.

estuary (China), the Berau estuary (Indonesia), the Rhine and Meuse estuary (the Netherlands) and the Yangtze estuary (China). The last two estuarine networks are shown in Figure 1.3.

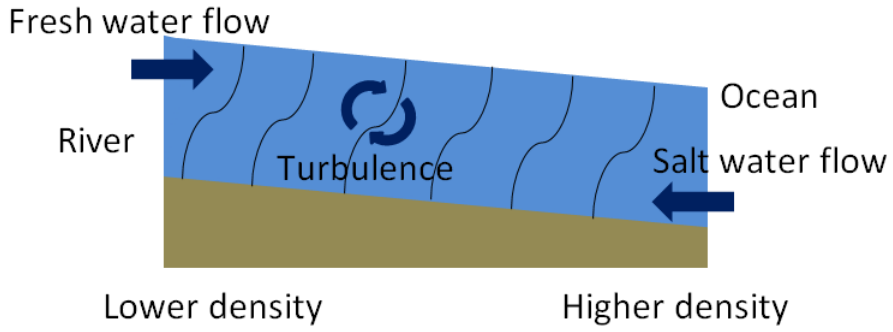

Figure 1.2: Schematic figure illustrating the gravitational circulation. Near the landward boundary of the estuary there is freshwater, with a lower density, that is provided by the river. Near the seaward boundary there is saltier water, with a higher density, provided by the sea. The slope in the sea surface results in a barotropic pressure gradient that drives a seaward fresh water flow (left dark blue arrow). Near the bottom there is a landward flow of saltier water (right dark blue arrow), driven by a baroclinic pressure gradient. Turbulence (caused by the tides, bent dark blue arrows) provides mixing of saltier water and fresher water. Black bent lines indicate lines of equal density. The river flow and the density driven flow together form the gravitational circulation (see *Valle-Levinson* [2011]).

In estuaries and estuarine networks, salt penetrates from the ocean into the estuary. This process is called salt intrusion and is often measured using a intrusion length. Mostly, the intrusion length is defined as the distance between the coast and the most landward location of a surface of a certain constant salinity (e.g. the river salinity, see *Savenije* [1993], or a number such as 1 psu). This is illustrated in Figure 1.4.

Figure 1.5 contains processes that provide a net horizontal transport of salt. First, river flow exports salt out of the estuary, as this flow is in landward direction at any depth (see *Geyer and MacCready* [2014]). Secondly, density driven flow generates import of salt into the estuary (see *Geyer* [2010] and *MacCready* [2004]). Density driven flow vanishes when averaged over depth. However, this flow is landward near the bottom and where more salt is present than close to the surface

[a] 

[b] 

Figure 1.3: Two examples of an estuarine network, viz. the Rhine Meuse estuary ([a]) and the Yangtze estuary ([b]). The figures originate from *Dörrbecker* (`https://commons.wikimedia.org/wiki/File:Map_of_the_annual_average_discharge_of_Rhine_and_Maas_2000-2011_(EN).png`, [a]) and *NASA* (`https://commons.wikimedia.org/wiki/File:Shanghai_Landsat-7_2005-08-15.jpg`, [b], the figure is slightly adapted).

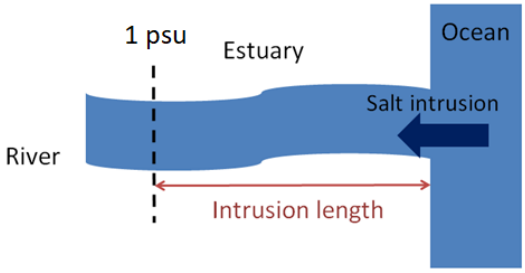

Figure 1.4: Figure illustrating the definition of the intrusion length.

(see *Geyer* [2010]). Another term providing import of salt is horizontal diffusion. Horizontal diffusion increases linearly with horizontal salinity gradient (see *MacCready* [2004] and *Guha and Lawrence* [2013]). The last term providing import of salt is tidal pumping, which can be explained as follow: during flood salt water from the ocean is transported into the estuary. There, due to e.g. turbulence, it

mixes with fresher water which is present near the head of the estuary. During ebb part of the mixed water leaves the estuary, so water leaving the estuary during ebb has a lower salinity than water entering the estuary during flood. For this reason tidal pumping causes import of salt into the estuary[2] (see *Dyer* [1997] and *Uncles et al.* [1985] for more information).

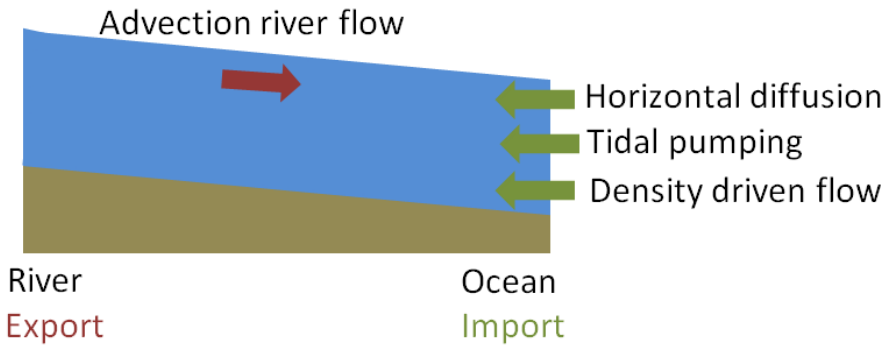

Figure 1.5: Figure illustrating the different processes that provide net horizontal salt transport. Horizontal diffusion, tidal pumping and the density-driven flow are import terms (green arrows), they increase salt intrusion. Advection of salt by river flow is an export term (red arrow).

It is good to realise that, different important topics in the problem of salt intrusion influence each other. This is illustrated in Figure 1.6. The important topics are turbulence, salinity and subtidal current. The gravitational circulation describes the physics behind the subtidal current. It consists of a density driven flow and a river flow (see *Valle-Levinson* [2011]). The eddy viscosity gives the strength of internal friction and thereby determines the strength of turbulence[3]. Diffusion coefficients give the strength of turbulent mixing of salinity[4]. Both the eddy viscosity and the diffusion coefficients decrease for increasing stratification (see *Dyer* [1997]). All the important topics influence each other. Firstly, subtidal current influences turbulence via the eddy viscosity. On its turn turbulence weakens stratification and therefore weakens the gravitational circulation (see *Monismith et al.* [1996]). Secondly, advection of salt by the subtidal current influences salinity, but, as salinity gradients are responsible for density driven flow (see *Geyer* [2010] and

[2]It is reasonable to assume that approximately the same volume of water is transported during ebb as during flood.

[3]See e.g. `http://www.mit.edu/course/1/1.061/www/dream/SEVEN/SEVENTHEORY.PDF`.

[4]See e.g. `https://www.merriam-webster.com/dictionary/diffusion%20coefficient`.

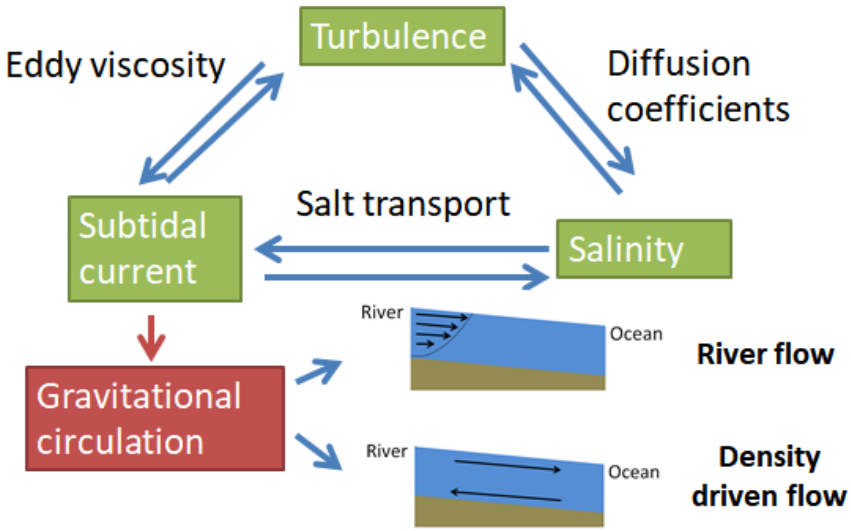

Figure 1.6: Figure showing important topics in the problem of salt intrusion and how these topics influence each other. The important topics are turbulence, salinity and subtidal current. The gravitational circulation describes the physics behind the subtidal current. The eddy viscosity gives the strength of internal friction and thereby determines the strength of turbulence. Diffusion coefficients give the strength of turbulent mixing of salinity. The gravitational circulation consists of a density driven flow and a river flow. All the important topics influence each other. Firstly, subtidal current influences turbulence via the eddy viscosity and on its turn turbulence weakens the density driven flow. Secondly, advection of salt by the subtidal current influences salinty, but, salinity gradients are responsible for density driven flow as well (see *Geyer* [2010] for more information). Lastly, turbulence influences salinity by mixing, but salinity affects turbulence via the diffusion coefficient.

Monismith et al. [1996]), salinity also influences subtidal current. Lastly, turbulence influences salinity by mixing, but salinity affects the turbulence as well via the diffusion coefficient (see *Dyer* [1997]).

1.2 Relevance

Understanding salt intrusion is of great importance, due to its influence on ecosystems (see *Sun et al.* [2009]). The possibly damaging effects of salt intrusion on ecosystems is illustrated in Figure 1.7. This figure shows a 'ghost forest'. At this place there used to be a living forest, but now only dead trees and a lot of salt is left (see *Webster* [2007] for more information).

Salt intrusion can also cause problems for the availability of fresh water (*Zhang et al.* [2011]) needed as for example drinking water or for agriculture. For instance the Yangtze Estuary contains a reservoir that provides more than 70% of the fresh-water of Shanghai (with 13 million inhabitants, see *Zhu et al.* [2018]).

Sea level rise and human made engineering projects influence salt intrusion (see for instance *Zhu et al.* [2018]). An example of such an engineering project is the Deep Waterway Project (DWP) in the Yangtze estuary. In this project one of the channels was deepened and straightened (before the project, the channel had a funnel-shape, with a greater width near the sea and a smaller width at the landward end of the channel). These geometrical changes, together with the construction of training walls, are convered by the Deepwater Navigation Channel (DNC, is part of the DWP). Also, other engineering structures were build, such as jetties and groins (see *Jiang et al.* [2012] for detailed information). Furthermore, intrusion lengths are influenced by natural variability. Examples are variability in river discharge (due to seasonal variations or events) or variability in intensity of mixing[5] (caused by the spring-neap or the tides themselves). Due to arguments mentioned above, it is very useful to understand the effect of different factors on the salt distribution in estuaries better.

Figure 1.7: Picture of a ghost forest in Terrebonne Parish (Louisiana, USA). Figure from *Webster* [2007].

[5]See e.g. *Zhu et al.* [2018] for research on the effect of river discharge and the spring-neap cycle on salt intrusion.

1.3 Approaches

In order to increase understanding of salt intrusion, different methods are used. One method is making and analyzing measurements. Measurements of salinity in estuaries are found in e.g. *Savenije* [2012]. Another option is to use models. One class of model that are regularly used are simulation models. An example of results for salinity distribution from such a model is shown in Figure 1.8a, which contains results from the study by *Zhu et al.* [2018] about the Yangtze estuary. The results in this figure are rather detailed and these kind of models are very suitable for making realistic simulations of the salinity distribution. However, for the goal of studying the underlying physical processes, these models might not be the best choice as they are slow, expansive and difficult to interpret physically. Also, there are still challenges to be solved concerning these models. For instance, *Kärnä et al.* [2015] showed for a certain model (SELFE) that it can reproduce the timing of events of salt intrusion correctly, however in the model salinity fields are smoothed as a result of numerical mixing. This results in an underestimation of gravitational circulation of salinity.

For improving simulation models it is useful to obtain more understanding of the underlying processes that result in salt intrusion. For this, idealised models are useful tools. The results of these models are less detailed, but the advantage of these models is that they provide insight into the physics. Furthermore, they are fast, so it costs less money and time to do a run. Some of these models are semi-empirical. An example of such a model is described in *Savenije* [1986]. However, this model is averaged over cross-section and tides, is based a lot on parametrisations (developed using measurements) and no gravitational circulation is described in the model. For this reason this model might not be the best candidate for gaining insight into the physics of an estuary. Other idealised models are semi-analytical, for example the model by *MacCready* [2004]. Results from this model, for the Salinity in the Northern San Francisco Bay, are shown in Figure 1.8b. The results of this model are less detailed than the results by *Zhu et al.* [2018] (see Figure 1.8). The model by *MacCready* [2004] is two-dimensional, width-averaged and tidally averaged (it does not include explicit tides), but does include an explicit description of the gravitational circulation and is more suitable for gaining physical insight than the models mentioned earlier in this section. Another semi-analytical model is the model by *McCarthy* [1993]. This model was made for well-mixed estuaries, is also two-dimensional, but does include an explicit description of tides. The model by *Wei et al.* [2017] also contains explicit tides and is made for well-mixed estuaries, but this model is three-dimensional. Semi-analytical, idealised models have been successfully applied to single channels (see *MacCready* [2004]), but the application to estuarine network is not (often) done yet.

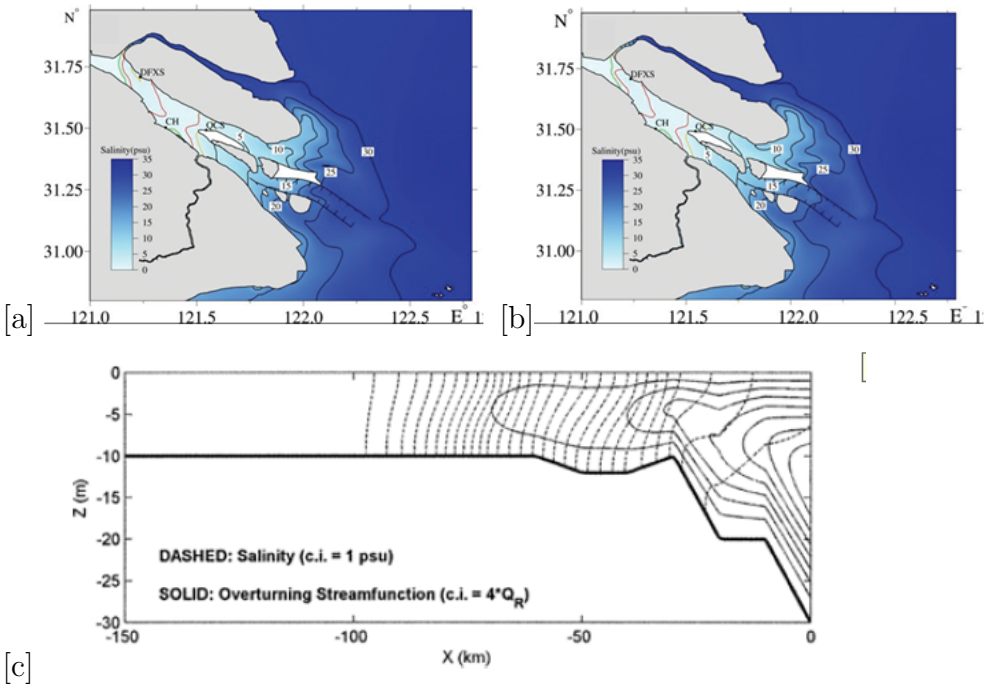

Figure 1.8: Salinity distribution in the surface layer ([a]) found in the study by *Zhu et al.* [2018] (adapted from Figure 10 in this study), who used a complex simulation model. From *Zhu et al.* [2018], the salinity distribution for the bottom layer ([b]) is shown as well (also adapted from Figure 10 in this study). These figures are compared with results found by *MacCready* [2004], who used an idealised model. The dashed lines in indicates the salinity distribution (and the solid line a streamfunction).

1.4 Research questions and methodology

The goal of this project is to understand more about the effect of different factors (such as channel geometry, tidal current, river discharge and man made engineering projects) on salt distribution and salt intrusion. In order to reach this goal an idealised model is made and used for experiments. As idealised models are (almost) only applied to single channel estuaries, in this project an idealised model will be generalized for a network configuration. In the first place it will be examined how this model performs in case of the network configuration similar to the Yangtze Estuary. Therefore, the first question of this project is *How does the idealised model perform in case of an estuarine network that consists of multiple channels?* The second question that will be addressed is *How do results depend on key parameters in such a system (such as river discharge, tidal forcing, geometrical characteristics of the network)?*

The model that is chosen to use for this project is the model by *MacCready* [2004]. As this model is relatively quick to run, contains a large part of the physics (in estuaries) that is described in this section and the model is convenient for physical interpretation. By choosing this model, it is chosen to only consider the two-dimensional case, to consider the width- and tidally-averaged case, not to take tidal pumping into account and to use simple parametrisations for modeling turbulence. This model is suitable for partially mixed and well mixed estuaries. First (in Chapter 2) the model(equations) will be described together with some important characteristics of the Yangtze estuary. Thereafter (in Chapter 3), the results of the reference case will be discussed. For the reference case, low river discharge during spring tide is considered for the present-day situations. Thereafter, the sensitivity of the results to tides, river discharge and human interventions is studied. The results are discussed in Chapter 4. After the results, the discussion will follow (in Chapter 5). In this chapter, the choice for a particular formulation for the eddy viscosity and the vertical diffusion coefficient will be discussed. Finally, the conclusions of the project are given (in Chapter 6).

Chapter 2

Method

2.1 Model equations

In this MSc thesis, an idealized, semi-analytical model is used to study an estuarine tidal network, that bears similarities to the Yangtze Estuary. Figure 2.1a shows a map of the Yangtze Estuary. The model made during this study consists of three channels; the South Channel, the South Passage and the North Passage. The seaward and the landward boundaries of this system are indicated with blue striped lines on the map in Figure 2.1a. The branching point that is considered in the model is indicated with a blue arrow. The map reveals that the South Passage is funnel-shaped (it has a smaller width near the branching point and a larger width near the ocean), while the North Passage and the South Channel are almost straight. Note that on this map the training walls along the North Passage are visible that are part of the Deepwater Navigation Channel (see *Alebregtse and de Swart* [2016]). A sketch of the network configuration in the model is shown in Figure 2.1b. The branching point is chosen at x =0 and the seaward and landward boundaries are indicated by $x = L_{sea,2}$ or $L_{sea,3}$ and L_{river}, respectively (all x-coordinates are written in green in the figure). The positive direction of x is chosen seaward and the vertical coordinate, z, such that $z = -H$ at the bottom and $z = \eta$ at the surface (η is the tidally averaged sea surface height and the positive direction of z is upward). It is chosen to define $z = 0$ at the sea surface on the seaward boundary.[1]

[1]It is assumed that η at the seaward boundary is the same for the South Passage and the North Passage (the two smaller channels in the model).

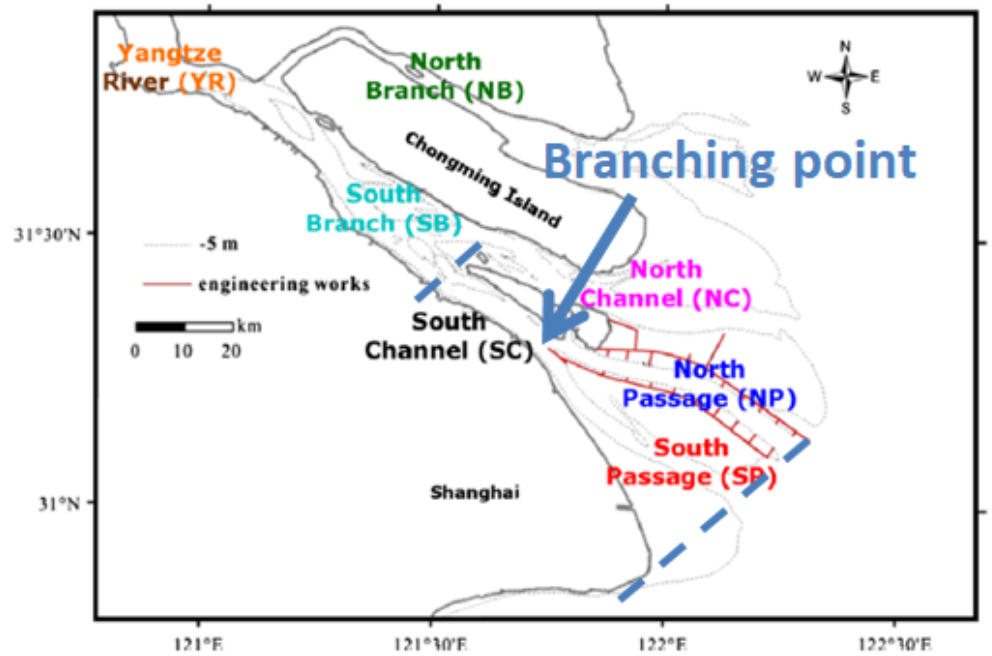

[a]

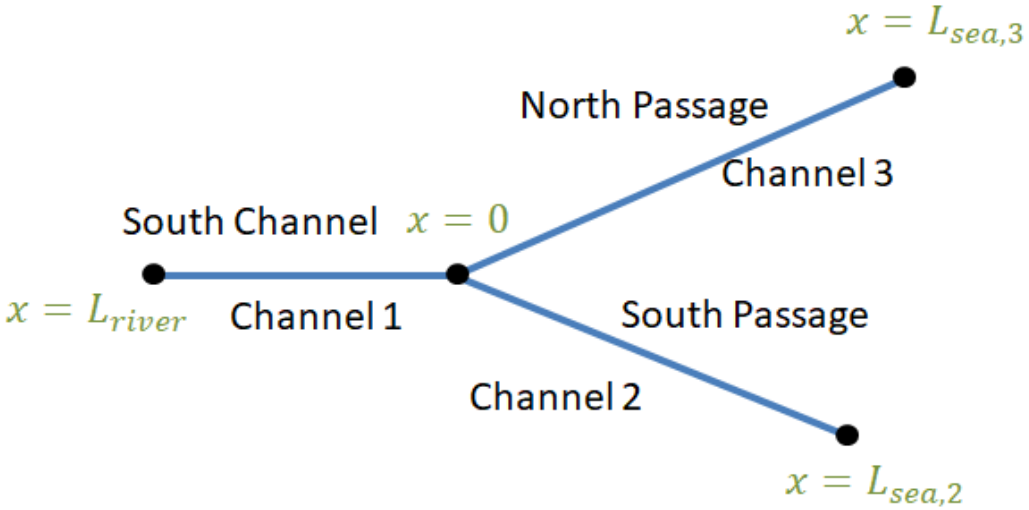

[b]

Figure 2.1: Map of the Yangtze Estuary ([a]). The model in this studies consists of three channels the South Channel, South Passage and North Passage. The blue striped lines indicate the approximate chosen location of the landward and seaward end of the network in the model. The blue arrow indicates the branching point that is considered in this studies. A sketch of the network system in the model is given in panel b. For every black dot, a x-coordinate is defined (written in green). Map adapted from *Alebregtse and de Swart* [2016].

The model made during this study is comparable to the model given by *MacCready* [2004], only now it is generalised to a network. The full derivation of the model for a single channel (including the assumptions made and the boundary conditions that are used) is given in the Appendix, Section 7.1.1-7.1.7. Here, only a short explanation on some physical aspects of the model and the final equations are given. The basic equations[2] that are used read

$$0 = -g\frac{\partial \eta}{\partial x} - \beta g \int_z^\eta \frac{\partial s}{\partial x} dz' + \frac{\partial}{\partial z}(K_M \frac{\partial u}{\partial z}), \tag{2.1a}$$

$$\frac{\partial}{\partial x}\big[Bus - BK_{HS}\frac{\partial s}{\partial x}\big] + \frac{\partial}{\partial z}\big[Bws - BK_S\frac{\partial s}{\partial z}\big] = 0, \tag{2.1b}$$

$$\frac{\partial Bu}{\partial x} + \frac{\partial Bw}{\partial z} = 0. \tag{2.1c}$$

These equations are width-averaged (see Section 7.1.1) and tidally-averaged and each of these equations holds for every channel separately. In other words, a certain variable, for instance u is actually u_i with i =1,2,3 the channel number (the indices are omitted in order to increase readability). In these equations B is the width of the channel, u the subtidal (tidally-averaged) velocity in the x-direction, w the subtidal vertical velocity, g the gravitational acceleration, β is the coefficient of saline contraction[3] (see *Cushman-Roisin and Beckers* [2011]) and s the subtidal salinity. Furthermore, K_M is the vertical eddy viscosity (a measure of vertical internal friction) and K_{HS} and K_S are the horizontal and vertical diffusion coefficients (that are measures of horizontal and vertical turbulent mixing of salinity). Equation 2.1a is the momentum balance in the x-direction and the first term on its right-hand side is the barotropic pressure gradient, the second term the baroclinic pressure gradient and the last two terms are the horizontal and vertical internal friction terms. Equation 2.1b is the salt balance equation, which contains terms representing horizontal and vertical advection of salt (term containing us and ws respectively) and horizontal and vertical turbulent mixing of salt (terms containing K_{HS} and K_S). Equation 2.1c is the continuity equation. The parametrisations of the eddy viscosities and diffusion coefficients are provided later in this chapter.

Now, the conditions at the boundary between river and estuary and the conditions at the branching point are given in Figure 2.2. The salt transport into a particular

[2]See Section 7.1.1 for the derivation of these equations from basic equations given by textbooks such as *Cushman-Roisin and Beckers* [2011] and *Gill* [1982].

[3]The coefficient of saline contraction is a constant that gives the dependence of density on salinity.

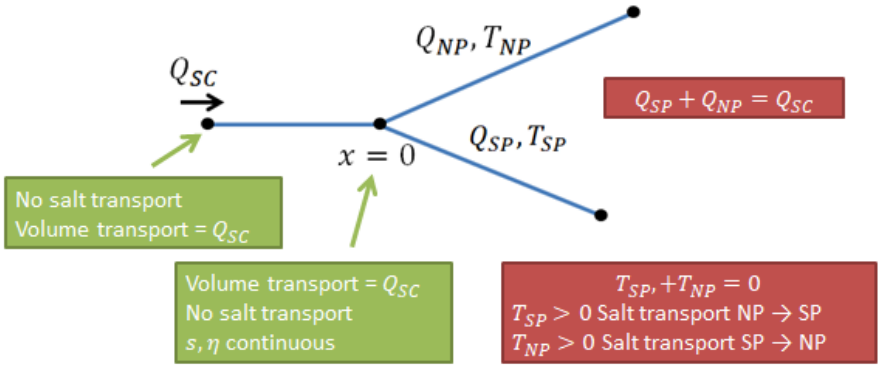

Figure 2.2: Schematic figure illustrating the most important boundary conditions in the model.

channel (originating from another channel or the river) is given by T. At the boundary between estuary and river it is imposed that there is no salt transport (see *Hansen and Rattray* [1965] for conditions at the landward boundary, as the river contains only fresh water $T_{SC} = 0$, that is there is no net salt transport into the South Channel (SC) at this boundary, left green rectangle in Figure 2.2). It will be shown that T (in this case T_{SC}) is constant. Therefore, at the branching point $T_{SC} = 0$ as well and there is no net salt transport between on one side the South Passage (SP) and the North Passage (NP) and on the other side the South Channel (right green rectangle in Figure 2.2). However T_{NP} (the net salt transport into the North Passage) and T_{SP} (the net salt transport into the South Passage) do not have to be zero necessarily and it follows that (lower red rectangle)

$$T_{NP} + T_{SP} = T_{SC} = 0. \tag{2.2}$$

When $T_{SP} > 0$, there is net salt transport from the North Passage to the South Passage ($T_{NP} < 0$ in that case). If $T_{NP} > 0$, there is net salt transport from the South Passage to the North Passage (then $T_{SP} < 0$, see also bottom red rectangle). It is imposed that, volume transport equals the river discharge (Q_{SC}) at the boundary between river and South Channel (see *Hansen and Rattray* [1965] and this condition is given in the left green rectangle in the figure). It will also be derived that, in the whole South Channel (SC) and therefore also at the branching point, the volume transport should also equal Q_{SC} (see right green rectangle). Consequently, we can say that Q_{SC} is the river transport through the South Channel. As there is no source of sink of (river) water at the branching point it follows that (see upper red rectangle with Q_{NP} the river transport through the North Passage and Q_{SP} the river transport through the South Passage)

$$Q_{SP} + Q_{NP} = Q_{SC}. \tag{2.3}$$

Furthermore, its is assumed that η =0 at the seaward boundary for both the South Passage and the North Passage[4]. Finally, it is assumed that at the branching point the subtidal salinity (s) and the subtidal sea surface height (η) are continuous. At the boundaries between the estuary and the ocean, another boundary condition is subscribed, namely that the salinity at the bottom of the estuary equals the salinity of the ocean. The corresponding equation (see *MacCready* [2004]) is

$$\text{at } x = L_{sea},\, z = -H: \qquad s = s_{ocn}. \tag{2.4}$$

In the model the salinity and the horizontal flow velocity are written as the sum of a depth-averaged part ($\overline{s}$ and $\overline{u}$) and a depth-dependent part (s' and u'), that is

$$s = \overline{s} + s', \tag{2.5}$$

$$u = \overline{u} + u'. \tag{2.6}$$

An equation for the depth averaged velocity ($\overline{u}$) is found by using the boundary condition that, at the boundary between the system and the river, the velocity integrated over the cross-section should equal the river discharge. Mathematically this means that $B\int_{-H}^{\eta} u dz = Q$, where Q is the river discharge. It can be shown, from integration of the continuity equation (Equation (2.1c)) and using the boundary conditions that this holds for every x (see Section 7.1.2 in the appendix for details). The boundary conditions are

$$u, w = 0 \;\text{ at } z = -H, \tag{2.7}$$

$$w = u\frac{\partial \eta}{\partial x} \;\text{ at } z = \eta. \tag{2.8}$$

These condition mean no flow at the bottom and no flow normal through the free surface (see e.g. *Gill* [1982] and *Cushman-Roisin and Beckers* [2011]). It is found that

$$B\int_{-H}^{\eta} u dz = Q \qquad \forall x. \tag{2.9}$$

[4]Note that z =0 is defined at the sea surface on the seaward boundary. From this definition and assuming that η at the seaward boundary is the same for the South Passage and the North Passage, it follows that η =0 at the seaward boundary for both the South Passage and the North Passage.

This equation shows that for all x, the volume transport equals the river discharge. From this equation the following expression for $\overline{u}$ is found:

$$\overline{u} = \frac{1}{H}\int_{-H}^{\eta} u dz = \frac{Q}{BH}. \tag{2.10}$$

Similarly, an equation for the depth-averaged salinity ($\overline{s}$) follows by integration over depth of the salt balance and applying the boundary conditions. The boundary conditions are (together with Equation (2.7) and (2.8))

$$K_{HS}\frac{\partial s}{\partial x}\frac{\partial H}{\partial x} + K_S\frac{\partial s}{\partial z} = 0 \text{ at } z = -H, \tag{2.11}$$

$$-K_{HS}\frac{\partial s}{\partial x}\frac{\partial \eta}{\partial x} + K_S\frac{\partial s}{\partial z} = 0 \text{ at } z = \eta. \tag{2.12}$$

The conditions physically mean no salt diffusion normal to the bottom and no salt diffusion normal to the surface (see e.g. *Gill* [1982]). The resulting equation is the salt transport equation (see Section 7.1.2-7.1.7 for details on the derivation), namely

$$B\int_{-H}^{\eta}(\overline{us} + u's' - K_{HS}\frac{\partial \overline{s}}{\partial x})dz = T \qquad \forall x. \tag{2.13}$$

This equation shows that the depth integrated salt transport is constant.

Now, in order to be able to find a solution for $\overline{s}$ from Equation (2.13), first solutions for s' and u' should be found. The Equation for u' is found by taking the derivative to z of the momentum equation, this gives

$$\frac{\partial^3 u'}{\partial z^3} = -\frac{\beta g}{K_M}\frac{\partial \overline{s}}{\partial x}. \tag{2.14}$$

Here, it is assumed that $\frac{\partial s'}{\partial x} << \frac{\partial \overline{s}}{\partial x}$ and that K_M is independent of z (see *MacCready* [2004] and the Appendix 7.1.2=7.1.7 for details). This equation shows that the depth-independent part of the horizontal velocity depends on horizontal (depth-averaged) salinity gradients. A solution for u' is found by integrating Equation (2.14) multiple times and applying Equation (2.7), (2.10) and using

$$\frac{\partial u'}{\partial z} = 0 \text{ at } z = 0. \tag{2.15}$$

This equation stems from a free-slip condition at the surface (see *Cushman-Roisin and Beckers* [2011] and Section Section 7.1.2-7.1.7 for details). The solution for u' reads

$$u' = u_E F_1 + \overline{u} F_2. \tag{2.16}$$

Here, u_E gives the strength of the density-driven flow (also called exchange flow, see also *MacCready* [2004]). So the depth-dependent part of the flow velocity is dependent on both the river flow and the density-driven flow. The functions F_1 and F_2 are polynomials of z. The density-driven flow, u_E is given by

$$u_E = \frac{g\beta H^3}{48 K_M} \frac{\partial \overline{s}}{\partial x}. \tag{2.17}$$

The functions F_1 and F_2 are given by

$$F_1 = 1 - 9\zeta^2 - 8\zeta^3, \tag{2.18}$$

$$F_2 = \frac{1}{2} - \frac{3}{2}\zeta^2. \tag{2.19}$$

In these Equations ζ is defined as

$$\zeta \equiv \frac{z}{H}. \tag{2.20}$$

An equation for s' is found by evaluation of the order of magnitude of the different in Equation (2.1b), (2.1c) and (2.13), combining these equations and, again, evaluating the order of magnitude of the different terms in the resulting equation (see the Appendix, Section 7.1.2-7.1.7, for details). The resulting equation is

$$K_S \frac{\partial^2 s'}{\partial z^2} = u' \frac{\partial \overline{s}}{\partial x}. \tag{2.21}$$

Basically, this equation says that there is balance between the stimulation of stratification by vertical velocity shear and the weakening of stratification by vertical turbulent mixing of salt (see *MacCready* [2004] for more information). In order to solve this equation for s', Equation (2.16) is substituted in Equation (2.21) and the resulting equation is integrated multiple times with respect to z and boundary conditions are applied (see the Appendix, Section 7.1.2-7.1.7, for details, there are some subtleties in this derivation). The solution for s' is

$$s' = \frac{H^2}{K_S} \frac{\partial \overline{s}}{\partial x} (u_E F_3 + \overline{u} F_4). \tag{2.22}$$

This equation shows that the depth-dependent part of salinity also depends on both density-driven and river flow. In this equation, the functions F_3 and F_4 are polynomials of z and are given by

$$F_3 = -\frac{1}{12} + \frac{1}{2}\zeta^2 - \frac{3}{4}\zeta^4 - \frac{2}{5}\zeta^5, \quad (2.23) \qquad F_4 = -\frac{7}{120} + \frac{1}{4}\zeta^2 - \frac{1}{8}\zeta^4. \quad (2.24)$$

Plots of F_1 and F_2 against ζ are shown in Figure 2.3a. Similar plots are made for F_3 and F_4 (Figure 2.3b). Physically, F_1 (F_2) is a function describing the part of u' that originates from the density-driven (river) flow and F_3 (F_4) describes the part of s' that originates from the density-driven (river) flow (see Figure 1.2). In Figure 2.3a the plot of F_1 clearly shows the structure of the density-driven flow, with seaward (positive) velocities near the surface and landward (negative) velocities near the bottom. The contribution of the density-driven flow at the bottom is zero, as a no slip boundary condition is assumed (and the contribution of the river flow is zero there is well). The contribution of the river flow to u' (indicated by F_2) is always seaward. This contribution is strongest near the surface and gets weaker for greater depths. This observation can be explained by the fact that a river contains fresh water and because of the low density of this water, the river water tends to stay close to the surface. Although part of the river water is brought to greater depths by turbulent mixing. In Figure 2.3b the plots of F_3 and F_4 show both density-driven flow and river flow tend to cause an increase in salinity near the bottom and a decrease in salinity near the surface (with respect to the depth-averaged salinity). In other words they both are associated with stratification.

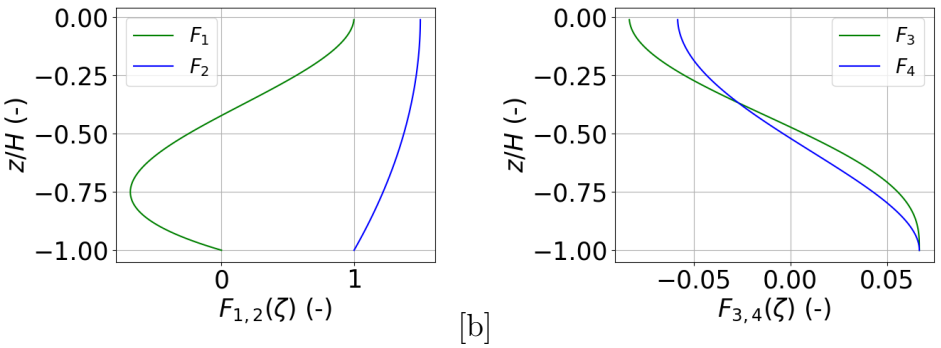

[a] [b]

Figure 2.3: Plots of F_1 and F_2 ([a]) and F_3 and F_4 ([b]) against $\zeta = \frac{z}{H}$. The Function F_1 (F_2) describes the part of u' that originates from the density-driven (river) flow and F_3 (F_4) describes the part of s' that originates from the density-driven (river) flow.

Now that solutions for u' and s' are available, these can be substituted in Equation (2.13). As $\eta << H$ (see Section 7.1.2 and 7.1.3), the integral in this equation is evaluated from $z = -H$ to z =0. In this way, an Equation describing $\overline{s}$ is found.

The result is

$$-(L_{E3}\frac{\partial\Sigma}{\partial x})^3-(L_{E2}\frac{\partial\Sigma}{\partial x})^2-(L_{E1}+L_D)\frac{\partial\Sigma}{\partial x}+\Sigma=\frac{T}{Qs_{ocn}}. \tag{2.25}$$

Here, Σ is a scaled version of the salinity, given by

$$\Sigma=\frac{\overline{s}}{s_{ocn}}. \tag{2.26}$$

In this salt transport equation, T is the (constant) net salt transport into[5] a particular channel and s_{ocn} the salinity of the adjacent ocean. The expressions for the length scales L in Equation 7.62 are

$$L_{E3}=\big[C_3\frac{H^8\beta^2s_{ocn}^2g^2}{K_SK_M^2\overline{u}}\big]^{\frac{1}{3}}, \tag{2.27a}$$

$$L_{E2}=\big[C_2\frac{H^5\beta s_{ocn}g}{K_SK_M}\big]^{\frac{1}{2}}, \tag{2.27b}$$

$$L_{E1}=C_1\frac{H^2\overline{u}}{K_S}, \tag{2.27c}$$

$$L_D=\frac{K_{HS}}{\overline{u}}. \tag{2.27d}$$

Here, $C_3=\frac{0.030}{48^2}$, $C_2=\frac{0.045}{48}$ and $C_1=0.019$ are constants. In equation (2.25)the terms containing L_{E3}, L_{E2} and L_{E1} represent salt transport due to the density-driven flow (which contains both river flow and density driven flow). The term containing L_D represents salt transport due to horizontal diffusion and the term containing Σ originates from salt transport due to river flow (see *MacCready* [2004]. As discussed in Chapter 1 (Figure 1.5), salt transport due to horizontal diffusion and density-driven flow are import terms and salt transport due to river flow is an export term.

2.2 Channel characteristics

Similar to what was done in many previous studies (such as *Savenije* [1986] and *Zhang et al.* [2011]), channel width (B) is parametrised by an exponential function, and is given by

[5]That it is salt transport into a particular channel can be understood by only keeping in mind the last two terms in Equation (2.25) and ignoring all the other terms for a moment. It is then observed that Σ increases (decreases), when T is positive (negative).

$$B(x) = B_0 \exp\left(\frac{1}{\lambda_s}(x - x_0)\right). \tag{2.28}$$

In these equations, λ_s is a constant convergence length scale and x_0 is a reference x-coordinate. The depth, H is described by a fifth order polynomial for the South Channel and the South Passage and a constant for the North Passage (there depth is almost constant). This parametrisation is made based on estimated depths from *Navionics* (`https://webapp.navionics.com/?lang=en#boating@7&key=_tz_EowycV`). It is chosen to use the maximum depth on the map for a certain value of x. The parametrisation for depth (in the South Channel and South Passage) is given by

$$H(x) = p_0 + p_1 x + p_2 x^2 + p_3 x^3 + p_4 x^4 + p_5 x^5. \tag{2.29}$$

The different p's are constants. The values of the different parameters are given in Table 2.3 (Section 2.6).

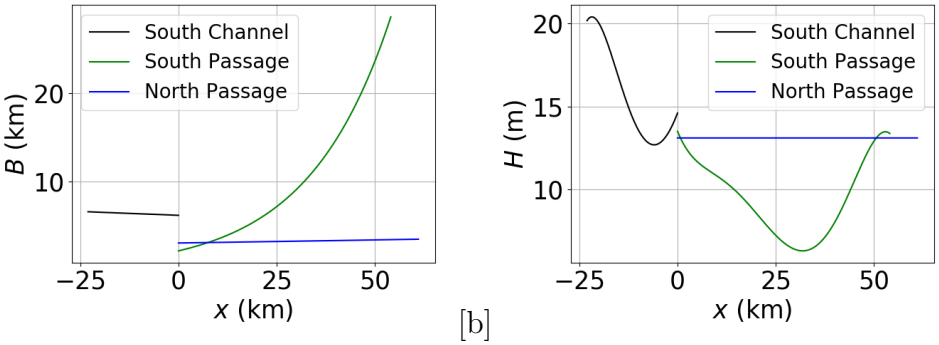

[a] [b]

Figure 2.4: The width ([a]) and depth ([b]) against x as described in the model for the three different channels. The maximum depth on the map for a certain value of x is used. The parameter values for width are from *Alebregtse and de Swart* [2016] and the depth is estimated using the map from *Navionics* (`https://webapp.navionics.com/?lang=en#boating@7&key=_tz_EowycV`). The parametrisation for depth (in the South Channel and South Passage).

Figure 2.4 contains plots of the parametrisations for the width and for the depth in the three different channels. From Figure 2.4a it is visible that the South Channel and the North Passage have a rather straight shape and the South Passage is funnel-shaped. On average, the South Passage has a larger width than the other two channels. From Figure 2.4b it follows that the North Passage is (generally) deeper than the South Passage and the South Channel has the largest depth (on average).

2.3 Parametrization of the eddy viscosity and diffusion coefficients

In this project the vertical eddy viscosity (K_M) and the vertical diffusion coefficient (K_S) are parameterised by the formulation by *Munk and Anderson* [1948], while the formulation by *MacCready* [2007] is used for the horizontal diffusion coefficient K_{HS}. The expressions read (see *Dyer* [1997] and *Guha and Lawrence* [2013])

$$K_M = C_v U_T H (1 + 10 Ri_L)^{-\frac{1}{2}}, \tag{2.30a}$$

$$K_S = C_v U_T H (1 + 3.33 Ri_L)^{-\frac{3}{2}}. \tag{2.30b}$$

$$K_{HS} = 0.0525 U_T B, \tag{2.30c}$$

Here, C_v is a constant, U_T is the tidal velocity amplitude and Ri_L is the Richardson number, defined by $Ri_L \equiv \frac{gH(\rho_{bottom} - \rho_{top})}{\rho_0 U_T^2}$ (see *MacCready* [2007]). The Richardson number is small when there is a lot of mixing and little stratification and it is large when there is a lot of stratification. Note that the factor 0.0525 in K_{HS} is different from *Guha and Lawrence* [2013], why this factor chosen is explained in Chapter 5. The equation of state used in this model is

$$\rho = \rho_0 (1 + \beta s) \tag{2.31}$$

Here, ρ is the reference density (see e.g. *MacCready* [2004]). Using this equation Ri_L can be rewritten as (see *Geyer* [2010])

$$Ri_L = \frac{gH\beta\Delta s}{U_T^2} \tag{2.32}$$

Here, $\Delta s = s_{bottom} - s_{top}$.

Equation (2.30a) and (2.30b) show that K_M and K_S are dependent on U_T, H and Δs. Physically this means that internal friction and turbulent mixing of salt increase when tidal velocity increases and decrease for larger stratification. These relations can be expected as in literature it is described that there is competition between stratification and tides, with stratification limiting and tides enhancing mixing (see *Geyer and MacCready* [2014]). Also, K_{HS} depends on tidal velocity, as horizontal turbulent mixing of salt is caused by the tides (see *MacCready* [2007]).

Note that K_S and K_M depend on salinity itself via Ri_L (Ri_L depends on Δs and Δs follows from Σ). It shows that turbulence and salinity are connected, as was illustrated in Figure 1.6.

In addition to Ri_L, another measure is defined to quantify stratification. This measure is the stratification parameter (χ) given by

$$\chi = \frac{\Delta s}{s_{bottom}}. \tag{2.33}$$

The definition of χ is similar to the one by *Guha and Lawrence* [2013], only the one defined here varies with x. While Ri_L is a measure of how Δs changes with respect to a scale which is fixed for a specific channel, χ is a measure of how Δs changes with respect to the maximum salinity (which is equal to s_{bottom}). As the maximum salinity varies with x as well, χ gives a relative measure for stratification.

2.4 Solution method

For the network configuration, a complication is that the river transports, Q_{SP} and Q_{NP}, and the salt transport into a specific channel, T_{SP} and T_{NP}, are unknown beforehand. How to deal with this complication is described in Section 2.5, here it is assumed that Q_{SP}, Q_{NP}, T_{SP} and T_{NP} are known already (i.e. they are already determined using the method of Section 2.5).

In this thesis a similar method of solving Equation (2.25) is used as proposed in *MacCready* [2004]. The starting point for calculating Σ in the South Passage and the North Passage is the boundary condition Equation (2.4). This equation can be written as $\Sigma\big|_{x=L_{sea}} + \frac{s'}{s_{ocn}}\big|_{x=0,\zeta=-1} = 1$ and, by using Equation 2.22, this is rewritten as

$$\Big[\frac{g\beta s_{ocn}H^5}{720K_MK_S}\Big(\frac{\partial\Sigma}{\partial x}\Big)^2 + \frac{H^2}{15K_S}\overline{u}\frac{\partial\Sigma}{\partial x} + \Sigma - 1\Big]\Big|_{x=L_{sea}} = 0. \tag{2.34}$$

In this equation, Σ is eliminated using Equation (2.25) (see *MacCready* [2004]) resulting in

$$\begin{aligned}\Big[L_{E3}^3\Big(\frac{\partial\Sigma}{\partial x}\Big)^3 + \Big(L_{E2}^2 + \frac{g\beta s_{ocn}H^5}{720K_MK_S}\Big)\Big(\frac{\partial\Sigma}{\partial x}\Big)^2 + \Big(L_{E1} + L_D + \frac{H^2}{15K_S}\overline{u}\Big)\frac{\partial\Sigma}{\partial x} \\ + \frac{T}{Q_R s_{ocn}} - 1\Big]\Big|_{x=L_{sea}} = 0.\end{aligned} \tag{2.35}$$

From this equation $\frac{\partial\Sigma}{\partial x}\big|_{x=L_{sea}}$ is determined. The result is substituted into Equation 2.25 and the resulting equation is used to find $\Sigma\big|_{x=L_{sea}}$. Now the following scheme is used to calculate Σ at the next point in the x-direction:
Thereafter, $\Sigma\big|_{x-\delta x}$ is substituted into Equation (2.25) and from the result $\frac{\partial\Sigma}{\partial x}\big|_{x-\delta x}$ is calculated. After this, Equation (2.36) is used to calculate Σ at the next point

and in this way Σ is calculated at every point in the South Passage and the North passage. At the branching point, Σ should be continuous, i.e. $\Sigma_{SP}\big|_{x=0} = \Sigma_{NP}\big|_{x=0} = \Sigma_{SC}\big|_{x=0}$. This condition gives $\Sigma\big|_{x=0}$ for the South Channel and, using Equation (2.25), $\frac{\partial\Sigma}{\partial x}\big|_{x=0}$ is determined. Then, using Equation (2.36) and (2.25), Σ and $\frac{\partial\Sigma}{\partial x}$ at all other points in the South Channel are determined just as was done for the other two channels.

$$\Sigma\big|_{x-\delta x} = \Sigma\big|_{x} - \delta x \frac{\partial\Sigma}{\partial x}\big|_{x}. \tag{2.36}$$

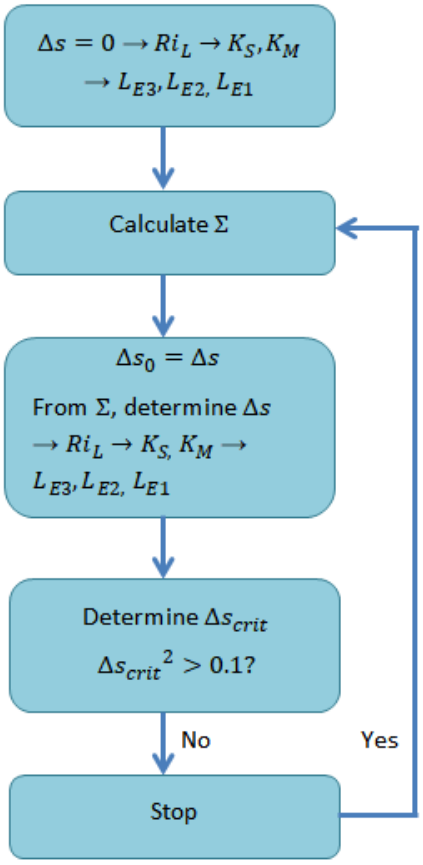

Figure 2.5: Diagram illustrating the different iteration steps in the model.

In Section 2.3 it was shown that K_S and also K_M depend on salinity via Ri_L and Δs (note that Δs is calculated using Σ). For this reason, K_S and K_M have to be determined iteratively. Figure 2.5 illustrates how this is done in the model. The

starting value for Δs is $\Delta s = 0$ (for all x). From this value Ri_L is calculated, using Ri_L, K_S and K_M can be calculated and thereafter also L_{E3}, L_{E2} and L_{E1} (which depend on K_S and/or K_M) are calculated. As Δs is a function of x, all these variables are dependent on x. The next step is to calculate Σ (which is a scaled depth-averaged salinity) using these variables (as described earlier in this section). Next, the old Δs is stored as Δs_0 and a new Δs is calculated using Σ. Again, from the found Δs, Ri_L, K_S, K_M, L_{E3}, L_{E2} and L_{E1} are determined. Thereafter $\Delta s_{crit} = \sqrt{\frac{1}{L}\int_{x_{begin}}^{x_{end}} (\Delta s - \Delta s_0)^2 dx}$ is determined (by numerical integration). If $\Delta s_{crit}^2 > 0.1$ psu^2, Σ will be calculated with the new values of K_S, K_M, L_{E3}, L_{E2} and L_{E1}, otherwise, the model will stop and the last calculated values for Σ are accepted.

2.5 Finding river water transports and salt transports

A priori it is unknown how the river transport through the South Channel will be divided between the South Passage and the North Passage and this distribution is determined in the model. Also, it is not known of which direction and magnitude the salt transport between the South and the North Passage is (and in the first place if this transport exists at all). In other words, Q_{SP} and T_{SP} should be determined in the model. Thereafter, Q_{NP} and T_{NP} follow from Q_{SP} and T_{SP}. There are two conditions that determine Q_{SP} and T_{SP}, namely both Σ and η should be equal for the South Passage and the North Passage at the branching point (or in other words Σ and η should be continuous). Mathematically, these conditions are

$$\Sigma_{SP}\big|_{x=0} = \Sigma_{NP}\big|_{x=0}, \qquad (2.37) \qquad\qquad \eta_{SP}\big|_{x=0} = \eta_{NP}\big|_{x=0}. \qquad (2.38)$$

Using the following expression (which is derived in Appendix Section 7.1.8), η at the branching point is determined[6]:

$$\eta\big|_{x=0} = \eta\big|_{x=L_{sea}} + \int_{x=0}^{x=L_{sea}} \frac{3K_M Q_R}{gBH^3} dx + \int_{x=0}^{x=L_{sea}} \frac{3\beta s_{ocn} H}{8} \frac{\partial \Sigma}{\partial x} dx. \qquad (2.39)$$

The integration is done numerically. In order to determine Q_{SP} an T_{SP}, in the model, Σ at all locations in the South Passage and the North Passage is calculated

[6]Note that $\eta\big|_{x=L_{sea}}$ =0 in this model.

(following the method illustrated in Figure 2.5) for different values of Q_{SP} and T_{SP}. From Σ, also η at the branching point can be determined using Equation (2.39). Then, using these values for Σ and η, the following criteria are calculated for every possible combination of the different values of Q_{SP} and T_{SP}:

$$crit_1 = \frac{\left|\Sigma_{SP,bif} - \Sigma_{NP,bif}\right|}{(0.01/s_{ocn})}, \tag{2.40a}$$

$$crit_2 = \frac{\left|\eta_{SP,bif} - \eta_{NP,bif}\right|}{\sqrt{\eta^2_{SP,bif} + \eta^2_{NP,bif}}}. \tag{2.40b}$$

Here, $\Sigma_{SP,bif} = \Sigma\big|_{x=0}$ and $\eta_{SP,bif} = \eta_{SP}\big|_{x=0}$ (in m) and analogous for the North Passage. From the two criteria a combined criterion is calculated, which is given by

$$crit_{comb} = \sqrt{crit_1^2 + crit_2^2}. \tag{2.41}$$

In order to find Q_{SP} and T_{SP}, this criterion is calculated for different values of Q_{SP} and T_{SP}. The values for Q_{SP} and T_{SP} that minimize the value for $crit_{comb}$ are selected and used in the model. In this process of finding Q_{SP} and T_{SP}, first a large range in Q_{SP} and T_{SP} are tried, with large steps between different values for Q_{SP} and T_{SP}. The values for Q_{SP} and T_{SP} corresponding to the smallest value for $crit_{comb}$ are selected. Thereafter, this process is continued a few times with each time a smaller range of values for Q_{SP} and T_{SP} (around the selected values for Q_{SP} and T_{SP}) and a smaller step size. When the step size of Q_{SP} and T_{SP} is sufficiently small, 1 m^3/s and 1 psu m^3/s respectively, the selected values of Q_{SP} and T_{SP} are chosen as the final result for these parameters. From these values, Q_{NP} and T_{NP} are determined using Equation (2.3) and 2.2.

The river water transport through the South Passage and the North Passage is quantified here using the net water division ration (nWDR). This quantity is the ratio of the river transport through one channel (the South Passage or the North Passage) divided by the total river transport through both channels. Mathematically, the definition (which is similar to the one in *Alebregtse and de Swart* [2016]) is

$$\text{nWDR} = \frac{Q_{SP,NP}}{Q_{SP} + Q_{NP}} \times 100\%. \tag{2.42}$$

Here, $Q_{SP,NP}$ is either Q_{SP} or Q_{NP}.

In order to analyse the nWDR, an approximate expression for the ratio $\frac{Q_{SP}}{Q_{NP}}$ is derived in the Appendix (Section 7.1.9). For deriving an exact expression for $\frac{Q_{SP}}{Q_{NP}}$ it was necessary to make the approximations that depth and the vertical eddy viscosity (K_M) are constant over a channel (this is achieved by assuming that Ri_L =0). The found expression for the ratio of Q_{SP} over Q_{NP} is

$$\frac{Q_{SP}}{Q_{NP}} = \frac{\left[\frac{3\beta}{8}(H_{SP}ds_{x,SP} - H_{NP}ds_{x,NP}) + \frac{3K_{M,NP}Q_{SC}L_{s,NP}}{gB_{0,NP}H_{NP}^3}E_{NP}\right]}{\left[\frac{3\beta}{8}(H_{NP}ds_{x,NP} - H_{SP}ds_{x,SP}) + \frac{3K_{M,SP}Q_{SC}L_{s,SP}}{gB_{0,SP}H_{SP}^3}E_{SP}\right]}. \tag{2.43}$$

Here, $ds_x = \overline{s}\Big|_{x=L_{sea}} - \overline{s}\Big|_{x=0}$ and $E = 1 - \exp\left[\frac{x_0}{\lambda_s}\right]$.

2.6 Design of experiments

The research questions that are asked in this study are *How does the idealised model perform in case of an estuarine network that consists of multiple channels?* and *How do results depend on key parameters in such a system (such as river discharge, tidal forcing, geometrical characteristics of the network)?* In order to answer the first questions a reference case is studied. In this reference case, the present situation (after realisation of the Deepwater Navigation Channel, DNC) with spring tide and low river discharge is studied. The different parameter values in the model for this reference case are given in Table 2.2 and Table 2.3 (parameter values describing geometrical properties of the network) at the end of this section.

Thereafter, to answer the second research question, experiments are done where parameters are changed with respect to this reference experiment. An overview of the experiments and which parameters are changed is given in Table 2.1. First, the sensitivity to tides and river discharge is investigated. In order to do that results for all possible combinations between spring tide/neap tide and high/low river discharge (in the present situation) are studied and compared. Secondly, the effect of the Deepwater Navigation Channel (DNC) is investigated. For the situation before the DNC, the North Passage is given made shallower and is given a funnel-shape (in contrast to the present situation were the North Passage is deeper and has a straight shape). In order to isolate the effect of the funnel-shape another experiment is done where the North Passage has the present (larger) depth, but the funnel-shape (as before the DNC).

Experiment nr	Description	Physical changes w.r.t. reference case	Changed parameters w.r.t. reference case
1a	Spring tide high river discharge	Larger river discharge (i)	Q_{SC} =6440 m^3/s
1b	Neap tide low river discharge	Smaller tidal currents (ii)	$U_{T,SC}$ =0.80 m/s, $U_{T,SP}$ =1.05 m/s, $U_{T,NP}$ =0.88 m/s
1c	Neap tide, high river discharge	Larger river discharge (A), smaller tidal current (B)	$U_{T,SC}$ =0.80 m/s, $U_{T,SP}$ =1.05 m/s, $U_{T,NP}$ =0.88 m/s, Q_{SC} =6440 m^3/s
2a	Situation before DNC	North Passage shallower and funnel-shaped (C)	$B_{0,NP}$ =8.5 km, $\lambda_{s,NP}$ =60.0 km, H_{NP} =12.1 m
2b	Situation before DNC present depth	North Passage funnel-shaped (C)	$B_{0,NP}$ =8.5 km, $\lambda_{s,NP}$ =60.0 km

Table 2.1: Overview experiments with reference case: spring tide, dry season in present situation. References of parameter values: (A) *Zhu et al.* [2018] (river discharge) and *Alebregtse and de Swart* [2016] (net water division ratio South Channel), (B) estimated from results amplitide tidal current by Jinyang Wang, (C) *Alebregtse and de Swart* [2016].

It should be noted that K_M and K_S (both for $Ri_L = 0$) and K_{HS} are known when geometry of the network and tidal current are imposed in the model; they are independent of results for salinity and currents. However, when Ri_L is determined iteratively, K_S and K_M are model output. Then, they depend on the salinity distribution.

The first output of the model are Q and T for South Passage and the North Passage. As explained in Section 2.5, these are determined by minimising the criterion $crit_{comb}$. Secondly, Σ is given as model output (Σ is a non-dimensional version of depth-averaged salinity, $\overline{s}$). Also, the depth-averaged and depth-dependent part of the current distribution ($\overline{u}$ and u' respectively) are output of the model. Furthermore, the depth-dependent part of salinity is calculated by the model. Salinity and current distribution are the main variables calculated in the model. From the salinity distribution, the Richardson number (Ri_L) and the stratification parameter (χ) are calculated. Thereafter, Ri_L is used to calculate K_S and K_M.

It is stressed that salinity and Ri_L depend on each other. For instance, the starting value for Ri_L is Ri_L =0 (for all x). This value is used as input to calculate the salinity field. If, after that calculation, the iteration is ended (because the criterion to stop the iterations is satisfied), the calculated salinity distribution is accepted. From that salinity distribution Ri_L can be calculated. However, this distribution of Ri_L is not equal to zero for all x. This illustrates that the Ri_L distribution used to calculate the final salinity distribution is different from Ri_L distribution calculated from this final salinity distribution. The Ri_L calculated from the final salinity distribution is considered the final result for Ri_L.

Variable	Meaning	Value	Units
g	Gravitational acceleration (I)	9.8	m s^{-2}
ρ_0	Reference density (I)	1000.0	kg m^{-3}
β	coefficient of saline contraction (II)	7.7 $\times 10^{-4}$	psu $^{-1}$
$s_{ocn,SC}$	Ocean salinity South Channel (III)	26.22	psu
$s_{ocn,SP}$	Ocean salinity South Passage (III)	26.0	psu
$s_{ocn,NP}$	Ocean salinity North Passage (III)	28.0	psu
dx	Stepsize x-direction	10.0	m
$d\zeta$	Stepsize $\zeta = \frac{z}{H}$	0.01	-
C_v	Parameter eddy viscosity, diffusion coefficient (IV)	0.001	-
$U_{T,SC}$	Tidal current South Channel (V)	1.15	m/s
$U_{T,SP}$	Tidal current South Passage (V)	1.7	m/s
$U_{T,NP}$	Tidal current North Passage (V)	1.4	m/s
Q_{SC}	River discharge entering South Channel (VI)	3714	m^3/s

$\eta\big\vert_{x=L_{sea,SP}}$	Surface height at coast South Passage	0	m
$\eta\big\vert_{x=L_{sea,NP}}$	Surface height at coast North Passage	0	m

Table 2.2: Parameters values. References for values: (I) *Chen* [2018], (II) *MacCready* [2004], (III) *Zhu et al.* [2018], (IV) changed from value by *Huijts et al.* [2009] (see Chapter 5 for details), (V) estimated from result of amplitude semi-diurnal tidal current by Jinyang Wang, (VI) based on *Zhu et al.* [2018] (river discharge) and *Alebregtse and de Swart* [2016] (net water division ratio South Channel).

Variable	Meaning	Value	Units
L_{SC}	Length South Channel (i)	23.0	km
L_{SP}	Length South Passage (i)	54.0	km
L_{NP}	Length North Passage (i)	61.0	km
$B_{0,SC}$	Width, branching point South Channel (i)	6.2	km
$B_{0,SP}$	Width, coast South Passage (i)	30.0	km
$B_{0,NP}$	Width, coast North Passage (i)	3.5	km
$x_{0,SC}$	Reference x South Channel (i)	0.0	km
$x_{0,SP}$	Reference x South Passage (i)	55.0	km
$x_{0,NP}$	Reference x North Passage (i)	61.0	km
$\lambda_{s,SC}$	Convergence length South Channel (i)	-368.0	km

$\lambda_{s,SP}$	Convergence length South Passage (i)	21.0	km
$\lambda_{s,NP}$	Convergence length North Passage (i)	470.0	km
$p_{0,SC}$	Parameter depth South Channel (ii)	1.460 $\times 10^{1}$	m
$p_{1,SC}$	Parameter depth South Channel (ii)	6.198 $\times 10^{-4}$	-
$p_{2,SC}$	Parameter depth South Channel (ii)	4.493 $\times 10^{-8}$	m^{-1}
$p_{3,SC}$	Parameter depth South Channel (ii)	-9.668 $\times 10^{-13}$	m^{-2}
$p_{4,SC}$	Parameter depth South Channel (ii)	-3.946 $\times 10^{-18}$	m^{-3}
$p_{5,SC}$	Parameter depth South Channel (ii)	2.267 $\times 10^{-21}$	m^{-4}
$p_{0,SP}$	Parameter depth South Channel (ii)	1.350 $\times 10^{1}$	m
$p_{1,SP}$	Parameter depth South Channel (ii)	-5.832 $\times 10^{-4}$	-
$p_{2,SP}$	Parameter depth South Channel (ii)	5.962 $\times 10^{-8}$	m^{-1}
$p_{3,SP}$	Parameter depth South Channel (ii)	-3.643 $\times 10^{-12}$	m^{-2}
$p_{4,SP}$	Parameter depth South Channel (ii)	8.958 $\times 10^{-17}$	m^{-3}

$p_{5,SP}$	Parameter depth South Channel (ii)	-7.199 $\times 10^{-22}$	m^{-4}
H_{NP}	Depth North Channel (ii)	13.1	m

Table 2.3: Values of geometrical parameters. References of parameter values: (i) *Alebregtse and de Swart* [2016] and (ii) determined from *Navionics* (`https://webapp.navionics.com/?lang=en#boating@7&key=_tz_EowycV`).

Chapter 3

Results 1: reference case, spring tide and low river discharge

First, a reference case will be discussed. For this reference case a low river discharge (Q_{SC} =3714 m^3s^{-1}) is chosen and the tidal currents are given the values for spring tide (see Table 2.2 for the specific numbers). The reference case considers the present day situation.

3.1 River water and salt transports

An example of a flow diagram for this reference case is given in Figure 3.1. The contours give, for every value of river transport (Q_{SP}) and salt transport (T_{SP}) in the South Passage the value the combined criterion $crit_{comb} = \sqrt{crit_1^2 + crit_2^2}$ (a measure of the difference in salinity and surface height between the South Passage and the North Passage) at the branching point. According to the boundary conditions this difference should disappear (and $crit_{comb}$ should approach zero, see Section 2.5). The right values for Q_{SP} and T_{SP} are found by finding the minimum value for $crit_{comb}$ (marked with the white dot in the figure). The final result of this process is Q_{SP} =2152 m^3s^{-1} and T_{SP} =-165 psu m^3s^{-1} (indicating salt transport from the South Passage into the North Passage). The physical meaning of this result is sketched in Figure 3.2.

The percentages give the net water division ratio (nWDR, defined by Equation (2.42)) in the South Passage and the North Passage. The 165 psu m^3 s^{-1} salt transport from the South Passage into the North Passage is also indicated. The salt transport from the South Passage into the North Passage is in agreement with the study by *Zhu et al.* [2018]. It appears from the figure that there is more river transport through the South Passage than through the North Passage.

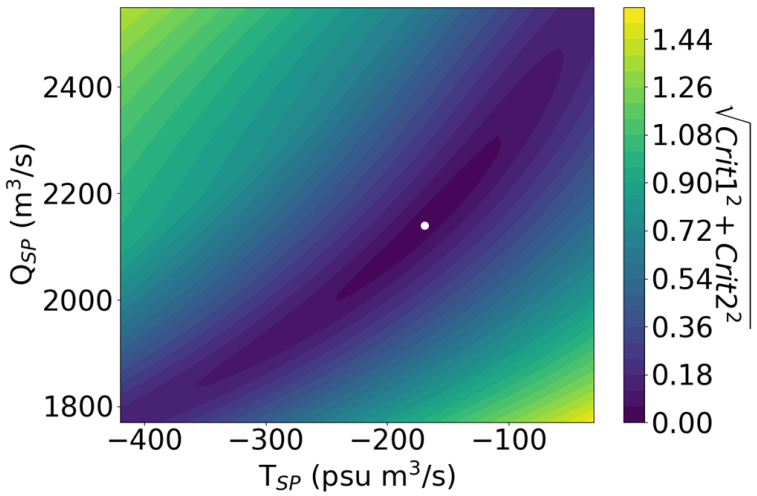

Figure 3.1: Example of a flow diagram for the reference case (spring tide, low river discharge and present-day situation). The contours indicate the value for the combined criterion ($crit_{comb} = \sqrt{crit_1^2 + crit_2^2}$) for each value for the river transport (Q_{SP}) and salt transport (T_{SP}) in the South Passage. According to boundary conditions, this combined criterion should be minimal. The white dot indicates the minimum for the combined criterion ($crit_{comb} = \sqrt{crit_1^2 + crit_2^2}$). The values for Q_{SP} and T_{SP} at the dot are selected.

Equation (2.43) can be used to investigate why there is more river transport through the South Passage than through the North Passage. This equation gives an approximation for $\frac{Q_{SP}}{Q_{NP}}$, assuming that depth and eddy viscosity (K_M) are constant. From filling out the parameter values in Table 2.2 and 2.3 into Equation (2.43) and assuming that Ri_L =0 and $\Delta s = s_{ocn}$ a nWDR of 57% for the South Passage is found. For the reference case Equation (2.43) seems to give a reasonable approximation for $\frac{Q_{SP}}{Q_{NP}}$.

Now, it is interesting to know which factors lead to an increase $\frac{Q_{SP}}{Q_{NP}}$ and therefore explain the higher nWDR in the South Passage (than in the North Passage). From calculations with Equation (2.43), using the parameter values in Table 2.2 and 2.3, it appears that the funnel-shape (i.e. the small convergence length scale for the width of the channel) of the South Passage and the larger tidal current (and consequently larger K_M) and smaller depth in the South Passage (than in the

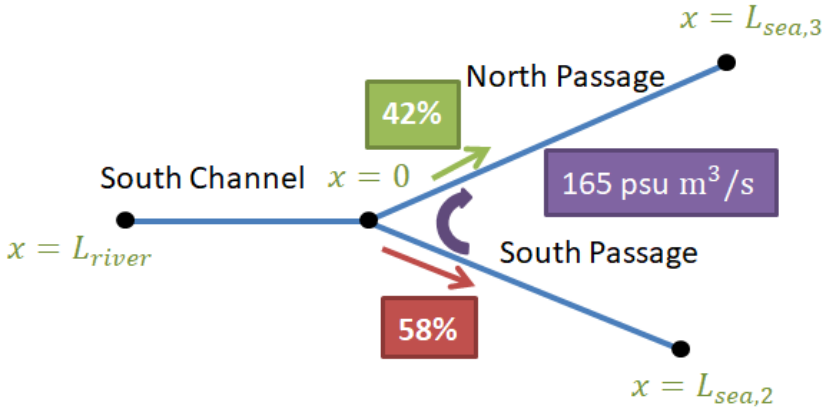

Figure 3.2: Sketch giving the salt transport from the South Passage into the North Passage (in purple) and the net water division ratio (nWDR) in both channels (in red and green). These results are for the reference case (spring tide, low river discharge and present-day situation).

North Passage) all decrease the ratio $\frac{Q_{SP}}{Q_{NP}}$.[1] Therefore, these characteristics of the channels do not explain the larger nWDR in the South Passage (which means that $\frac{Q_{SP}}{Q_{NP}} > 1$). Nevertheless, these relations are physically understandable as the stronger tidal current in the South Passage provides more friction (and this possibly makes river flow more difficult) and due to the shallower South Passage there is less space for river transport. Furthermore, a larger λ_s makes the South Passage narrower near the branching point; therefore, there is little space there for river flow to enter the channel.

However, what does explain (according to the calculations with Equation (2.43)) that $\frac{Q_{SP}}{Q_{NP}} > 1$ is mainly that $B_{0,SP} > B_{0,NP}$. Physically $B_{0,SP} > B_{0,NP}$ means that the width (near sea) is larger for the South Passage than for the North Passage. The increase in $\frac{Q_{SP}}{Q_{NP}}$ for $B_{0,SP} > B_{0,NP}$ is physically plausible as a greater width of the South passage (near sea) provides more space for river transport. The other explanation for $\frac{Q_{SP}}{Q_{NP}} > 1$ is that $\Delta s_{NP} > \Delta s_{SP}$. However this effect seems to be barely visible. Physically, the increase in $\frac{Q_{SP}}{Q_{NP}}$ for $\Delta s_{NP} > \Delta s_{SP}$ might be

[1] The first two things can be reasoned from Equation (2.43) itself (without needing a lot of numbers). From trial calculations with Equation (2.43) it appears that both the numerator and the denominator are negative, so if the numerator (denominator) gets more (less) negative $\frac{Q_{SP}}{Q_{NP}}$ will increase. A larger U_T and λ_s for the South Passage cause a less negative numerator and a more negative denominator; leading to a decrease in $\frac{Q_{SP}}{Q_{NP}}$.

explained by the relation that a larger horizontal salinity gradient in the North Passage increases the diffusion of salt into this channel and this potentially provides more resistance for river flow to enter the North Passage.

3.2 Depth-averaged salinity

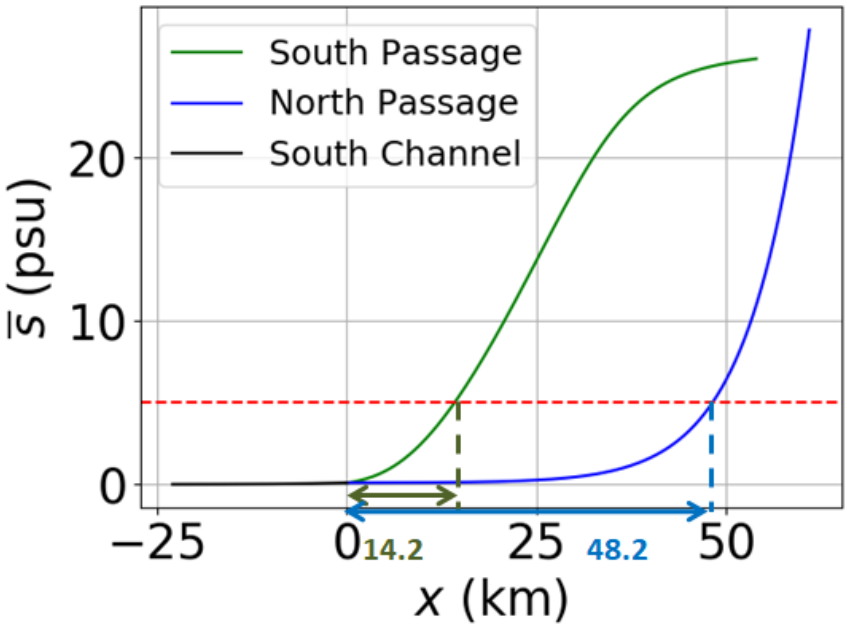

Figure 3.3: Depth averaged salinity ($\overline{s}$) against x in the three channels. Again, the reference case is considered (spring tide, low river discharge and present-day situation). The arrows and numbers indicate the distance between the branching point and the $\overline{s}$ =5 psu-line (in green for the South Passage and in blue for the North Passage).

Next, Figure 3.3 shows the depth averaged salinity ($\overline{s}$) for the three channels. In the figure, the distance between the branching point (at x =0) and the $\overline{s}$ = 5 psu-line is indicated with arrows and numbers (in green for the South Passage and in blue for the North Passage). When this distance is shorter, there is more salt intrusion. The figure suggests that there is more salt intrusion in the South Passage than in the North Passage. This is also found in literature (see e.g. *Zhu et al.* [2018]). A more extensive comparison of the results with literature is given in Chapter 5. Why the salt intrusion in the South Passage is larger than in the North Passage is discussed later (in Section 4.2.2). The larger salt intrusion in the South Passage

might also explain why a salt transport was found from the South Passage to the North Passage (see Figure 3.2); there is simply more salt available (near the branching point) in the South Passage than in the North Passage to transport to the other channel.[2] The figure also shows that there is almost no salt in the South Channel.

3.3 River and density-driven flow

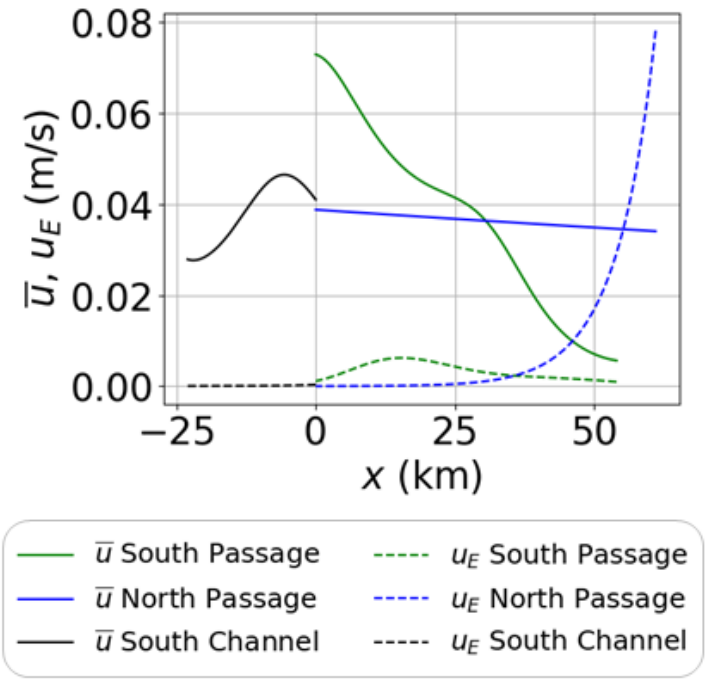

Figure 3.4: Depth averaged velocity ($\overline{u}$, solid line) and strength of the density-driven flow (u_E, dotted line) against x in the three channels. Again, the reference case is considered (spring tide, low river discharge and present-day situation).

Also, the depth-averaged velocity ($\overline{u}$) is calculated by the model. As explained before, the depth-averaged velocity equals the river flow. Figure 3.4 shows this velocity, together with the strength of the density-driven flow (u_E) in the three

[2]It seems contradictory that very little salt reaches the branching point, but that there is still a transport of salt from the South Passage to the North Passage. However, this salt transport only causes a very small change in the salinity. This is understood by considering the last two terms in Equation (2.25) in Section 2.1. As Q is in the order of a few thousand m^3/s and s_{ocn} is 26 or 28 psu, a very big value for T_{SP} is needed in order to see a noticeable difference in Σ.

different channels. The figure shows that the river flow decreases in seaward direction particularly for the South Passage, but also for the North Passage. As $\overline{u} = \frac{Q}{BH}$ (Equation (2.10)) and river transport (Q) is constant in a channel, changes in $\overline{u}$ are described by geometry. Figure 2.4 shows that the width (B) of the South Passage strongly increases seaward and that the depth (H) is approximately the same at the branching point as near the ocean. For this reason, the decrease in river flow in the South Passage is caused by the funnel-shape of this channel. Because the river transport in the South Passage is distributed over a larger area when it moves towards the ocean, the river flow weakens in seaward direction. In the North Passage the depth is constant (in the model) and the width weakly increases in seaward direction and this explains the slight decrease in river flow towards the ocean. The river flow in the South Channel is stronger seawards and weaker near the landward boundary. The width of the South Channel decreases seaward and together with the net seawards decrease in depth, this explains the seawards increase in river flow.

The density-driven flow appears to be clearly the strongest in the North Passage. Equation (2.17) shows that the strength of the density-driven flow is proportional to H^3 and $\frac{\partial \overline{s}}{\partial x}$. The stronger density-driven flow is probably explained by the strong horizontal gradient in depth-averaged salinity ($\frac{\partial \overline{s}}{\partial x}$) near the ocean, apparent from Figure 3.3 and the large depth of the North Passage (relative to the South Passage).

For the South Channel and the South Passage, the figure suggests that the river flow is (generally) much stronger than the density driven-flow. The density-driven flow in the South Channel is (almost) absent, because of the little salt that is present in the South Channel (consequently $\frac{\partial \overline{s}}{\partial x}$ is very small). The density-driven flow in the South Passage is strongest just seaward of branching point, possibly due to a combination of the large depth near the branching point and the strong $\frac{\partial \overline{s}}{\partial x}$ a bit seaward of the branching point.

3.4 Distribution of currents

Now it is interesting to see how the river flow and the density-driven flow combine into the current distribution. The current distribution for the different channels is given in Figure 3.5. For the North Passage, there is seaward flow near the surface and landward flow near the bottom. This structure is characteristic for the density-driven flow (see Figure 1.2). The density-driven flow in this channel is strongest near the coast, which is in agreement with Figure 3.4.

For the South Passage and the South Channel all the velocities are seawards. This means that, for these channels, mainly river flow is visible and the density-driven

flow is weak. This was also concluded from Figure 3.4. Furthermore, Figure 3.5 shows that velocities are stronger near the surface. This was also concluded from Figure 2.3a and is according to expectations as fresh water from river flow is buoyant and tends to stay close to the surface.

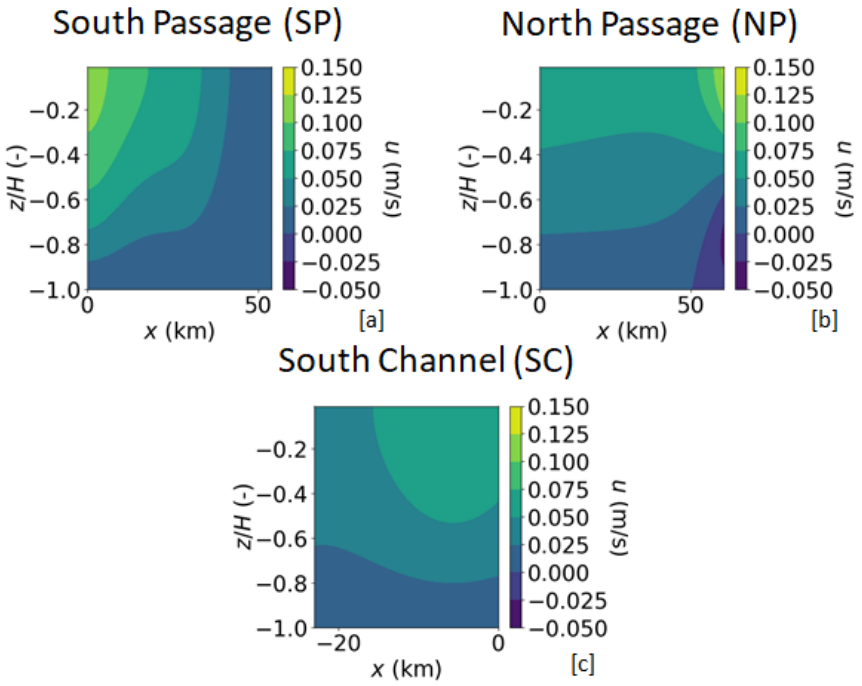

Figure 3.5: Plots of the subtidal current for the reference case (spring tide, low river discharge and present-day situation) for the three different channels.

3.5 Salinity distribution

First, the salinity distributions for the three different channels are plotted and given in Figure 3.6. The 5 psu and 15 psu lines are shown in white. From the figures, it is immediately clear that there is much more salt intrusion in the South Passage than in the North Passage. This is in agreement with Figure 3.3. A possible explanation for this observation is that the river flow in the South Passage decreases in seaward direction (due to the funnel-shape of the South Passage and consequently the decreasing cross-section in seaward direction), as suggested by Figure 3.4. Due to the decreasing river flow, salt experiences a weaker push out of the estuary near the ocean. This hypothesis is further tested in Section 4.2. Also, the South Passage has a larger tidal current than the North Passage (see

Section 2.2). As a result, horizontal diffusion increases (note that K_{HS} is linear in U_T), resulting in more salt intrusion. The other side is that, a higher tidal current increases mixing and the density-driven flow is weakened in the South Passage. This causes a lower salt intrusion, but apparently the other two effects (funnel-shaped South Passage and stronger horizontal diffusion) are stronger and the salt intrusion is higher in the South Passage.

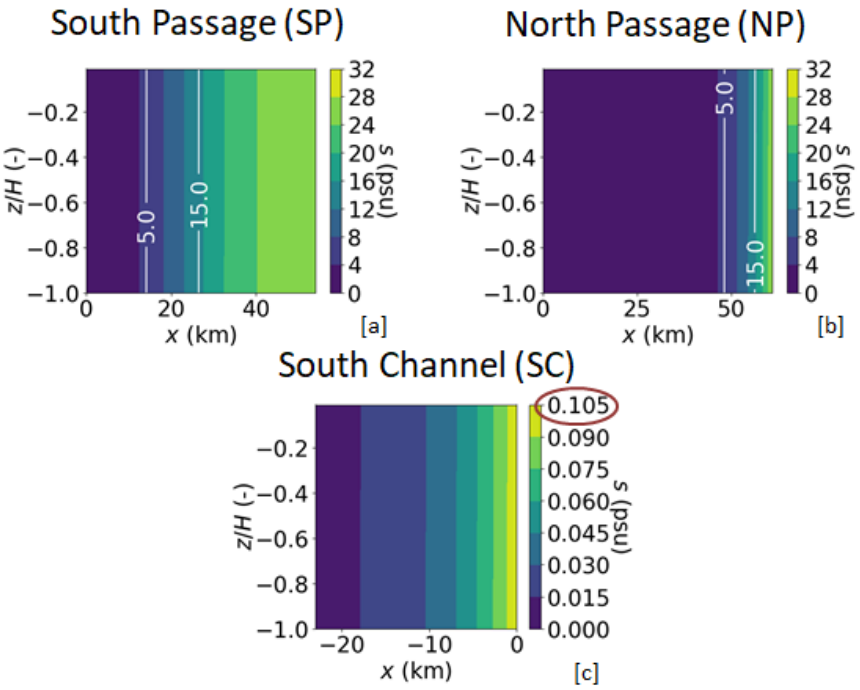

Figure 3.6: Plots of the salinity distribution in the present situation with spring tide and low river discharge for the three different channels. The 5 psu line and the 15 psu line are given in white. Note that the colorbars are the same for the South Passage and the North Passage, but is different for the South Channel (in fact there is almost no salt intrusion in the South Channel).

It is noted that the plot for the South Channel has different contour levels than the figures for the South Passage and the North Passage, because there is very little salt intrusion in the South Channel. Furthermore, it is observed that in all the channels, the lines of equal salinity are rather vertical. This indicates that there is little stratification and a lot of mixing. Because there is little stratification, the density-driven flow will be weak (see Chapter 1) and it is expected that the most important mechanism for salt intrusion is horizontal diffusion.

3.6 Stratification

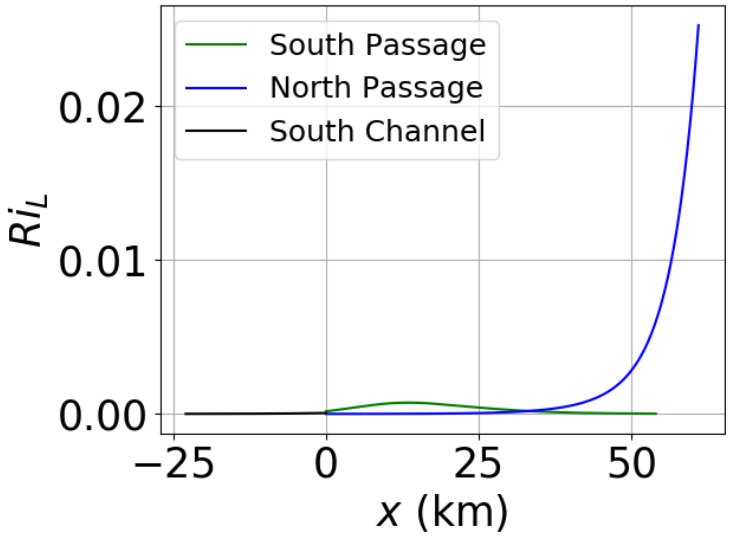

Figure 3.7: The Richardson number (Ri_L) for the three different channels. The Richardson number is large when there is a lot of stratification and it is small when there is a lot of mixing. Again the reference case is considered (spring tide, low river discharge and present-day situation).

In order to study the stratification further, the Richardson number and stratification parameter are useful. Figure 3.7 gives the Richardson number (Ri_L) for the three different channels. The Richardson number is defined by Equation 2.32 (Section 2.3) and the Richardson number increases when stratification is stronger. From the figure it can be concluded that the North Passage has the most stratification (according to the Richardson number). The highest Richardson number in this channel is found near the ocean. In *Monismith et al.* [1996] it is explained that the gravitational circulation increases stratification and *Geyer and MacCready* [2014] expect that river flow also has an increasing effect on stratification. In Figure 3.4 it is visible that, in the North Passage, there is a strong density-driven flow (and a fairly strong river flow) close to the ocean. This strong density-driven flow possibly explains the high Richardson number in the North Passage, especially because the shape of the graphs of Ri_L (Figure 3.7) and u_E (Figure 3.4) are rather similar. The river flow near the branching point in the South Passage is large, but the Richardson number is still relatively small there. The maximal Richardson number in the South Passage is just seaward of the branching point and approximately coincides with the maximal density-driven flow in the South passage. This sug-

gests that the connection between density-driven flow and the Richardson number is stronger than the connection between river flow and the Richardson number. The Richardson number in the South Channel is very small as there is very little salt there.

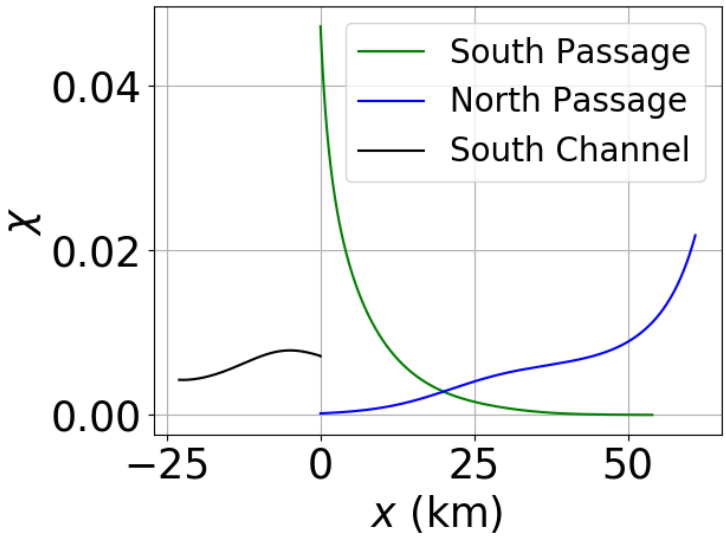

Figure 3.8: The stratification parameter (χ) against x for the three different channels in the reference case (spring tide, low river discharge and present-day situation). The stratification parameter increases when stratification is stronger.

Figure 3.7 shows the stratification parameter (χ) for the three different channels. The definition of the stratification parameter is given in Equation (2.33) (Section 2.3) and the stratification parameter is larger when stratification is stronger. It is explained in Section 2.3 that Ri_L gives an absolute scale (which is fixed for a specific channel) for the change in Δs . In contrast, χ gives the relative change of Δs with respect to the salinity at the bottom of the channel (which also varies with x).

Figure 3.7 shows maximal stratification parameter near the branching point in the South Passage. This maximum was not visible in Ri_L as salinities are very small near the branching point and Δs is scaled by an absolute value there. In χ, the small Δs near the branching point is scaled by a small s_{bottom} and therefore it is possible that χ is large for small salinities. The figure shows that the stratification parameter decreases seaward for the South Passage. This is possibly explained by the decrease in river flow towards the sea (see Figure 3.4). It seems that

river flow has a stronger relation with the stratification parameter than with the Richardson number. The stratification parameter decreases landwards for the North Passage. Again, this might be explained by the landwards decrease in strength of the exchange flow. The graph of the stratification parameter for the South Channel has a similar shape as the graph for the river flow (see Figure 3.4), suggesting a connection between the two.

3.7 Eddy viscosity and diffusion coefficients

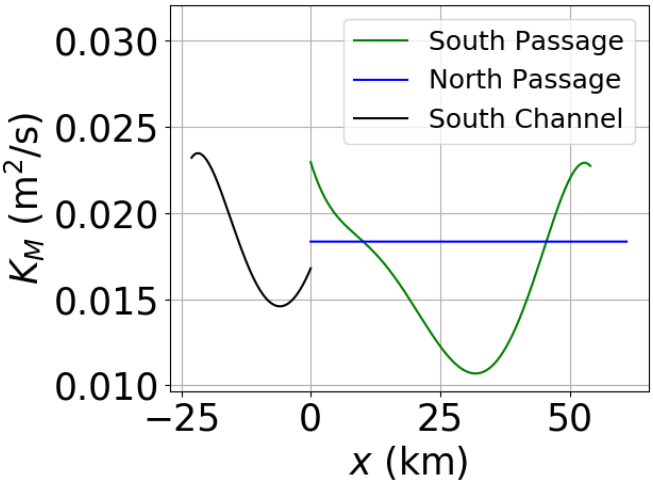

Figure 3.9: The vertical eddy viscosity (K_M, measure of internal friction) against x for the three different channels in the reference case (spring tide, low river discharge and present-day situation).

The last variables that are calculated by the model are the vertical eddy viscosity (K_M, a measure of internal friction), and the vertical an horizontal diffusion coefficients (K_S and K_{HS} respectively, they give a measure of vertical and horizontal turbulent mixing of salt). Figure 3.9 shows the vertical eddy viscosity, Figure 3.10 the vertical diffusion coefficient and 3.11 the horizontal diffusion coefficient (that are used in the model calculations) against x.

Figure 3.9 and Figure 3.10 show that K_M and K_S are exactly the same. It was explained in Section 2.4 that Ri_L is determined iteratively and that the first model calculations are done with Ri_L =0. For the reference case it appears that the criterion to stop these iterations (Δs^2_{crit} >0.1 in Figure 2.5) is already met after these calculations with Ri_L =0. In other words, the model calculations are carried out

using Ri_L =0. When Ri_L =0 is substituted into the definitions of K_M and K_S (Equation 2.30a and 2.30b respectively), it appears that K_M and K_S are exactly the same. It is noted that Figure 3.7 shows non-zero values for Ri_L as these values for Ri_L are calculated using the results for salinity distribution (they are calculated after the salinity distribution was found, these values of Ri_L are not the values that are used in the calculation of the salinity itself).

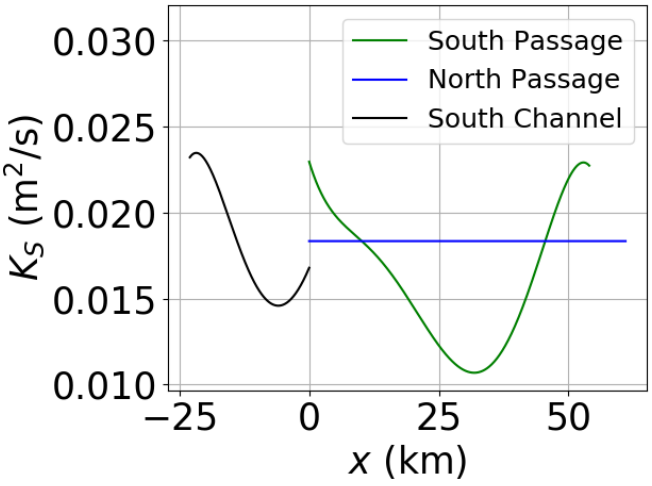

Figure 3.10: The vertical diffusion coefficient (K_S, measure of vertical turbulent mixing of salt) against x for the three different channels in the reference case (spring tide, low river discharge and present-day situation).

As K_M and K_S are calculated with Ri_L =0, the only variable in their equations (Equation (2.30a) and (2.30b)) that is not constant (in a channel) is depth. As K_M and K_S are linear in H, their graphs have the same shape as the graph of H (see Figure 2.4). Because, according to Equation (2.30c), K_{HS} is linear in B (and the other variables are constant in a channel), the graph K_{HS} of K_{HS} has the same shape as the graph of channel width (see Figure 2.4).

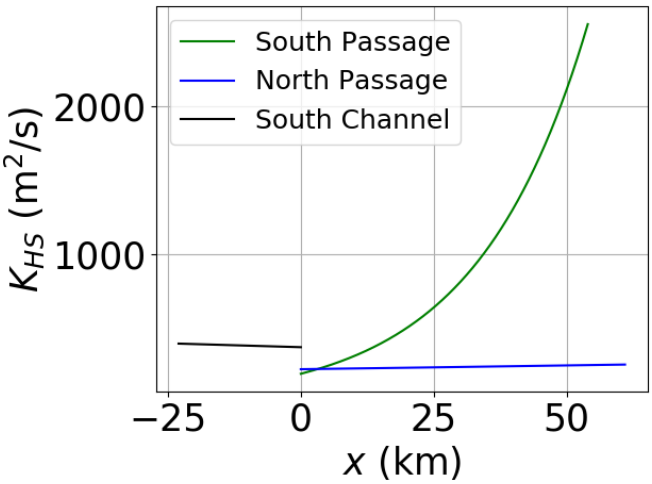

Figure 3.11: The horizontal diffusion coefficient (K_{HS}, measure of horizontal turbulent mixing of salt) against x for the three different channels in the reference case (spring tide, low river discharge and present-day situation).

Chapter 4

Results 2: sensitivity analysis

4.1 Sensitivity to tides and river discharge

As discussed in Chapter 1, tidal current and river discharge are expected to have an important influence on salt intrusion. In order to study this effect, different conditions are tried, namely all combinations between neap/spring tide and low/high river discharge (Q_{SC} =3714 m^3/s and Q_{SC} =6440 m^3/s respectively). The exact values that are used for the tidal current (U_T) for spring and neap tide are given in Table 2.1. All experiments in this section consider the present-day situation.

4.1.1 River water and salt transport

To begin with, the river water and salt transport in the South Passage and North Passage are found. The results are given in Figure 4.1 (for river transport) and Figure 4.2 (for salt transport). The white percentages in Figure 4.1 indicate the nWDR (percentage of total river water transport that is transported through a certain channel) for a certain channel. The nWDR is defined by Equation (2.42) (see Section 2.5). For interpretation of Figure 4.1, again the approximate expression for $\frac{Q_{SP}}{Q_{NP}}$ (that was introduced in Section 2.5) is used. To obtain this expression it is assumed that depth and K_M (vertical eddy viscosity, measure of internal friction) are constant. The last thing can be achieved by making the approximation that Ri_L =0.

First the river water transport through the South Passage is calculated using Equation (2.43) (using parameter values form Table 2.1, 2.2 and 2.3 and assuming Ri_L =0). Using this equation, the values for the nWDR are estimated. The found values for the nWDR are 57% (spring tide, low river discharge), 63% (neap tide, low river discharge) 53% (spring tide, high river discharge) and 57% (neap tide,

high river discharge). Generally, these numbers are reasonable approximations to the values found in Figure 4.1. However, the nWDR value for neap tide and high river discharge found from Equation (2.43) is a lot higher than the value given in Figure 4.1. However, the case neap tide and high river discharge is the only situation for which a Richardson number (Ri_L) larger than zero is used for the calculations in the model (this is only the case for the North Passage). For all the other situations, the iterations to calculate Ri_L are already ended after the first calculation (which uses Ri_L =0), as the criterion to stop the iterations is met (see Figure 2.5 and Section 2.4 for more details). When the calculation with Equation (2.43) is done again for the situation neap tide and high river discharge, but this time using $Ri_L = 0.2$ for the North Passage[1], it is found that 46 % of the river flow is transported through the South Passage (which is more similar to the value in Figure 4.1), so it seems that stratification is important for determining the distribution of the river flow between the two channels in case of neap tide and high river discharge.

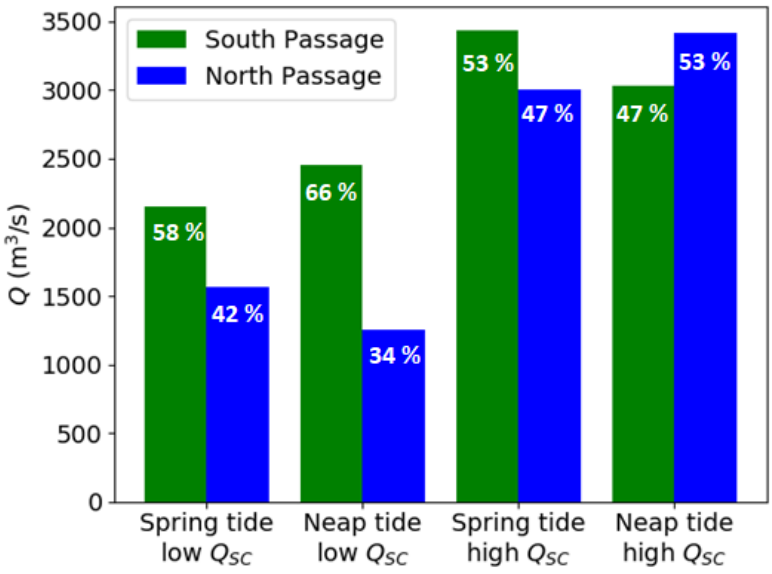

Figure 4.1: Bar plot showing the distribution of the river water transport through the South Passage and the North Passage under varying conditions. The values for the nWDR (percentage of the total river water transport that is transported through a certain channel) are given in white.

[1]In the model calculations a Ri_L between 0 and approximately 2.8 (but for most x, $Ri_L = 0$ or very small) is used for the North Passage for this situation.

The first pattern that is visible in Figure 4.1 is that the nWDR for the North Passage increases when river discharge increases. This observation will be explained in Section 4.1.6, when discussing stratification. Considering the case with low river discharge, it appears that the nWDR for the North Passage is larger for spring tide than for neap tide. In contrast, for high river discharge, the nWDR for the North Passage is larger for neap tide than for spring tide.

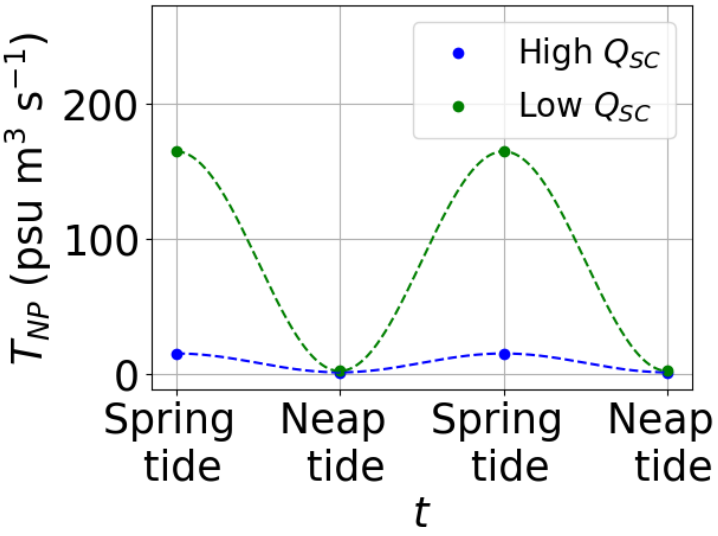

Figure 4.2: Plot of salt transport into the North Passage over time for high and low river discharge (Q_{SC}). It appears that for all situations there is salt transport from the South Passage into the North Passage. Dashed lines suggest a possible trend.

Figure 4.2 shows the salt transport into the North Passage (T_{NP}) against time for high river discharge (Q_{SC}) and low river discharge. The dashed lines show a possible trend in the salt transport into the North Passage. It appears that, if there is salt transport between the two channels, it is always from the South Passage to the North Passage (as $T_{NP} > 0$). During spring tide this salt transport is maximal and during neap tide it almost vanishes. Furthermore, there is more salt transport when river discharge is low than when it is high.

4.1.2 Salt intrusion

In order to study the effect of tides and river discharge on salt intrusion, the distance (L_5) between the branching point and the $\overline{s}$ =5 psu-line is plotted against time in Figure 4.3. Figure 4.3a shows this time series for the South Passage and Figure 4.3b for the North Passage and the time series are shown for high and

low river discharge. The smaller L_5, the more salt intrusion there is. Both Figure 4.3a and 4.3b suggest that salt intrusion decreases (L_5 increases) when river discharge is higher. For this higher river discharge, there is more river water transport through the both channels (see Figure 4.1) and more salt is exported from the estuary by this river water.

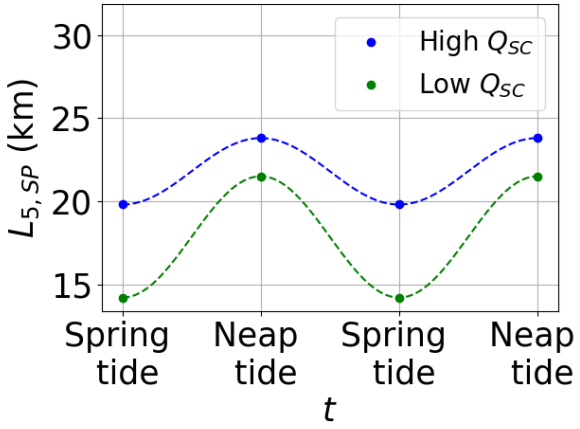

[a]

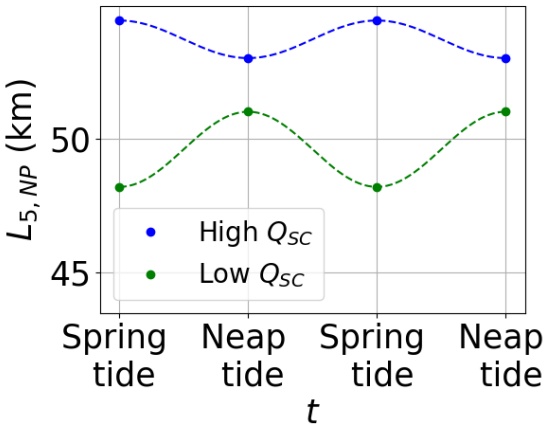

[b]

Figure 4.3: Figure showing the distance (L_5) between the branching point and the $\overline{s} = 5$ psu-line against time for the South Passage ([a]) and the North Passage ([b]). When L_5 is smaller, there is more salt intrusion. The dashed lines give a possible time trend for L_5.

Furthermore, in the South Passage in case of both high and low river discharge and in the North Passage in case of low river discharge, there is more salt intrusion for spring tide than for neap tide. However, in the North Passage in case of a high river discharge, there is less salt intrusion during spring tide than during neap

tide. During spring tide, tidal currents are larger than during neap tide. This has two consequences. First, horizontal diffusion increases (K_S is proportional to U_T, see Equation (2.30b)) and consequently there is more import of salt. Secondly, a larger tidal current results in more mixing (K_S and K_M increase for a larger tidal current, see Equation (2.30b) and Equation (2.30a)). Due to the increased mixing, the density-driven flow will weaken and this results in less salt import (see Section 1.1). The figure suggests that in the North Passage, in case of high river discharge, the effect of the weaker density-driven flow dominates the increased horizontal diffusion and there is less salt intrusion during spring tide. In the other cases, the increased horizontal diffusion dominates and there is more salt intrusion during spring tide. Another option is that the results deviate for the North Passage in case of neap tide and high river discharge, due to model technical reasons. This possibility will be discussed in Chapter 5 Discussion.

It is found that salinity in the South Channel is very low in all cases and for that reason it is chosen to only discuss the South Passage and the North Passage. The profiles of depth-averaged salinity (not shown) show that for all situations, except the North Passage in case of neap tide and high river discharge, the depth-averaged salinity decreases more rapidly landwards for neap tide (compared to spring tide) and high river discharge (compared to low river discharge). This also indicates more salt intrusion for spring tide and a low river discharge in those situations. The profile of depth-averaged salinity for the North Passage in case of wet season and neap tide indicates that the salinity is relatively high near the mouth of the estuary and relatively low in more landwards in the channel (when compared to the situation with the same river discharge but stronger tidal current or the same tide but lower river discharge). This suggests that the effect of the stronger density-driven flow is more strongly present near the mouth of the estuary.

Finally, it is noted that, when salt intrusion in the South Passage is stronger, the salt transport from the South Passage to the North Passage is larger (see Figure 4.2). When there is more salt intrusion in the South Passage there is also more salt to transport to the North Passage and this possibly explains the increased salt transport to the North Passage.

4.1.3 River and density-driven flow

Now, it is interesting to study the effect of tide and river discharge on river flow and density driven flow. To do this, Figure 4.4 shows the river flow (solid lines) and density driven flow (dashed lines) in the South Passage ([a]) and the North Passage ([b]). Figure 4.4a shows that, in the South Passage, river flow is a lot stronger than density-driven flow. This river flow is stronger for high river discharge than

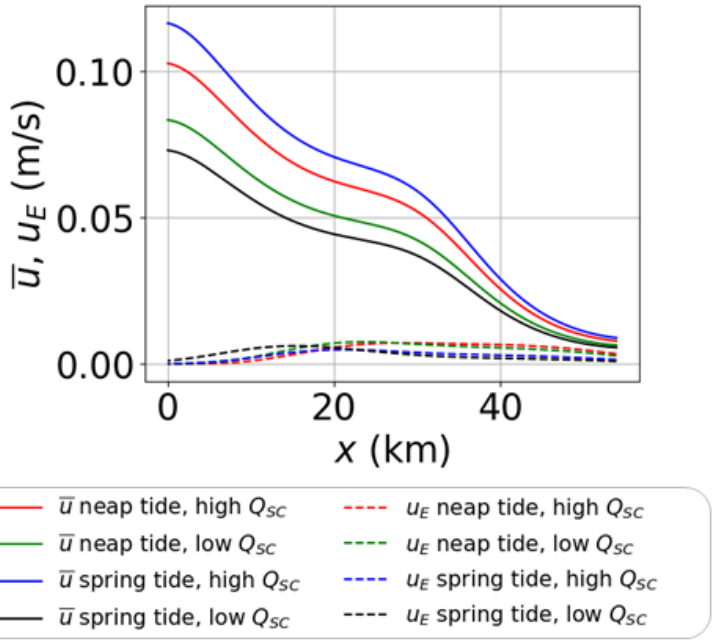

[a]

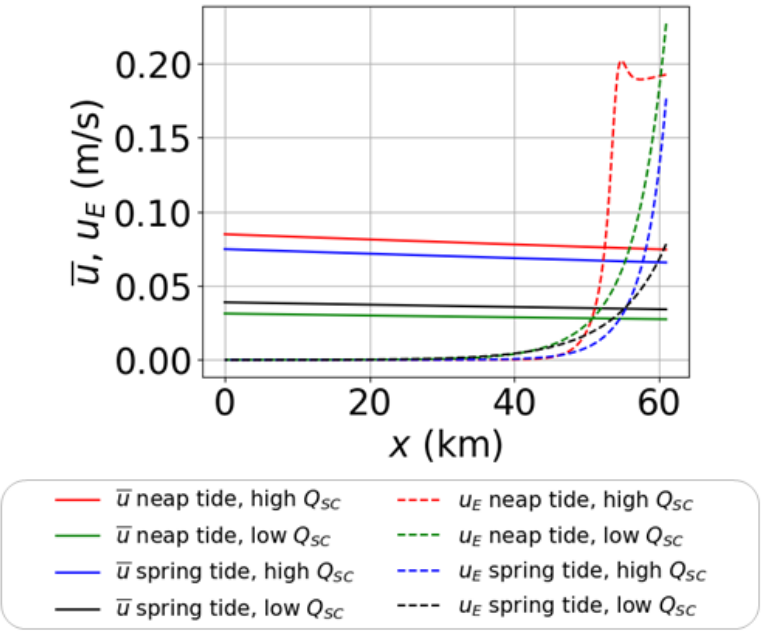

[b]

Figure 4.4: River flow ($\overline{u}$, solid lines) and density-driven flow (u_E, dashed lines) against x in the South Passage ([a]) and the North Passage ([b]).

for low river discharge, as more river water is available when the river discharge is larger. In fact, from comparing Figure 4.4a with Figure 4.1, it appears that a stronger river transport (Q) results in a stronger river flow ($\overline{u}$). This is expected as river flow only depends on river transport and geometry of the channel and the geometry of the channels is the same for all situations. The strength of the exchange flow in the South Passage is comparable for all situations, only locally small variations are visible.

It is suggested by Figure 4.4b that near the mouth of the North Passage, the density-driven flow is a lot stronger than the river flow and landwards the river flow is a lot stronger than the density-driven flow. Again stronger river transport (see Figure 4.1) results in stronger river flow as it should. In the figure, the exchange flow is stronger for higher river discharge and for neap tide (than for spring tide). These results can be expected as river flow is suggested to stimulate stratification (see *Geyer and MacCready* [2014]) and the density-driven flow is stronger for stronger stratification. Also, there is less mixing and consequently more stratification for neap tide than for spring tide and this also results in a stronger density-driven flow.

It was hypothesised that the higher depth-averaged salinities near the mouth of the North Passage in case of neap tide and high river discharge (when compared to the case with the same river discharge but stronger tidal current or the same tide but lower river discharge) results from a more dominant density-driven flow there. From Figure 4.4b it seems that, indeed, the density-driven flow near the mouth of the North Passage is (generally) more dominant for neap tide and high river discharge than for the other situations.

4.1.4 Distribution of currents

Figure 4.5 and 4.6 show the differences (δu) in subtidal current between a certain situation and the reference case (the situation spring tide and low river discharge) for the South Passage and the North Passage respectively. Blue indicates an increase and red a decrease in tidal current with respect to the reference case. In the South Passage, an increase in river flow with respect to the reference case is visible for all situations. This can be recognised by in increase in current (positive δu) over a large range of depths (this increase is not attributed to density-driven flow as this flow shows a clear structure with seawards flow near the surface and landward flow near the bottom). The increase in river flow was also found in Figure 4.4. Similar to Figure 4.4, the largest increase in river flow is found for the case spring tide and high river discharge, than neap tide and high river discharge

and lastly neap tide and low river discharge. For the situations during neap tide, also an (slight) increase in density-driven flow is visible (recognised from negative values for δu near the bottom), which can be explained by the increased stratification due to decreased tidal mixing.

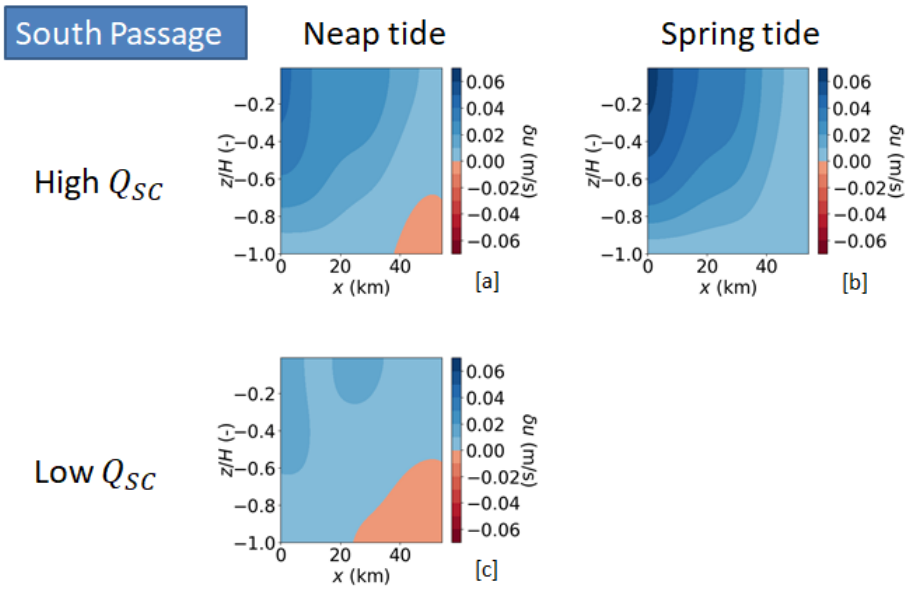

Figure 4.5: Subtidal current difference (δu) between a certain situation and the reference case (spring tide and low river discharge) for the South Passage. The different situations that are shown are all possible combinations between spring/neap tide and high/low river discharge (Q_{SC}). Blue indicates an increase and red a decrease in tidal current with respect to the reference case. There is no figure for spring tide and low river discharge as this is the reference case.

For the North Passage, all the different situations show a stronger density-driven flow near the head of the estuary with respect to the reference case. This increase in density-driven flow is recognised by the cell-like structures with positive values for δu near the surface and the negative values near the bottom. Also, there is a slight decrease in river flow for the situation neap tide (δu shows a lot of negative values over a large range of depths) and low river discharge and a slight increase in river flow for the other situations (positive values for δu over a large range of depths). These observations were also mentioned when discussing Figure 4.4.

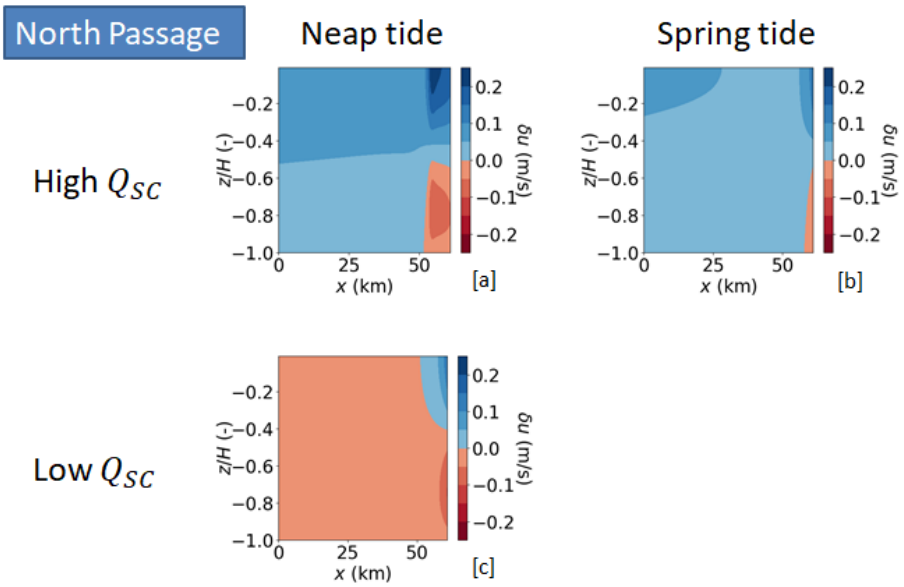

Figure 4.6: Subtidal current difference (δu) between a certain situation and the reference case (spring tide and low river discharge) for the North Passage. The different situations that are shown are all possible combinations between spring/neap tide and high/low river discharge (Q_{SC}). Blue indicates an increase and red a decrease in tidal current with respect to the reference case. There is no figure for spring tide and low river discharge as this is the reference case.

4.1.5 Salinity distribution

Figure 4.7 and 4.8 show salinity under different conditions in the South Passage and North Passage respectively. The salinity distributions for the South Passage show that the lines of equal salinity are vertical for all cases, indicating that there is a lot of mixing and density-driven flow is weak. This was also concluded from Figure 4.4a. Furthermore, the figure shows that salt intrudes further into the estuary for spring tide (than for neap tide) and low river discharge (than for high river discharge). This was also concluded from Figure 4.3.

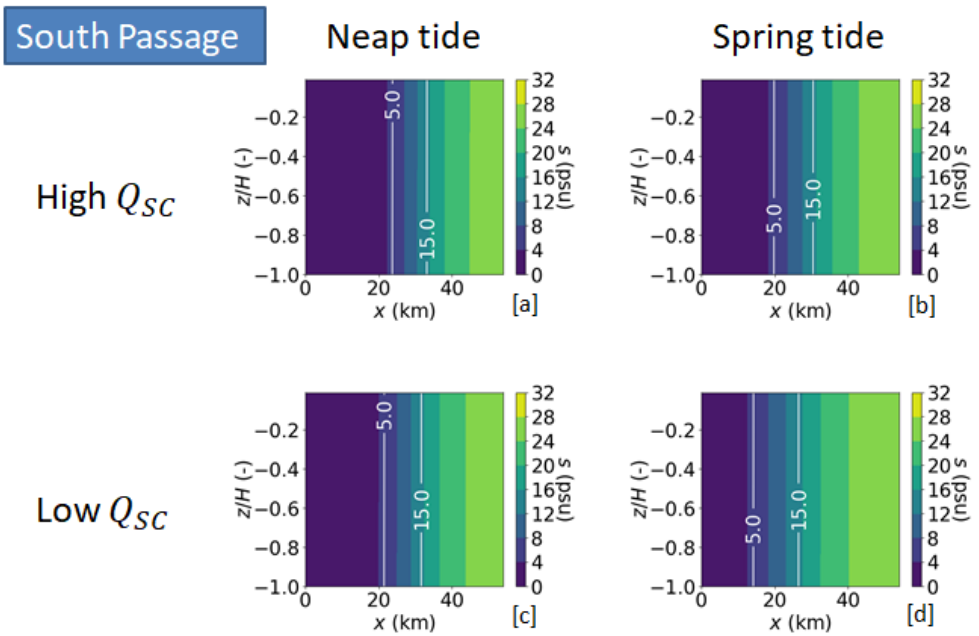

Figure 4.7: Plots of the salinity distribution in the South Passage in case of all possible combinations between spring tide/neap tide and low/high river discharge (Q_{SC}). The 5 psu line and the 15 psu line are marked in white.

For the North Passage, the lines of equal salinity are still rather vertical (indicating a lot of mixing), except from the situation neap tide and high river discharge. For this situation, stratification is visible, with higher salinities near the bottom and lower salinities near the surface. From Figure 4.4b it appeared that this is the situation with (generally) the strongest density-driven flow. For all situations except neap tide and high river discharge, the figure shows that salt intrudes further into the channel for spring tide (than for neap tide) and for a low river discharge (than for a high river discharge). There is more salt intrusion for the situation neap tide and high river discharge, than for spring tide and high river discharge. These observations are similar to those from Figure 4.3.

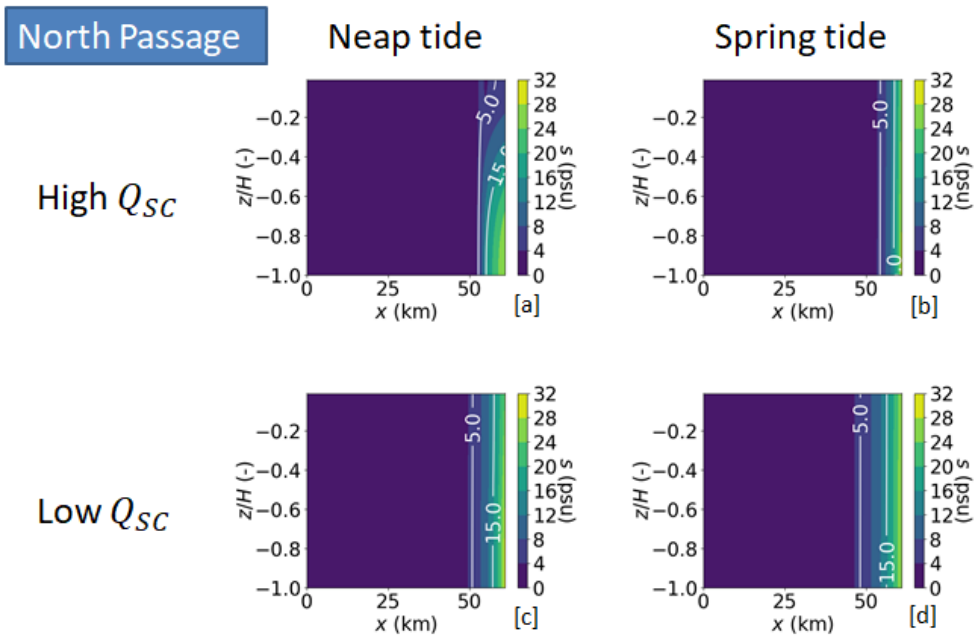

Figure 4.8: Plots of the salinity distribution in the North Passage in case of all possible combinations between spring tide/neap tide and high/low river discharge (Q_{SC}). The 5 psu-line and the 15 psu-line are marked in white.

4.1.6 Stratification

Furthermore, it is interesting to see what effect the different conditions have on stratification. In order to study this effect the Richardson number (Ri_L) is given in Figure 4.9 and the stratification parameter (χ) is plotted in Figure 4.10. The figures show these measures for different situations in the South Passage ([a]) and for the North Passage ([b]). A larger stratification results in higher values for Ri_L and χ. The difference between these measures is that Ri_L is a measure for the absolute salinity difference between bottom and surface and χ is a measure for the salinity difference between bottom and surface relative to the salinity at the bottom (which is the maximal salinity).

Both measures show that there is more stratification for neap tide than for spring tide. This is expected as during neap tide, the tidal current is smaller and therefore there is less mixing and more stratification. Also, the figures show that there is more stratification for a high river discharge, than for a low river discharge. This is also expected, as in literature it is suggested that more river flow leads to more stratification (see e.g. *Geyer and MacCready* [2014]).

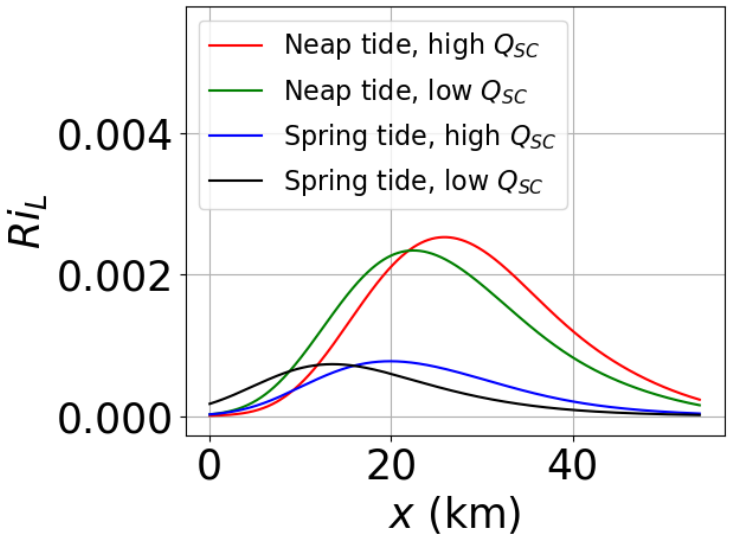

[a]

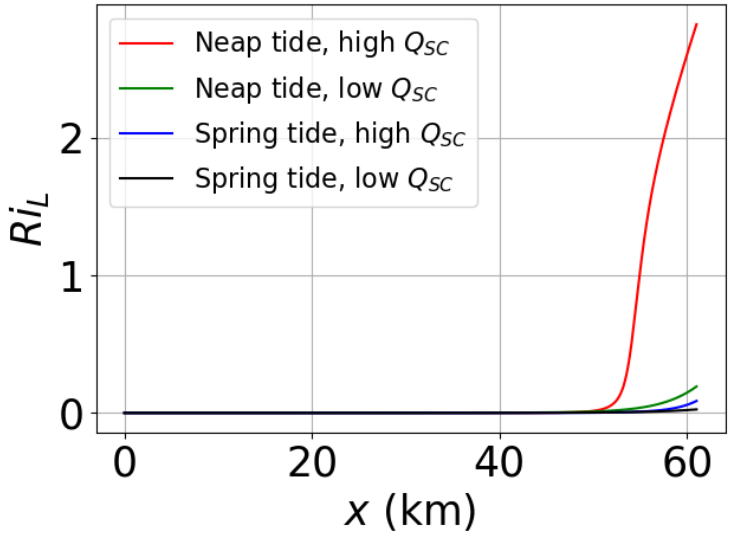

[b]

Figure 4.9: Plots of the Richardson number (Ri_L) for the South Passage ([a]) and the North Passage ([b]) in case of different situations. More stratification results in a larger value for Ri_L.

For the South Passage the peak in the Richardson number shifts towards the branching point, when there is either a transition from neap tide to spring tide or a transition from wet season to dry season. This shift of the peak in stratification towards the branching point seems to coincide with an increase in salt

intrusion. When there is little salt intrusion, there is simply not enough salt near the branching point to develop a clear stratification.

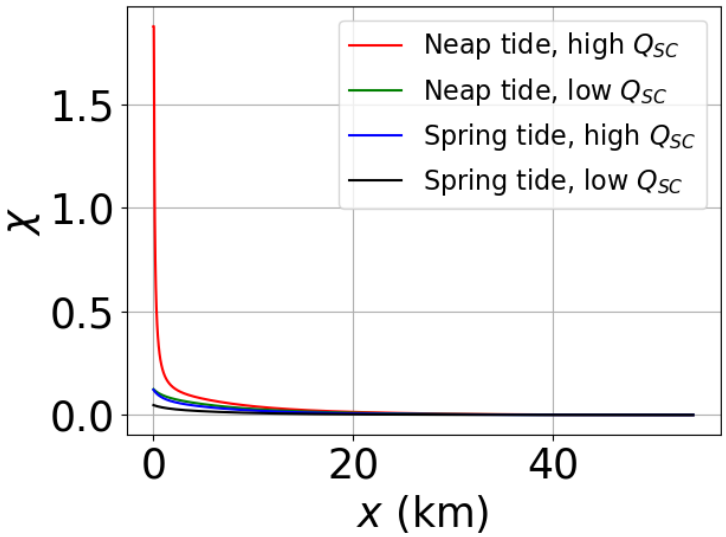

[a]

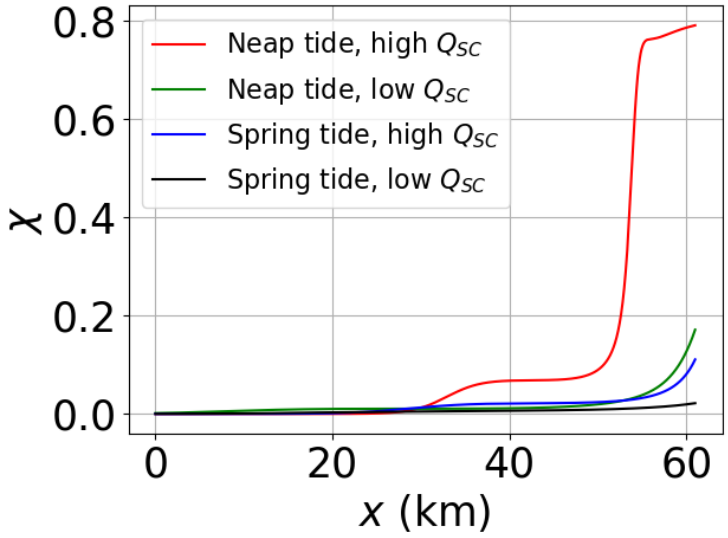

[b]

Figure 4.10: Plots of the stratification parameter (χ) for the South Passage ([a]) and the North Passage ([b]) in case of different situations. Stronger stratification results in a larger value for χ.

Furthermore, from Figure 4.1 it was observed that a larger river discharge leads to a higher nWDR for the North Passage. From Figure 4.9 it is concluded that a larger river discharge leads to a stronger stratification in both channels, but that

this increase in stratification is larger in the North Passage. This possibly explains the higher nWDR for the North Passage, as a stronger stratification results in less friction (see e.g. *Chant and Wilson* [1997]). Due to the decrease in friction, it will be easier for river water to flow through the North Passage. It is noted that, Figure 4.10 does show a large increase in stratification in the South Passage for larger river discharge. However, the location where this stratification is large has a very low salinity.

4.1.7 Eddy viscosity and diffusion coefficients

Figure 4.11 shows the eddy viscosity (K_M, a measure of internal friction) and diffusion coefficient (K_S, a measure of turbulent mixing of salt) in the South Passage ([a]) and the North Passage ([b]). For all situations except for the case neap tide and high river discharge in the North Passage, only one line is given for both K_M and K_S. The reason is that the situation neap tide and high river discharge is the only situation where iterations have taken place to calculate Ri_L (as was explained earlier). From Equation (2.30a) and (2.30b) (the equations for K_M and K_S) it appears that K_M and K_S are the same when Ri_L =0. Another thing that appears from those equations is that K_M and K_S are independent of river discharge when Ri_L =0. Consequently, only for neap tide in the North Passage, separate lines are drawn for high and low river discharge.

Figure 4.11 shows that in both channels K_M and K_S are larger during spring tide than during neap tide. This is expected as, according to Equation (2.30a) and (2.30b), K_M and K_S are linear in U_T (when Ri_L =0). It is noted that the same relation is found for K_{HS} (the horizontal diffusion coefficient, not shown). For spring tide K_{HS} is maximal approximately 2553 m^2s^{-1} in the South Passage and in the North Passage 257 m^2s^{-1}, while for neap tide this is 1577 m^2s^{-1} and 162 m^2s^{-1} respectively. The equation for K_{HS} (Equation (2.30c)) is linear in U_T and independent of Ri_L. The increase in K_M, K_S and K_{HS} for larger tidal current is physically logical as the tides provide mixing. In the North Passage during neap tide, K_M and K_S are larger for a low river discharge. This is also expected, because a low river discharge is expected to reduce stratification and, for this reason, there is more mixing.

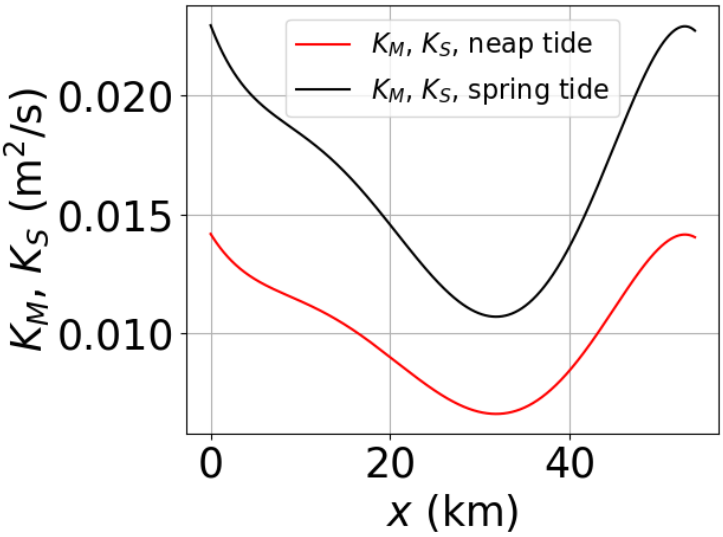

[a]

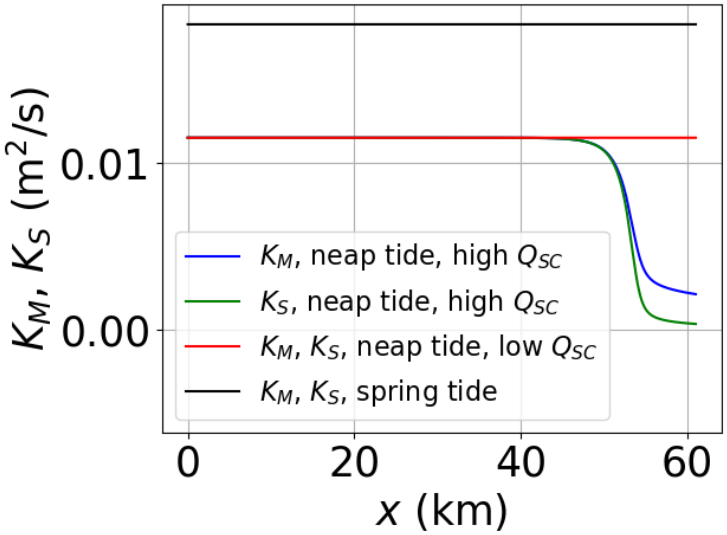

[b]

Figure 4.11: Plots of the eddy viscosity (K_M, a measure of internal friction) and diffusion coefficient (K_S, a measure of turbulent mixing of salt) for the South Passage ([a]) and the North Passage ([b]). Except for the situation neap tide and high river discharge in the North Passage, K_M and K_S are the same. In the South Passage, K_M (and K_S) is the same for low and high river discharge and is only different for a different tidal current. In the North Passage, K_M (and K_S) is the same for both cases (low and high river discharge) during spring tide, but different for the two cases (low and high river discharge) during neap tide.

4.2 The effect of the Deepwater Navigation Channel

As mentioned in Section 1.2, the Deepwater Navigation Channel (DNC, which is part of the Deep Waterway Project) possibly influences salt intrusion. Therefore, the reference case (which is the present-day situation) is compared with the situation before the DNC. This is done for spring tide and low river discharge. In order to model the situation before the DNC, the North Passage is made 1 m shallower (12.1 m instead of 13.1 m) than the present-day case and the width of the North Passage before the DNC and the present-day width are shown in Figure 4.12. Before the DNC, the North Passage had a funnel-shape, just like the South Passage has. During the realisation of the DNC, the North Passage was narrowed and now the channel has a straight shape. In order to separate the effect of the deepening and the narrowing, three situations are compared: the situation before the DNC; the situation before the DNC, but with the present-day depth and the present-day situation. There are only differences in parameter values for the North Passage, the parameter values for the South Channel and South Passage are the same for all three situations.

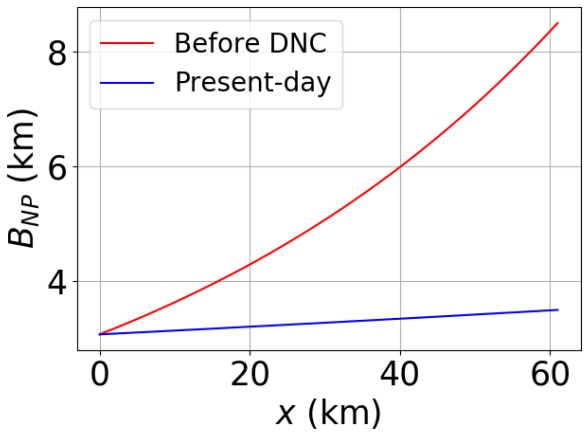

Figure 4.12: Plot showing the width before the existence of the DNC and the present width.

4.2.1 River water and salt transports

Figure 4.13 show the results for river transport in the South Passage and the North Passage and salt transport from the South Passage into the North Passage respectively. The situations that are considered are: the situation before the DNC; the

situation before the DNC, but with the present-day depth (H_{NP} =13.1 m) of the North Passage (so here only the funnel-shape is different from the present situation) and the present-day situation. In Figure 4.13, the percentages indicate the nWDR for a specific channel. The nWDR gives the percentage of the total river transport that is transported through a specific channel and is defined by Equation (2.42).

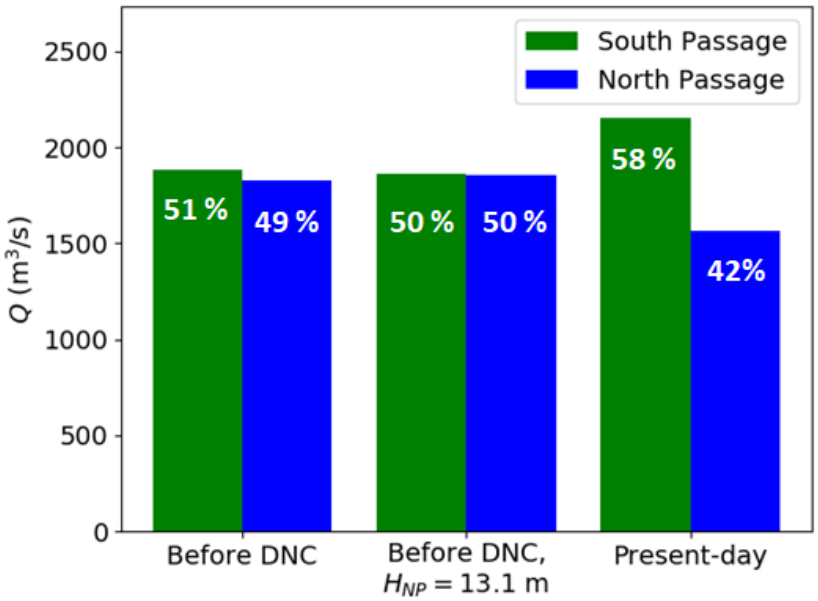

Figure 4.13: River transports through the South Passage and the North Passage for the situation before the DNC; the situation before the DNC, but with the present-day depth of the North Passage (H_{NP} =13.1 m) and the present-day situation. Percentages indicate the nWDR for a specific channel. The nWDR gives the percentage of the total river transport that is transported through a specific channel and is defined by Equation (2.42).

Again, Equation (7.71) gives reasonable approximations for the nWDR in the South Passage and North Passage under the different conditions. The found nWDR values for the South Passage are before DNC: 50%, before DNC, H_{NP} =13.1 m: 49% and present day (reference case): 57%. However, this time the physical interpretation is more clear from the experiments themselves. Considering the situation before the DNC, Figure 4.13 suggests a slight increase in river transport through the North Passage after this channel was deepened (to H_{NP} =13.1 m). Due to the increased depth of the North Passage there is more space for river

water to flow through this channel and this possibly explains the increase in river transport here. However, this increase is small and most of the change in river transport between the pre-DNC and the present-day situation is explained by the narrowing of the North Passage. The Figure suggests that this narrowing decreases the river water transport through the North Passage. Probably, the reason for this change is that there is simply less space for river water in the North Passage after it became narrower.

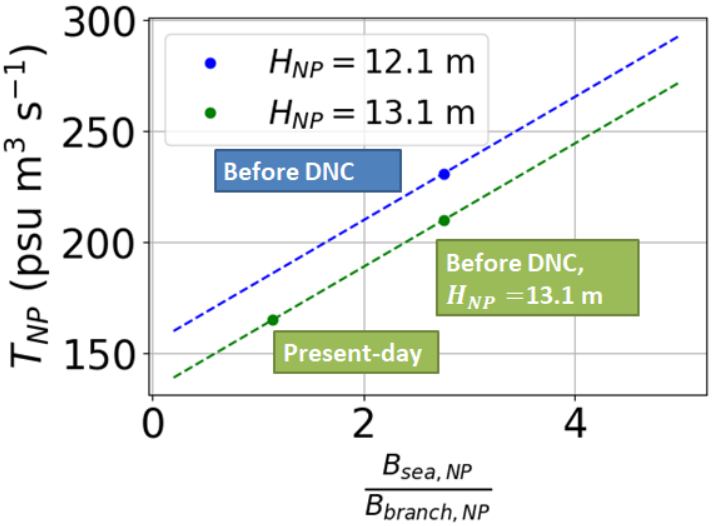

Figure 4.14: Salt transport (T_{NP}) from the South Passage into the North Passage against the ratio $\frac{B_{sea,NP}}{B_{branch,NP}}$, where $B_{sea,NP}$ is the width of the North Passage at sea and $B_{branch,NP}$ is the width of the North Passage near the branching point. A larger $\frac{B_{sea,NP}}{B_{branch,NP}}$, means that the North Passage is more funnel-shaped and less straight. The points show the results that are found for T_{NP} and the dashed lines suggest possible trends in these results. Separate lines are given for the two considered depths of the North Passage; H_{NP} =12.1 m and H_{NP} =13.1 m. The points correspond to the different situations and these different situations (before DNC; before DNC, H_{NP} =13.1 m and present-day) are indicated.

In Figure 4.14 the salt transport from the South Passage into the North Passage (T_{NP}) is plotted against $\frac{B_{sea,NP}}{B_{branch,NP}}$, where $B_{sea,NP}$ is the width of the North Passage at sea and $B_{branch,NP}$ is the width of the North Passage at the branching point. When the ratio $\frac{B_{sea,NP}}{B_{branch,NP}}$ increases, this means that the North Passage is less straight and more funnel-shaped. The points show the results that are found for T_{NP} and the lines suggest possible trends in these results. Lines are plotted for

different depths of the North Passage; one line for H_{NP} =12.1 m and one for H_{NP} =13.1 m. The situation before the DNC; before the DNC, but with the present-day depth (13.1 m) of the North Passage and the present day situation all correspond to a point and these situations are indicated in the figure. In all cases there is salt transport from the South Passage into the North Passage (as $T_{NP} > 0$ for all situations). From Figure 4.14, it appears that the salt transport from the South Passage, into the North Passage is smaller when the North Passage is deeper. Also, it seems that the salt transport increases when $\frac{B_{sea,NP}}{B_{branch,NP}}$ increases. So when the North Passage is funnel-shaped instead of straight, there is more salt transport from the South Passage into the North Passage. As the North Passage was (more) funnel-shaped before the DNC was realised, there used to be more salt transport from the South Passage into the North Passage at that time. Possible explanations for these observations are given when discussing salt intrusion (Section 4.2.2).

4.2.2 Salt intrusion

Figure 4.15 shows the distance between the branching point and the $\overline{s}$ =5 psu-line (L_5) against $\frac{B_{sea,NP}}{B_{branch,NP}}$ for the South Passage ([a]) and in the North Passage ([b]). A larger $\frac{B_{sea,NP}}{B_{branch,NP}}$, means that the North Passage is more funnel-shaped and less straight. A smaller value for L_5 means more salt intrusion. The points indicate results that are found for L_5 and the dashed lines indicate possible trends in those results. The points correspond to the different situations and these different situations (before DNC; before DNC, H_{SP} =13.1 m and present-day) are indicated.

The figure indicates that salt intrusion, in both the South Passage and the North Passage, was larger (L_5 was smaller) before the realisation of the DNC than it is nowadays. According to the figure, salt intrusion seems to increase for increasing $\frac{B_{sea,NP}}{B_{branch,NP}}$. Physically, this means that there is an increase in salt intrusion in both channels when the North Passage is more funnel-shaped. As the North Passage is straighter (less funnel-shaped) in the present day situation, than before the DNC, there is less salt intrusion in the present-day situation. Why there is more salt intrusion when the North passage is funnel-shaped is explained as follows: when the North Passage is funnel-shaped, the width of this channel is larger near the ocean, then when it is straight. Due to this larger width, the river transport is distributed over a larger area and consequently the river flow is weaker. Because of this weaker river flow, there will be less export of salt out of the North Passage and salt intrusion will increase. The larger salt intrusion in the South Passage, when the North Passage has a funnel-shape, is explained by the decrease in river transport through the South Passage (in Figure 4.13 the river transport through the South Passage is smaller for the situation before the DNC, where the North

Passage has a funnel-shape, than for the present-day situation). Due to the smaller river transport (and consequently weaker river flow), less salt is transported out of the South Passage and salt intrusion is increased there. In Section 4.2.3 it will be shown that the river flow is indeed larger for the situation before the DNC (where the North Passage has a funnel-shape) than for the present-day situation (where the North Passage is straight).

Using the observations described above, it can also be explained why there is more salt intrusion in the South Passage than in the North Passage (the larger salt intrusion in the South Passage was mentioned in Section 3.2). For the present-day situation, the South Passage has a funnel-shape and the North Passage is straight. Due to the funnel-shape of the South Passage, river flow will be weaker there (than when the South Passage would be straight), as the river transport is distributed over a larger area near the sea. Due to the weaker river flow, there is more salt intrusion. Salt intrusion in the North Passage might also be larger because of the funnel-shape of the South Passage (due to the resulting increase in river transport through the North Passage). However, based on the observations above, the funnel-shape of the South Passage is expected to increase the salt intrusion in the South Passage itself much more than it increases salt intrusion in the North Passage. According to Figure 4.15, for the situation before the DNC, there also was more salt intrusion in the South Passage than in the North Passage. This can be explained in the same way as was done above for the present-day situation. Before the existence of the DNC, the North Passage was (more) funnel-shaped than nowadays, but still the South Passage was more funnel-shaped (had a smaller convergence length scale) than the North Passage (see Table 2.1 and 2.3).

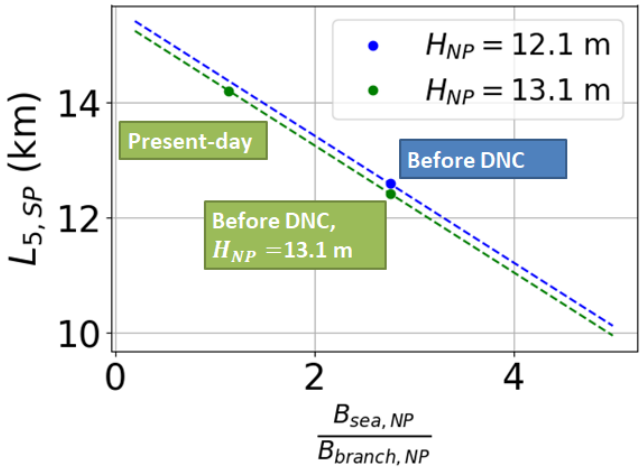

[a]

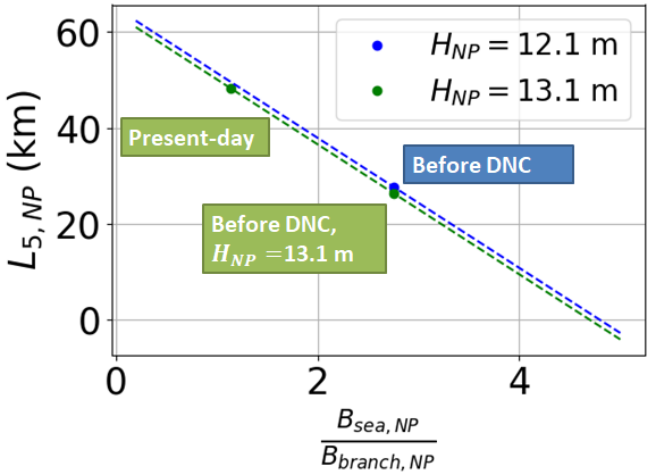

[b]

Figure 4.15: Distance (L_5) between the branching point and the $\overline{s}$ =5 psu-line against against $\frac{B_{sea,NP}}{B_{branch,NP}}$ for the South Passage ([a]) and in the North Passage ([b]). Here, $B_{sea,NP}$ is the width of the North at sea and $B_{branch,NP}$ is the width of the North Passage at the branching point. A larger $\frac{B_{sea,NP}}{B_{branch,NP}}$, means that the North Passage is more funnel-shaped and less straight. When L_5 is smaller, there is more salt intrusion. The points indicate results that are found for L_5 and the dashed lines indicate possible trends in those results. The points correspond to the different situations and these different situations (before DNC; before DNC, H_{SP} =13.1 m and present-day) are indicated. Separate lines are given for the two considered depths of the North Passage; H_{NP} =12.1 m and H_{NP} =13.1 m.

Figure 4.15 also suggests that there is slightly more salt intrusion in both channels when the North Passage is deeper. For the North Passage, this is probably ex-

plained by an increase density-driven flow, which is stronger when the channel is deeper (see also Equation (2.17)). As the density-driven flow causes a net import of salt, a stronger density-driven flow results in more salt intrusion. For the South Passage the increase in salt intrusion (when the North Passage is deeper) is possibly explained by the smaller salt transport from the South Passage to the North Passage (see Figure 4.14). The deeper North Passage (in the present-day situation) would increase the salt intrusion in the present-day situation with respect to the situation before the DNC. However, this increase in salt intrusion due to the deeper North Passage nowadays is very small, a lot smaller than the decrease in salt intrusion due to the straightening of the North Passage.

Furthermore, the increase in salt intrusion for increasing $\frac{B_{sea,NP}}{B_{branch,NP}}$ (suggested by Figure 4.15) also explains the increasing salt transport from the South Passage to the North Passage for increasing $\frac{B_{sea,NP}}{B_{branch,NP}}$ (this was found in Figure 4.14). As there is more salt intrusion in the South Passage when $\frac{B_{sea,NP}}{B_{branch,NP}}$ is larger (i.e. when the North Passage is more funnel-shaped), there is more salt available in the South Passage to be transported to the North Passage. Similarly, the increase in salt intrusion in the South Passage for larger depth of the North Passage (observed in Figure 4.14) possibly explains the increase salt transport from the North Passage into the South Passage (see Figure 4.14).

Finally, Figure 4.16 shows the depth averaged salinity ($\overline{s}$) profiles for the South Passage ([a]) and the North Passage ([b]) for the different situations (before the DNC; before the DNC, but H_{NP} =13.1 m and present-day). For the South Passage, there is almost no change in depth averaged salinity when the North Passage is made 1 m deeper so that H_{NP} =13.1 m (i.e. the black and the green line are almost the same). There is a slightly less salinity in the South Passage for the present-day situation, than for the other two situations. So this figure also suggests that the straightening of the North Passage caused a very slight decrease in salt intrusion in the South Passage. When the situation before the DNC is considered, for the North Passage there is a very small increase in salinity when the depth of the North Passage is increased to 13.1 m (i.e. when going from the black line to the green line). However, the figure shows that the depth-averaged salinity is a lot lower for the present-day situation than for the situation before the DNC, indicating that the straightening of the North Passage lowered the depth averaged salinity in this channel considerably.

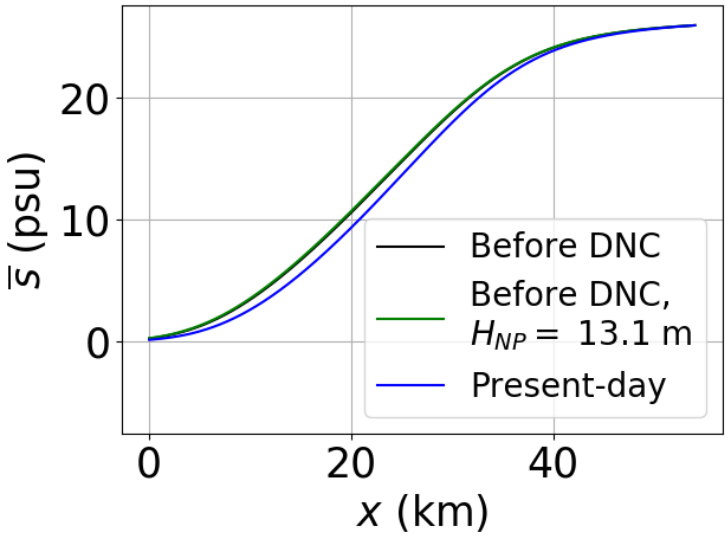

[a]

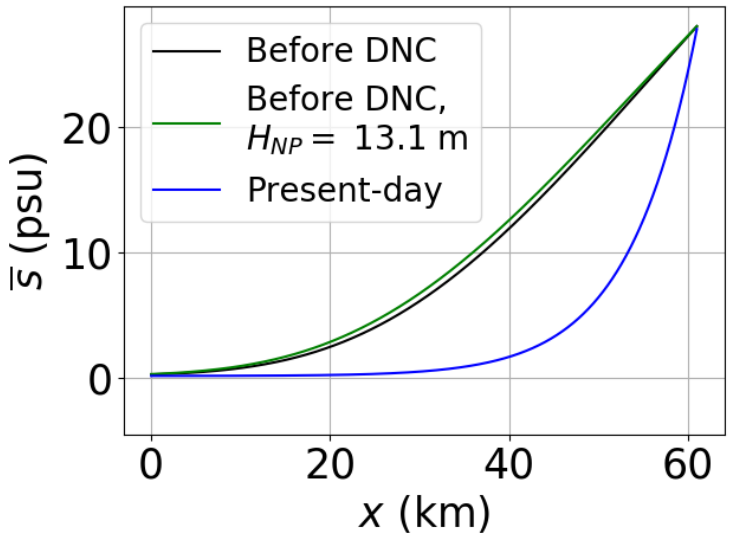

[b]

Figure 4.16: Profiles of depth-averaged salinity ($\overline{s}$) for the South Passage ([a]) and the North Passage ([b]) for the situations: before DNC; before DNC, but with H_{SP} =13.1m and present-day situation.

4.2.3 River and density-driven flow

Figure 4.17 shows river flow ($\overline{u}$, solid lines) and density-driven flow (u_E, dashed lines) in the South Passage ([a]) and the North Passage ([b]) for the different situations considered in this section. Figure 4.17a shows that the realisation of (elements of) the DNC has no effect on density-driven flow in the South Passage.

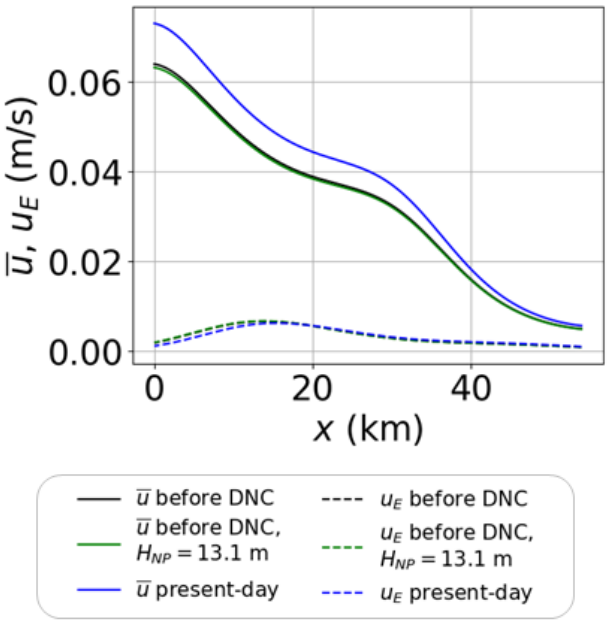

[a]

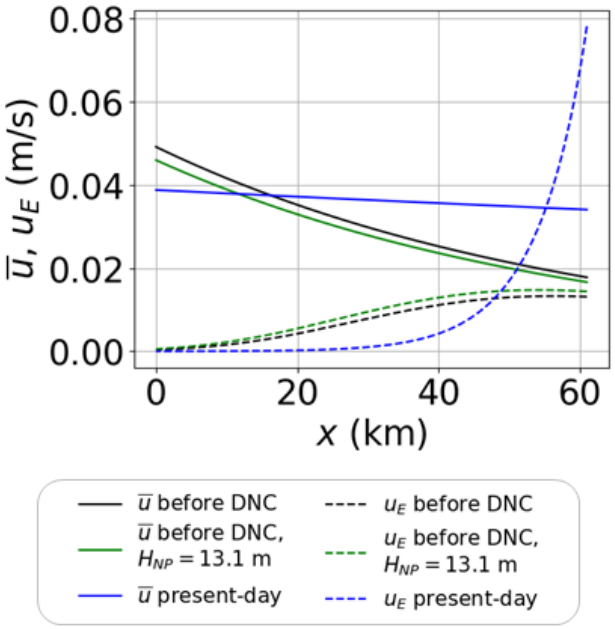

[b]

Figure 4.17: River flow ($\overline{u}$, solid lines) and density-driven flow (u_E, dashed lines) against x for the South Passage ([a]) and the North Passage ([b]). The following situations are considered: before the DNC; before the DNC, but with H_{SP} =13.1m and the present-day situation.

Also, there is almost no change in river flow in the South Passage when, from the situation before the DNC, the depth of the North Passage is increased to 13.1 m (the black and the green line are almost the same). Furthermore, the figure shows that there is an increase in river flow in the South Passage when going from the situation before the DNC to the present-day situation. As the increase in depth of the North Passage has (almost) no effect on the river flow in the South Passage, this increase is (almost) completely caused by the straightening of the North Channel. The increase in river flow for the present-day situation (compared to the pre-DNC situation) is explained by the larger river transport through the South Passage for the present-day situation (see Figure 4.13).

For the North Passage, there is a little decrease in river flow and a little increase in density driven flow when (starting from the situation before the DNC) the depth of the North Passage is increased to 13.1 m. The decrease in river flow is caused by the larger depth of the channel (remember that $\overline{u} = \frac{Q}{BH}$, see Equation (2.10)). Due to this larger depth, the river transport is distributed over a larger area and therefore the river flow weakens. The river flow nowadays is (in most of the North Passage) larger than during the situation before the DNC. As the increased depth of the North Passage has little effect on river flow, this increase is caused by the straightening of the North Passage. Consequently, the river transport is distributed over a smaller area (than before the DNC) and this results in a stronger river flow. Due to this stronger river flow, there is more export of salt and consequently there is less salt intrusion nowadays than before the DNC (as described in Section 4.2.2). The decrease in river flow for the present-day situation (compared to the situation before the DNC) in a small part of the North Passage is caused by the decrease in river transport in the North Passage (Q, see Figure 4.13).

Near the mouth of the North Passage, the density-driven flow largely increased after the DNC intervention. The figure indicates that the increase in depth of the North Passage only causes a small increase in density-driven flow. Therefore, this increase in density driven flow is largely caused by the narrowing of the North Passage. It is visible from Figure 4.16 that horizontal gradients in depth-averaged salinity in the North Passage increase due to the narrowing of the channel. These larger horizontal gradients in depth-averaged salinity possibly explain the increase in density-driven flow (see Equation (2.17)). In part of the North Passage, there is a decrease in density-driven flow (for the present-day situation compared to the other situations), which is caused by the decrease in salt intrusion (see Figure 4.15) and the resulting smaller horizontal gradients in salinity.

4.2.4 Distribution of currents

Next, it is investigated what the effect of the DNC is on the distribution of currents. To do that, Figure 4.18 shows the subtidal current difference (δu) between a certain situation and the reference case (present-day situation) for the South Passage. The situations that are considered are: the situation before the DNC and the situation before the DNC, but with the depth of the North Passage increased to H_{NP} =13.1 m. Figure 4.19 is a similar figure for the North Passage. Figure 4.18 shows that, in the South Passage, river flow was weaker in the situation before the DNC, than in the present-day situation. This was also indicated by Figure 4.17. In other words, due to the DNC, river flow became stronger in the South Passage. It is observed than δu is slightly more negative for the situation before the DNC, but with H_{NP} =13.1 m than for the situation before the DNC. For this reason it is concluded that the increase in depth of the North Passage weakens the river flow in the South Passage. And the stronger river flow in the present-day situation appears to be caused by the straightening of the North Passage. These changes are also visible in Figure 4.17.

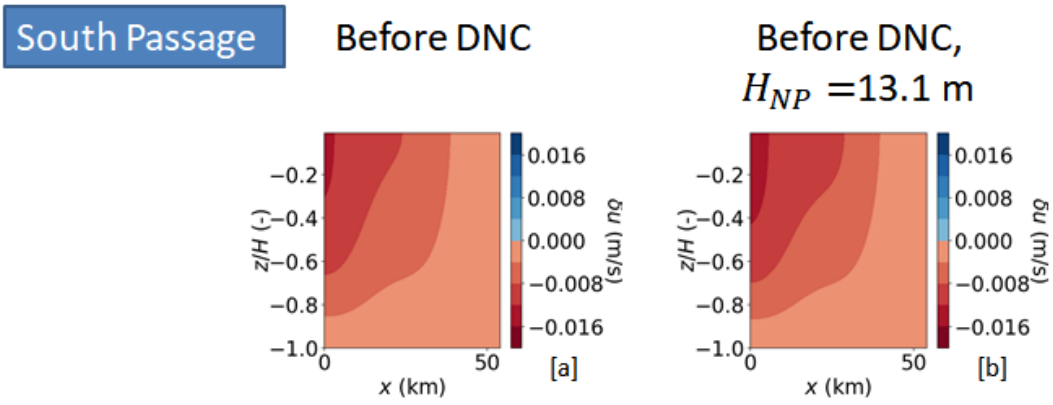

Figure 4.18: Subtidal current difference (δu) between a certain situation and the reference case (present-day situation) for the South Passage. The different situations that are shown are the situation before the DNC and the situation before the DNC, but with the depth of the North Passage increased to H_{NP} =13.1 m. Blue indicates an increase and red a decrease in tidal current with respect to the reference case.

For the North Passage, it seems that the density-driven flow was weaker in the situation before the DNC than the present-day situation. This can be recognised in the figure by the two cells with an increase in velocity near the bottom and a decrease in velocity near the top (the density driven flow consists of a seaward,

positive current near the surface and a landward, negative current near the bottom). Also, the figure indicates that river flow is weaker in most of the North Passage and stronger near the branching point for the situation before the DNC (compared to the present-day situation). These things were also observed from Figure 4.17. When, from the situation before the DNC, the depth of the North Passage is increased to its present-day value (H_{NP} =13.1 m), this seems to have very little effect on the current distribution in the North Passage. The river flow is slightly weaker when the depth of the North Passage is increased, just as observed in Figure 4.17.

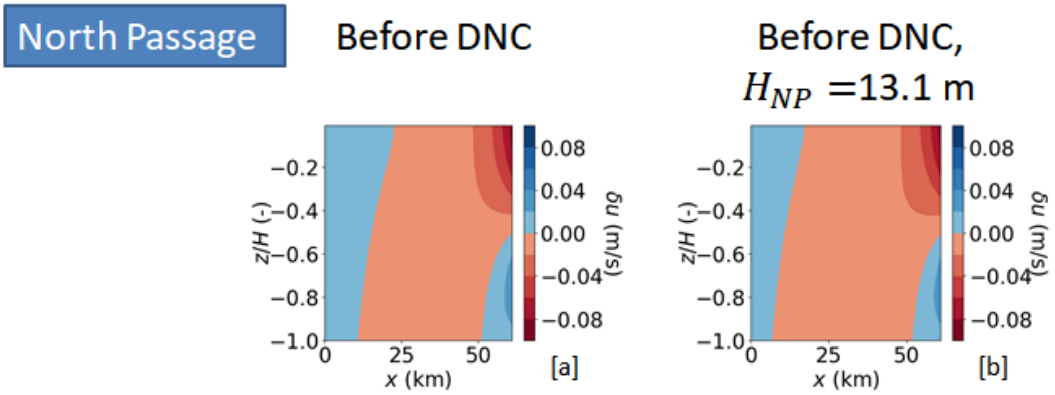

Figure 4.19: Subtidal current difference (δu) between a certain situation and the reference case (present-day situation) for the North Passage. The different situations that are shown are the situation before the DNC and the situation before the DNC, but with the depth of the North Passage increased to H_{NP} =13.1 m. Blue indicates an increase and red a decrease in tidal current with respect to the reference case.

4.2.5 Salinity distribution

Now, it is studied what the effect of the DNC is on salinity distribution. In order to do that, Figure 4.20 shows the salinity distribution in the South Passage for the situation before the DNC; the situation before the DNC, but with present-day depth of the North Passage and the present-day situation. Figure 4.20 is a similar figure, but for the North Passage. For both the South Passage and the North Passage, in all cases, the lines of equal salinity are rather vertical, indicating that there is a lot of mixing and the density-driven flow is weak. Therefore, in all situations horizontal diffusion seems to be the dominant mechanism for salt intrusion. In the South Passage, (elements of) the DNC seem to have little effect on the salinity distribution. When looking very carefully to the figure, it is observed that there

was slightly more salt intrusion before the DNC, than the salt intrusion present-day. This was also concluded from Figure 4.15. The effect of the deepening of the North Passage (to H_{NP} =13.1 m) on the salinity distribution in the South Passage is not visible.

In the North Passage, it is clear from Figure 4.21 that there was more salt intrusion before the DNC than nowadays. Also, salt intrusion increases slightly when for the situation before the DNC the depth of the North Passage is increased to its present-day value (H_{NP} =13.1 m). These results were also found from Figure 4.15.

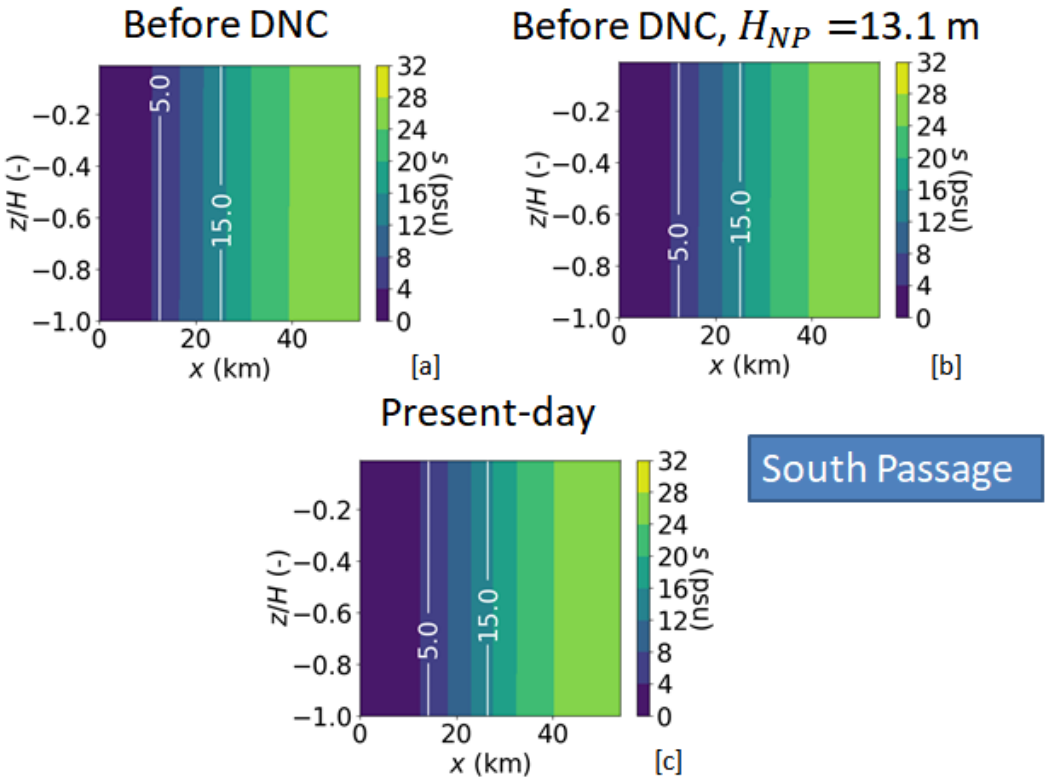

Figure 4.20: Salinity distribution in the South Passage for different situations (before DNC ([a]), before DNC, but with present-day depth ([b]) of the North Passage (H_{NP} =13.1 m) and the present-day situation ([c]). The s =5 psu-line and the s =15 psu-line are indicated in white.

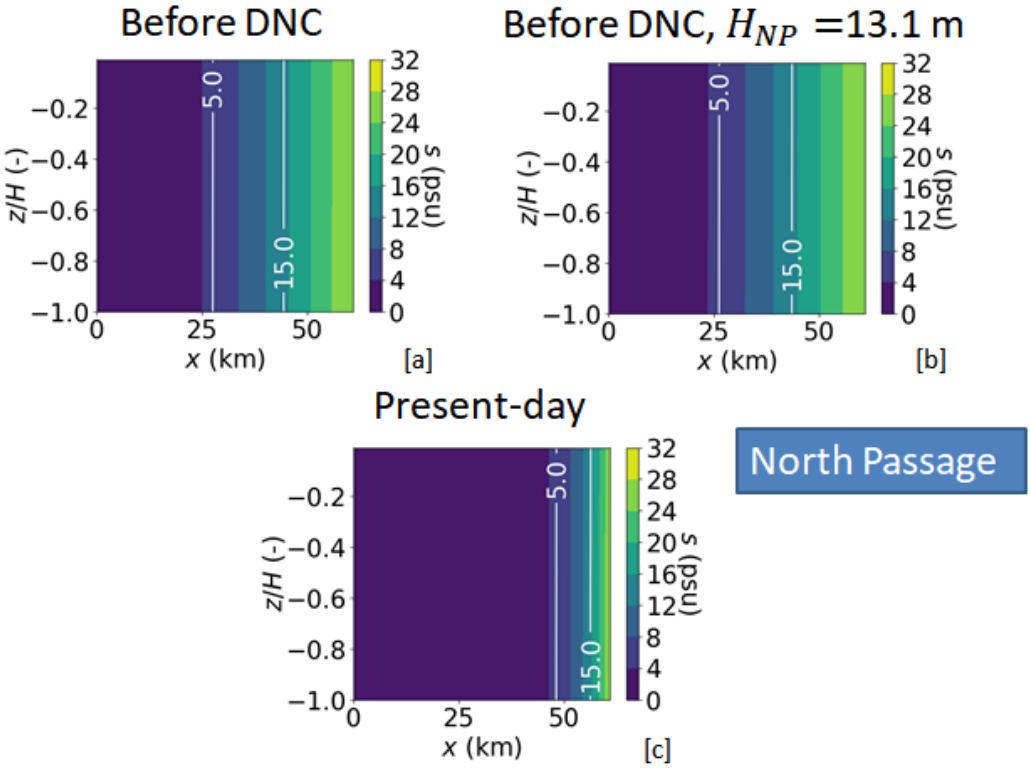

Figure 4.21: Salinity distribution in the North Passage for different situations (before DNC ([a]), before DNC, but with present-day depth ([b]) of the North Passage (H_{NP} =13.1 m) and the present-day situation ([c]). The s =5 psu-line and the s =15 psu-line are indicated in white.

4.2.6 Stratification

In order to study the effect of the DNC on stratification, Figure 4.22 shows the Richardson number (Ri_L) against x in the South Passage ([a]) and the North Passage ([b]) for the three different situations in this sections. Figure 4.23 is a similar figure for the stratification parameter (χ).

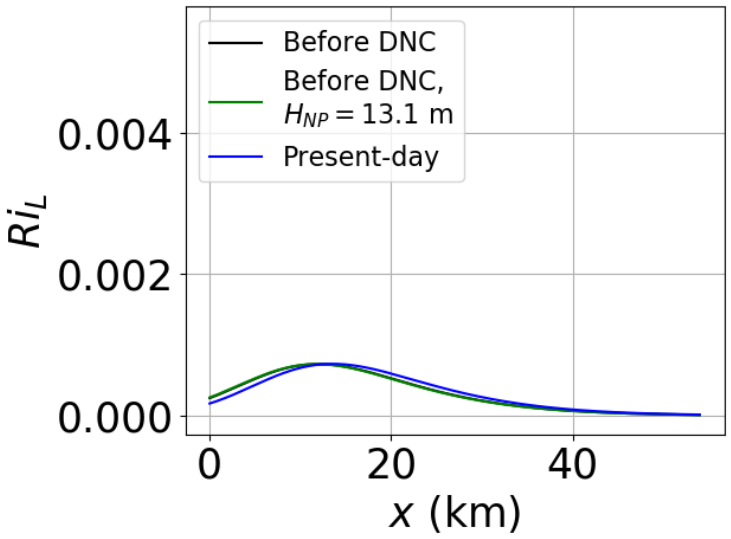

[a]

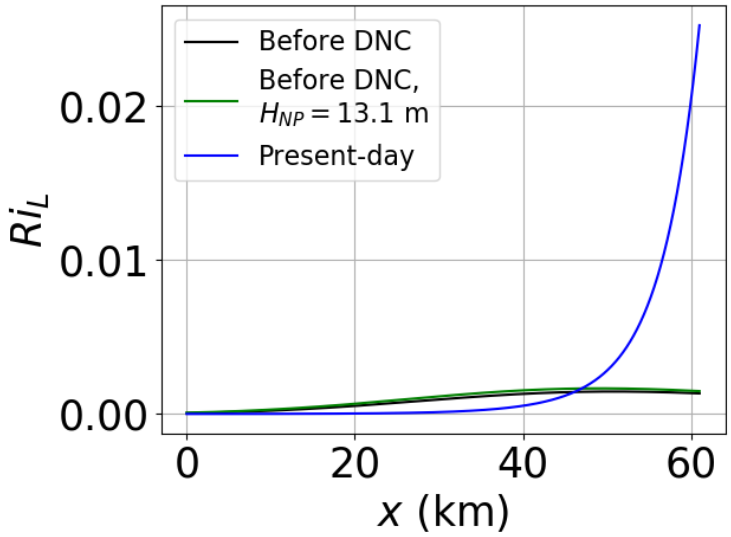

[b]

Figure 4.22: The Richardson number (Ri_L) for the South Passage ([a]) and the North Passage ([b]) for the situation before the DNC; the situation before the DNC, but with the depth of the North Passage increased to its present-day value (H_{NP} =13.1 m) and the present situation. A larger value for the Richardson number means more stratification.

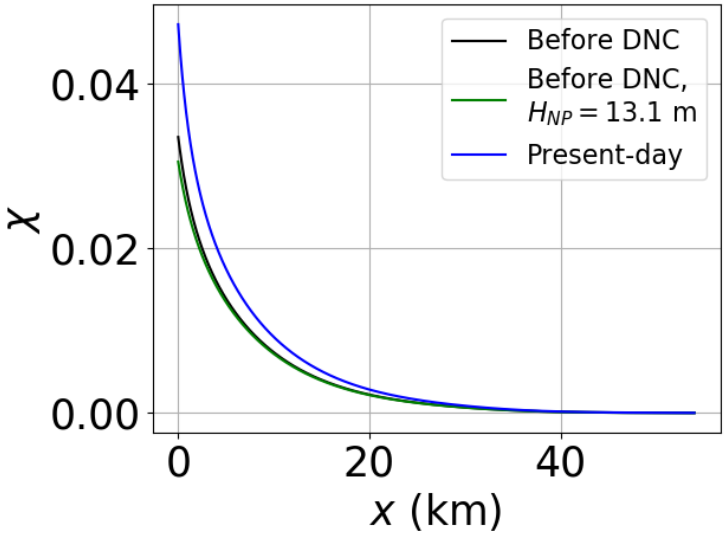

[a]

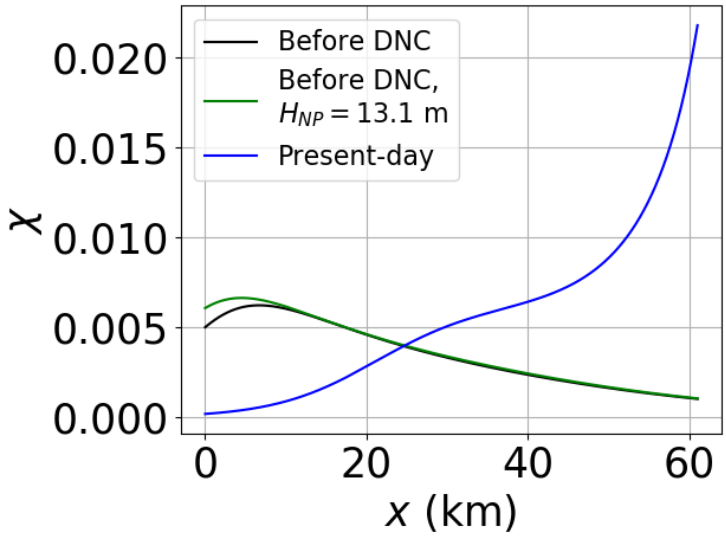

[b]

Figure 4.23: The stratification parameter (χ) for the South Passage ([a]) and the North Passage ([b]) for the situation before the DNC; the situation before the DNC, but with the depth of the North Passage increased to its present-day value (H_{NP} =13.1 m) and the present situation. A larger value for the stratification parameter means more stratification.

For the South Passage, Ri_L is (almost) the same for the three situations. The only very small difference is that the curve describing Ri_L for the present-day situation is shifted a bit more to the right compared to the other situations. This is possibly explained by a slightly smaller salt intrusion for the present-day situation (see Figure 4.15). For the North Passage, Ri_L for the situation before the DNC, but with the present-day depth is almost the same as Ri_L for the situation before the DNC, so the deepening of the North Passage during the realisation of the DNC has almost no effect on the stratification described by Ri_L. However, Ri_L near the ocean is a lot larger for the present-day situation than for the situation before the DNC. This is possibly explained by the larger density-driven flow (for the present-day situation compared to the situation before the DNC) there (according to *Monismith et al.* [1996], the gravitational circulation increases stratification). A bit further landwards Ri_L is smaller for the present-day situation the for the situation before the DNC. This is possibly, described by a smaller density-driven flow (for the present-day situation compared to the situation before the DNC) there (see Figure 4.17).

Figure 4.23 shows that, for the South Passage in the situation before the DNC, there is almost no change in χ when the depth of the North Passage is increased (to H_{NP} =13.1 m). However, χ is slightly higher for the present-day situation than for the situation before the DNC. This small increase in stratification, is likely explained by the increase in river flow due to realisation of the DNC (see Figure 4.17). In the North Passage, when starting with the situation before the DNC, there is only a slight local increase in χ when the depth of the North Passage is increased (to H_{NP} =13.1 m). In contrast, for the present-day situation in the North Passage, χ is a lot larger and has a very different distribution than in the situation before the DNC. This major change is probably explained by the much larger density-driven flow (near the ocean) and the larger river flow for the present-day situation in the North Passage (see Figure 4.17). Also, the density-driven flow and the river flow have a rather different distribution for the present-day situation than for the situation before the DNC.

4.2.7 Eddy viscosity and diffusion coefficients

For all situations (before DNC; before DNC, H_{NP} =13.1 m and present-day) in this section no iterations take place to determine the Richardson number (Ri_L) used to do the model calculations. In all cases the iteration to determine Ri_L is ended after the first calculation and Ri_L =0 is used for the calculations in the model. For the South Passage, the values for the tidal current and geometry of the channel are kept the same as for the reference case. Consequently, according to Equation (2.30a), (2.30b) and (2.30c), the vertical eddy viscosity (K_M, measure

of internal friction), the vertical diffusion coefficient (K_S, gives the strength of vertical turbulent mixing of salt) and the horizontal diffusion coefficient (K_{HS}, gives the strength of horizontal diffusion of salt) for the South Passage are exactly the same as for the reference case. The distributions and values of these parameters, for the reference case, are given in Figure 3.9, 3.10 and 3.11.

As the depth of the North Passage is constant (independent of x) and Ri_L =0 in the calculations, K_M and K_S are the same and also constant according to Equation (2.30a) and (2.30b). When the depth of the North Passage is H_{NP}=12.1 m (this is the case for the situation before the DNC), $K_M = K_S$ =0.0169 m^{2}s^{-1}. When H_{NP}=13.1 m (this is the case for the present-day situation),
$K_M = K_S$ =0.0183 m^{2}s^{-1}. So there is more turbulent mixing in the present-day situation than in the situation before the DNC.

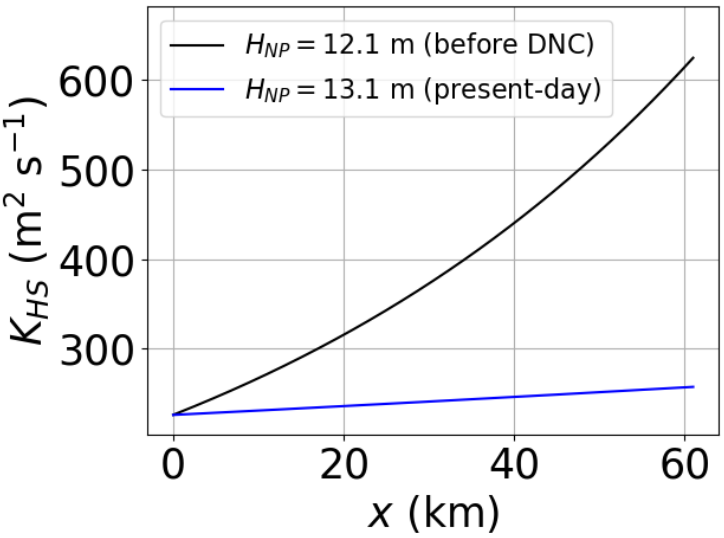

Figure 4.24: The horizontal diffusion coefficient (K_{HS}, a measure of horizontal diffusion of salt) for the North Passage. Separate lines for the two different depths (before the DNC: H_{NP} = 12.1 m and present-day situation: H_{NP} = 13.1 m) of the North Passage considered in this section are shown.

Figure 4.24 shows the horizontal diffusion coefficient (K_{HS}) for the North Passage. Separate lines for the two different depths (before the DNC: H_{NP} = 12.1 m and present-day situation: H_{NP} = 13.1 m) of the North Passage considered in this section are shown. As K_{HS} is linear in channel width B (when Ri_L =0, see Equation (2.30c)) and the North Passage was funnel-shaped before the existence

of the DNC, K_{HS} is generally larger for the situation before the DNC than for the present-day situation. Also, K_{HS} increases seawards for the situation before the DNC. Physically, this means that, before the DNC, there was more diffusion of salt near the ocean than near the branching point.

Chapter 5

Discussion

5.1 Choice eddy viscosity and diffusion coefficients

During this study other formulations for the vertical eddy viscosity (K_M) and vertical diffusion coefficient (K_S) have been tested, viz. those given in *MacCready* [2007]:

$$K_M = A_0 C_D U_T H, \tag{5.1a}$$

$$K_S = A_1 C_D U_T H(A_3 + \frac{1 - A_3}{1 + A_2 Ri_L}), \tag{5.1b}$$

In these equations A_0, A_1, A_2, A_3 and C_D are constants. As before, H is the depth, B the width and U_T the tidal current. These variables have the same values as for the reference case (the values that are given in Table 2.2 and 2.3). Two different values have been tried for A_0, namely A_0 =0.065 and A_0 =0.0325 (based on the study by *MacCready* [2007]). The values for the other constants are A_1 =0.022, A_2 =3.33, A_3 =0.3 and C_D =2.6×10^{-3} (these values are from *MacCready* [2007]).

In contrast to the formulations of *Munk and Anderson* [1948] (that are chosen for this study), in the formulations of *MacCready* [2007] only K_S depends on stratification. Figure 5.1 shows K_M (dashed lines) and K_S (solid lines) for Ri_L =0, i.e. when there is no stratification. When Ri_L =0, K_M and K_S have different values, while for the formulation by *Munk and Anderson* [1948] K_M and K_S are the same in that case. Also values for K_M and K_S are substantially lower for the formulations of *MacCready* [2007] (Figure 5.1) than for the formulation by *Munk and Anderson* [1948] (see Figure 3.9 and 3.10).

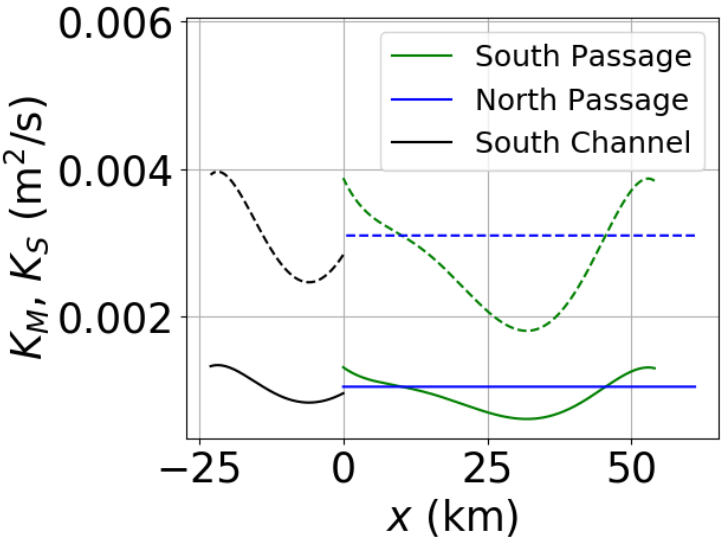

Figure 5.1: Plots of the vertical eddy viscosity (K_M, a measure of internal friction) and the vertical diffusion coefficient (K_S, a measure of vertical turbulent mixing of salt) versus distance x for the formulations of *MacCready* [2007] and Ri_L =0. Dashed lines show K_M and solid lines show K_S.

In Section 3.1, Figure 3.1 gives the flow diagram for the reference case (spring tide and dry season) when using the Munk and Anderson formulation. This flow diagram reveals a clear minimum value for the combined criterion, for a certain value of Q_{SP} and T_{SP}. Examples of flow diagrams when using the formulation by *MacCready* [2007] (also for spring tide, dry season and present-day situation) are shown in Figure 5.2. The two panels are each for a different value of A_0. The white dot shows the minimum value for the criterion $crit_{comb} = \sqrt{Crit_1^2 + Crit_2^2}$ (that should be minimized in order to obey the conditions at the branching point) and the corresponding values for Q_{SP} and T_{SP} are selected. A clear, consistent minimum (that is approached when resolution for Q_{SP} and T_{SP} is increased) is not found in the flow diagrams and therefore values found for Q_{SP} and T_{SP} are unreliable (they strongly depend on the resolution of Q_{SP} and T_{SP}). Moreover, when nevertheless, still values for Q_{SP} and T_{SP} are selected, very high values for the river transport through the South Passage are found for A_0 =0.065. For A_0 =0.0325, very low values for the river transport through the South Passage are found. The total river discharge is 3714 m^3/s here and the flow diagrams suggest that either, almost all river water flows through the South Passage (when A_0 =0.065, Figure 5.2a) or almost all river water flows through the North Passage (when A_0 =0.0325, Figure 5.2b). Physically this is not a realistic situation.

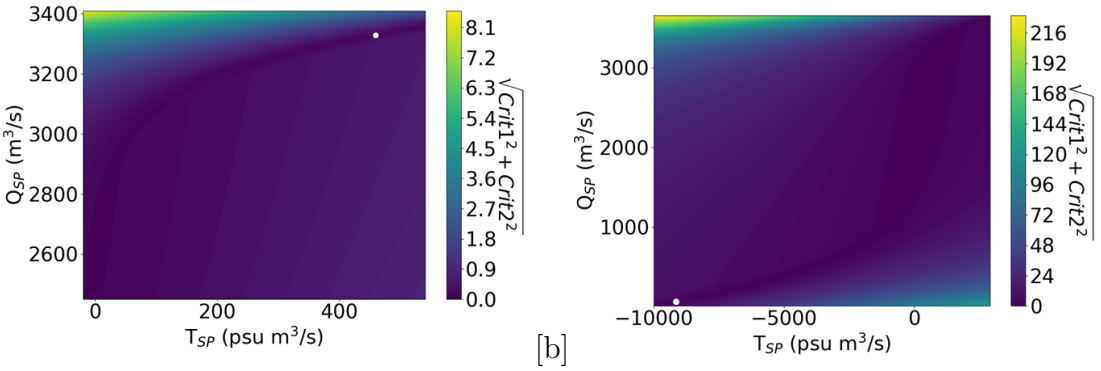

Figure 5.2: Flow diagrams when the formulations of *MacCready* [2007] are used for K_s and K_M. The river transport through the South Passage is called Q_{SP} and T_{SP} gives the salt transport from the North Passage into the South Passage (a negative value means transport from the South Passage into the North Passage). Two different values for A_0 are considered, viz. A_0 =0.065 ([a]) and A_0 =0.0325 ([b]). Both flow diagrams are for the reference case (spring tide, dry season, present-day situation) and the river discharge is Q_{SC} =3714 m^3 s^{-1} for these conditions. The white dot shows the minimum value for the criterion $crit_{comb} = \sqrt{Crit_1^2 + Crit_2^2}$. These minima are unreliable as they strongly depend on the resolution of Q_{SP} and T_{SP}.

One possible explanation for the absence of consisitent minima (that are approached when resolution is made better) for $crit_{comb}$ in Figure 5.2 is that the iterations for determining Ri_L (see Section 2.4 and Figure 2.5) are not working properly. In order to check whether this was the case, the runs were conducted for both the formulations of *Munk and Anderson* [1948] and *MacCready* [2007], but this time with fixed Ri_L =0. Exactly the same problem showed up for these runs, indicating that there is another reason for these problems. Other possible explanations remain that have not been analysed yet. For instance, it is possible that K_M and K_S should be the same when Ri_L =0, as is the case for the formulations of *Munk and Anderson* [1948]. A way to test this is by starting from the formulations of *Munk and Anderson* [1948] and then systematically lowering K_S with respect to K_M.

5.2 Comparison with literature

5.2.1 River and salt transport

As was shown in Section 4.1.1, the nWDR for the South Passage is 53% (spring tide) or 47% (neap tide) when river discharge is high and 58% (spring tide) or 66% (neap tide) when river discharge is low. These numbers are different from those found by *Alebregtse and de Swart* [2016], as they have found that, for both the dry season and wet season, approximately 50% of the river transport through the South Channel is transported to the South Passage and 50% to the North Passage. However the study by *Alebregtse and de Swart* [2016] is in several respects different from this study. For example, *Alebregtse and de Swart* [2016] do not consider salinity, but they do consider tides and non-linear effects.

For all cases studied in this thesis, a salt transport from the South Passage into the North Passage is found. This transport (almost) vanishes for neap tide. This is in agreement with the results by *Zhu et al.* [2018], as they have found overflow of water from the South Passage to the North Passage during spring tide and that this vanishes during neap tide. The salt transport from the South Passage to the North Passage originates from advection of salt by the overflow between these channels.

5.2.2 Salinity distribution and stratification

Figure 5.3 shows a salinity distribution at flood slack in the Yangtze Estuary found by *Zhu et al.* [2018]. In the latter study, a complex numerical model was used for the entire Yangtze Estuary. Model results turned out to agree fairly well with observations. The left panels are for spring tide and all the right panels are for neap tide. Panels a and b (the top panels) are for the surface layer and panels c and d (the bottom panels) are for the bottom layer. The river discharge in *Zhu et al.* [2018] (8000 m^3 s^{-1}) is that entering the whole estuary, whereas the river discharge in this study is the river water transport entering the South Channel, so these river discharges can not be compared directly. According to *Alebregtse and de Swart* [2016], the river transport through the South Channel is approximately 50% of the total river discharge for the dry season. Consequently, the river transport through the South Channel for Figure 5.3 is estimated to be 4000 m^3 s^{-1} and this is slightly higher, but comparable to the river discharges of 3714 m^3 s^{-1} used in this thesis for low river discharge. Therefore results for low river discharge in this study are compared to the results in Figure 5.3.

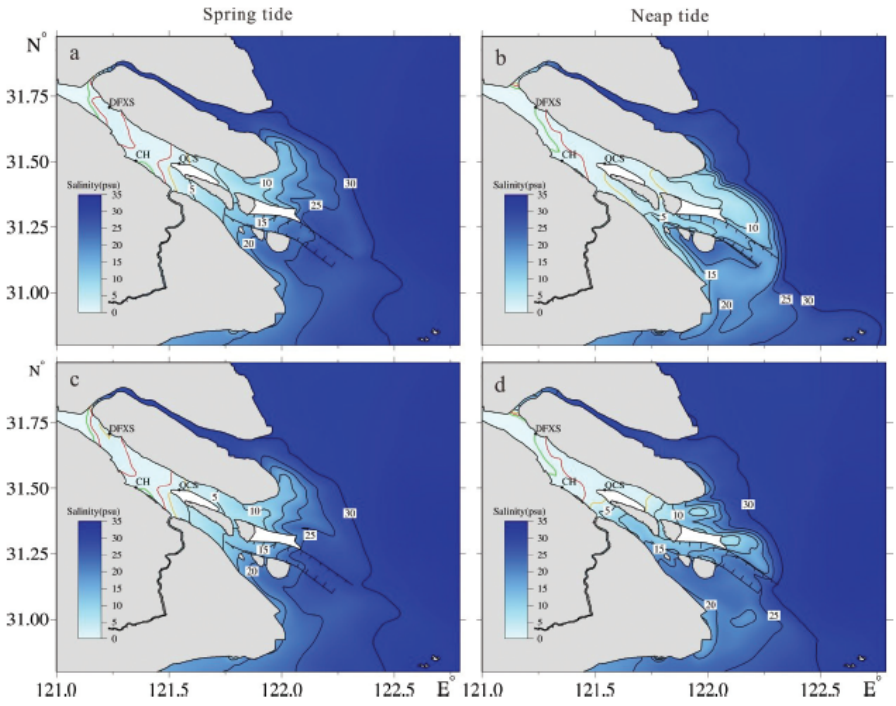

Figure 5.3: Salinity distributions at flood slack in the Yangtze Estuary found by *Zhu et al.* [2018] (Figure 10 in their paper). The left panels are for spring tide, the right panels for neap tide, panel a and b are for the surface layer and c and d are for the bottom layer. The river discharge for these results is 8000 m^3 s^{-1} at the upstream boundary. The river water transport in the South Channel is estimated to be 50% of that value, based on results of *Alebregtse and de Swart* [2016].

First, in this study, more salt intrusion was found for the South Passage than for the North Passage. This is also visible in Figure 5.3. Secondly, in the results in this thesis, the $\overline{s}$ =5 psu-line never reaches the branching point. However, from Figure 5.3, it is observed that the 5 psu-line lies in the South Channel (or close to the branching point in the surface layer during neap tide). This indicates that salt intrusion is underestimated by the model in this study.

Also, little stratification was observed in the results of this thesis. In contrast, in Figure 5.3 stratification is visible, especially for neap tide (the salinity distribution in the surface layer is different from the one in the bottom layer). Additionally, in this study, for the present-day situation, the highest Richardson number that is found for the South Passage is 0.003 (for neap tide and high river discharge) and that in the North Passage is just below 3 (for neap tide and high river discharge,

see Figure 4.9). For instance, *Chen* [2018] found a bulk Richardson number of 0.3 for spring tide and 2.0 for neap tide. From these comparisons, it seems that stratification is underestimated by the model of this study. However, both the results of this study and the Richardson numbers from *Chen* [2018] show that Richardson numbers are higher for neap tide than for spring tide, so the model seems to show that relation correctly.

From the experiments for this thesis, more salt intrusion is found when river discharge is lower. Also, it is found that salt intrusion generally increases when tidal current increases, except for the situation with high river discharge (in the North Passage). For this situation, in the North Passage, more salt intrusion is found for neap tide than for spring tide. Likewise, *Zhu et al.* [2018] have found that salt intrusion is stronger when there is a lower river discharge. They also have found increasing salt intrusion for increasing tidal currents, but for all river discharges.

5.2.3 Sensitivity of the results to DNC

In this study it is found that geometrical changes that were made during the realisation of the DNC lead to less salt intrusion. Also an increase in river flow is found in the South Passage and (most of) the North Passage. These changes are mainly the result of the straightening of the North Passage and there is little effect of the deepening of the North Passage. However, it is found by *Zhu* [2006] that the salinity in the South Passage increased due to the Deep Waterway Project (DWP) and the salinity in the North Passage decreased near the ocean and increased near the branching point. Furthermore, they have found a decrease in river flow in the South Passage and an increase in river flow in the North Passage due to the DWP.

A possible explanation for these differences is that in this project the depth of the North Passage is 1 m larger after the DNC, than before the DNC while *Zhu* [2006] used a larger increase in depth (2-3 m). As it is found in this study that the increase in depth has lead to more river water transport through the North Passage and more salt intrusion in the North Passage and the South Passage, it is plausible that the difference in depth increase explains (at least part of) the different results. Another possible explanation is that in this study only the geometrical changes due to the DNC are considered and tidal currents are kept the same. However tidal characteristics after the DNC are also different from those before the DNC. Also, some engineering structures are part of the Deep Waterway Project, such as groins and jetties and these might also influence for example local mixing. Lastly, it is possible that due to the underestimated stratification in the model of this thesis, the role of density-driven flow is underestimated. If this is the case then the effect of the deepening of the North Passage might be larger than suggested

by the results in this thesis (due to the depth dependence of the density-driven flow) and consequently, the increase in salt intrusion due to this deepening of the North Passage might be underestimated as well.

5.3 Increasing salt intrusion and stratification

As mentioned in Section 5.2.2, it seems that salinity and stratification are underestimated in the model. In order to get more insight into what can cause these underestimations, some results of additional exploratory experiments are discussed in this section.

The starting point of these experiments is the reference case (spring tide, low river discharge, present-day situation) as described in Section 2.6, but the following parameters are different: s_{ocn} =28 psu for all channels (from *Zhu et al.* [2018]), C_v is 2 times larger (0.002 instead of 0.001, C_v is a factor in the equations for K_M and K_S, see Equation 2.30a and 2.30b and the next paragraph, value C_v from *Huijts et al.* [2009]) and the factor in Equation (2.30c) (the equation for K_{HS}) is 1.5 times smaller (0.035 in stead of 0.0525, from *Guha and Lawrence* [2013]) than for the reference case. Then, five changes are considered to see if this yields results that are closer to those of *Zhu et al.* [2018].

First, it is possible that the vertical eddy viscosity (K_M, measure of internal friction) and diffusion coefficient (K_S, strength of turbulent mixing of salinity) are overestimated. This would result in an overestimation of mixing and an underestimation of stratification. For the reference case experiment values for K_M and K_S lie between 0.01 and 0.025 m^2s^{-1} (see Figure 3.9 and 3.10). Whilst in *MacCready* [2004], values K_M and K_S between 0.0004 and 0.01 m^2s^{-1} are used. Therefore, a different value of C_v has been considered.

Secondly, it is possible that the Richardson number (Ri_L) should have a larger influence on K_M and K_S or formulated differently, that the factors in front of Ri_L in the equations for K_M and K_S (Equation 2.30a and 2.30b) should be larger. Therefore, these factors were multiplied with a factor of 5.

A third possibility is that K_{HS} (measure of horizontal diffusion if salt) is underestimated. This would mean that salt import into the estuary by horizontal diffusion is underestimated and this would lead to an underestimation of salt intrusion. For the reference case experiment, K_{HS} has values between 190 and 2560 m^2s^{-1} for the South Passage and K_{HS} slightly varies around 240 and 390 m^2s^{-1} for the South Passage and South Channel respectively (see Figure 3.11). For this reason, the

third possible solution is to multiply the constant in K_{HS} with 1.5, such that K_{HS} increases.

A forth point of improvement in the model is that tidal straining is not taken into account. Tidal straining originates from the faster movement of water near the surface than near the bottom, due to vertical shearing of the tidal current. During ebb, this results in an increasing stratification, as fresh water near the surface flows over saltier water near the bottom (due to its higher current). This results in stronger stratification. During flood the faster movement near the surface will decrease stratification (even if mixing is absent) and this even leads to disappearance of the stratification generated during ebb. In this way, there is a periodic variation in stratification (see *Dyer* [1997] and *Simpson et al.* [1990] for more information). The net flow due to tidal straining is often hard to distinguish from density-driven flow as the parts of the flows due to tidal straining and horizontal density gradients reinforce each other and *Burchard and Hetland* [2010] has found that approximately two-thirds of the estuarine circulation originates from tidal straining and one-third from horizontal density-gradients. A way to take into account tidal straining is to increase the strength of the density-driven flow. Therefore, u_E is multiplied with a factor 1.5 to see if this makes a difference.

Lastly, considering the left panels of Figure 5.3, there is no clear single, suitable value for s_{ocn} (the salinity of the adjacent ocean). Considering the choice of the boundaries of the estuary in the model (see Figure 2.1) and comparing these with Figure 5.3, it seems that the salinity at the seaward boundaries for the South Passage is different from the one for the North Passage. Therefore implications of the choices $s_{ocn,SP} = 26$ psu, $s_{ocn,NP} = 28$ psu were considered.

In order to see how the different possible solutions influence salt intrusion, Figure 5.4 shows the distance (L_5) between the branching point and the $\overline{s}$ =5 psu-line in the South Passage ([a]) and the North Passage ([b]) for the reference case (Normal) and the five options that were considered. When there is more salt intrusion, L_5 is smaller. The red dashed line indicates the value for L_5 for the reference case. A little increase in salt intrusion is visible when C_v is reduced (here by a factor of 2), but for that possible solution, there is less salt intrusion in the South Passage. From both figures it is clear that only larger values of K_{HS} lead to more salt intrusion in both channels. Hence, it the underestimation of salt intrusion in the model is possibly caused by an underestimation of K_{HS} (horizontal diffusion). As tidal pumping is not taken into account in the model, this might also lead to an underestimation of salt import into the estuary. Possibly, increasing horizontal diffusion can compensate for (a part of) this underestimation.

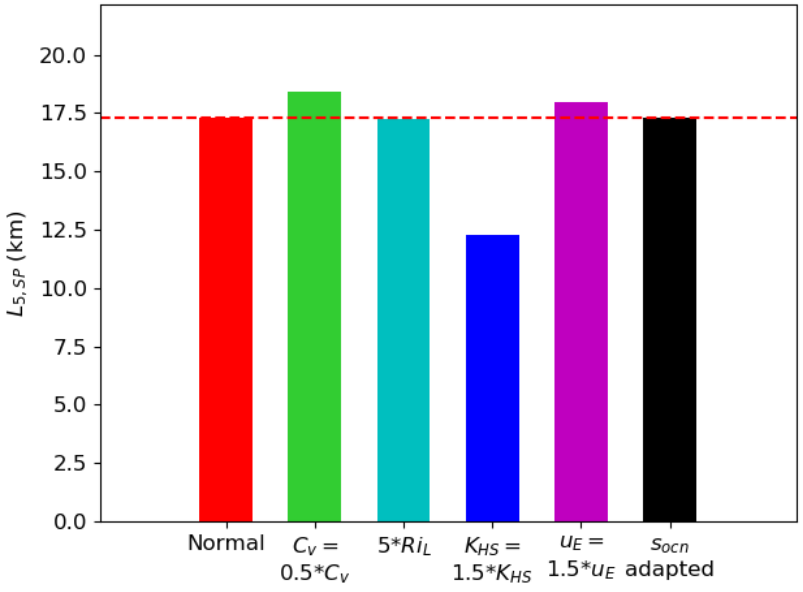

[a]

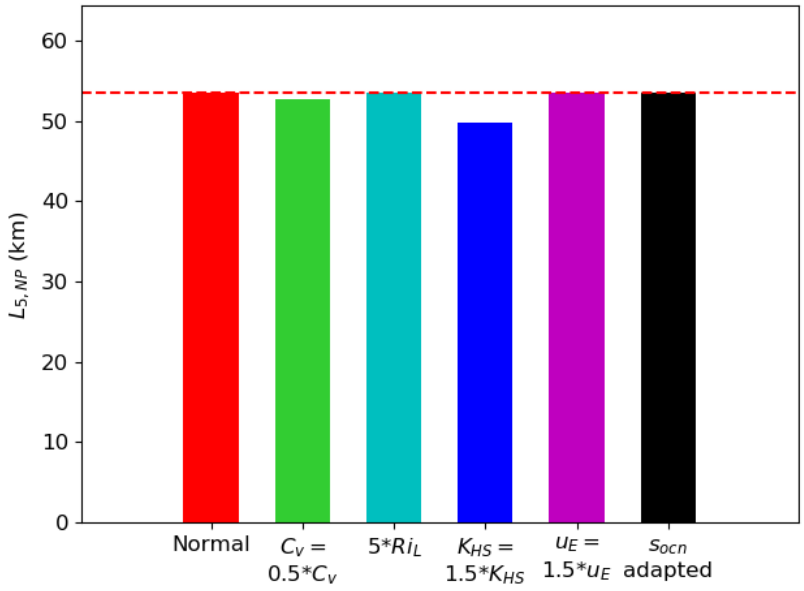

[b]

Figure 5.4: Distance (L_5) between the branching point and the $\overline{s}$ =5 psu-line in the South Passage ([a]) and the North Passage ([b]) for the reference case described in the text (Normal) and the five options that were considered (see text for explanation). A smaller value for L_5 means more salt intrusion. The red dashed line indicates L_5 for the normal (starting point) situation.

The effect of the different possible solutions on stratification is studied using Figure 5.5, showing the stratification parameter (χ) against x in the South Passage ([a]) and the North Passage ([b]) for the reference case and the five options that were considered. From the figure it appears that stratification is increase most in both channels by making C_v smaller (this decreases K_M and K_S) and it is possible that an overestimation of K_M and K_S (partly) explains the underestimation of stratification.

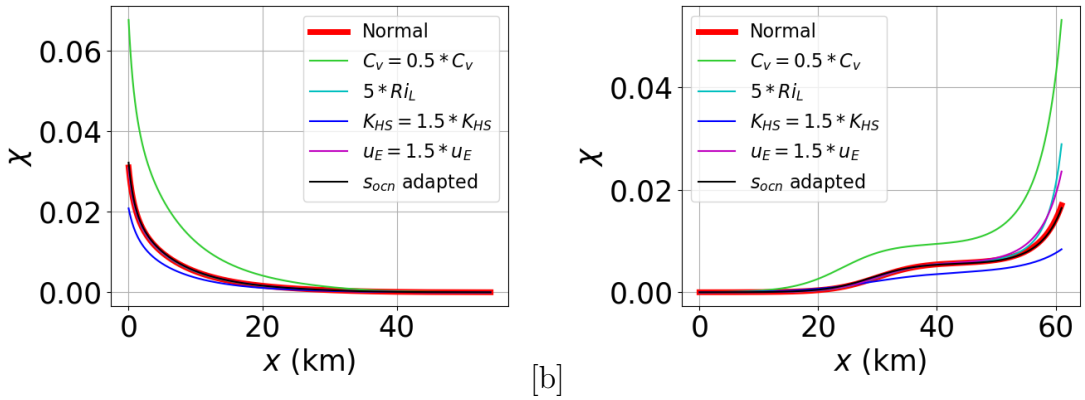

[a] [b]

Figure 5.5: Stratification parameter (χ) in the South Passage ([a]) and the North Passage ([b]) for the reference case described in the text (Normal) and the five options that were considered (see text for explanation). Equation (2.33) gives the definition of χ and a larger value for χ means more stratification.

5.4 Other points of improvement

There are more possibilities to improve the model. For example, different parameters in the model might be determined with higher precision. For example, for this study, channel depths have been estimated from a map. However, it might increase accuracy if measurements of channel depth are available. Another point of consideration is that it is assumed in the model that the sea surface height at the seawards boundary of the estuary is the same for the South Passage and the North Passage. However, it is likely that there is a difference between those sea surface heights. Furthermore, in the model, tidal currents are constant for a certain channel, but it might be interesting to see what changes when the tidal currents are dependent on x.

Finally, the tidal current and the net salt transport that they provide (through tidal pumping, see Section 1.1) are not explicitly accounted for in the model. Models

that explicitly take these processes into account are for instance *McCarthy* [1993] and *Wei et al.* [2017], but these models are only suitable for well mixed estuaries (see Section 1.3). A major opportunity for improvement is to combine the model in this study with such models in order to explicitly account for tidal currents and the corresponding salt transport.

Chapter 6

Conclusions

In this thesis, salt dynamics in estuarine networks have been studied. This was done by generalising an idealised subtidal model (formulated for a single channel estuary) to a network configuration. This model was applied to a prototype network configuration, viz. the South Channel, the South Passage and the North Passage of the Yangtze Estuary.

Regarding the first research question (*How does the idealised model perform in case of an estuarine network that consists of multiple channels?*) it is concluded that the model generally shows behaviour that is observed in the Yangtze Estuary. In particular, it shows that there is more salt intrusion in the South Passage than in the North Passage. The reason is that the South Passage is funnel-shaped and the North Passage is straight. Due to the funnel-shape, river flow is weaker as the river transport is distributed over a larger area near the ocean. This results in less export of salt. Also, a net salt transport from the South Passage to the North Passage is found (in case of spring tide). Furthermore, it is found that there is slightly more river transport through the South Passage than through the North Passage (except for high river discharge during neap tide). However, concerning the application of the model to the Yangtze Estuary, there are also still challenges to be met, as salt intrusion and vertical stratification are underestimated by the model.

Concerning the second research question (*How do results depend on key parameters in such a system, such as river discharge, tidal forcing, geometrical characteristics of the network?*) it was found that the river transport in all channels increases, when river discharge increases. This increase is larger for the North Passage than for the South Passage, due to a larger increase in stratification and consequently, a larger decrease in friction in the North Passage. Moreover, salt intrusion increases, in the South Passage and North Passage, when river discharge decreases. The rea-

son is, that less salt is transported away by river flow. For neap tide the increase is the largest in the South Passage and for spring tide it is the largest in the North Passage. Moreover, salt transport from the South Passage to the North Passage increases for decreasing river flow, because of the increase in salt intrusion in the South Passage. Furthermore, stratification increases for increasing river discharge.

Considering the case with low river discharge, the net water division ration (nWDR, river transport through a channel as percentage of the total river transport) for the North Passage is larger for spring tide than for neap tide. In contrast, for high river discharge, the nWDR for the North Passage is larger for neap tide than for spring tide. Furthermore, salt intrusion generally increases when tidal currents increase, due to an increase in horizontal diffusion. An exception to this relation is the situation with high river discharge (i.e. a river discharge of 6440 m^3 s^{-1} entering the South Channel). For this situation, in the North Passage, more salt intrusion is found for neap tide than for spring tide, due to a stronger density-driven flow during neap tide. Net salt transport from the South Passage to the North Passage practically disappears during neap tide. This is explained by the weaker salt intrusion in the South Passage during neap tide. Moreover, stratification is stronger for neap tide than for spring tide, due to less mixing during neap tide. Results are generally in agreement with those of *Zhu et al.* [2018], which where obtained using a complex numerical model. An exception is that the latter study increasing salt intrusion for increasing tidal current was found for all river discharges.

Finally the effect of the Deepwater Navigation Channel (DNC) on salt dynamics has been investigated. Only geometric changes due to the DNC are taken into account and low river discharge during spring tide is considered. Before the DNC, the North Passage had a funnel-shape and was 1 m shallower than it is today. During the realisation of the DNC the North Passage was made straighter and deeper. A smaller nWDR for the North Passage was found for the present-day situation than before the DNC. The reason is that there is less space for river water in the North Passage nowadays. Moreover, the straightening of the North Passage also caused a decrease in salt intrusion.This decrease in salt intrusion is larger for the North passage than for the South Passage. In the North Passage, this decrease in salt intrusion is explained by an increase in river flow, as the river transport has to flow through a smaller surface area near the ocean. In the South Passage an increase in river transport lead to the decrease in salt intrusion. The decrease in salt intrusion in the South Passage, due to the DNC, results in a decrease in salt transport from the South Passage to the North Passage. Finally, stratification in the North Passage has largely increased near the ocean due to the DNC. This

is explained by a stronger density-driven flow. More landwards the stratification in the North Passage decreased, due to a decrease in density-driven flow. For the South Passage there is little change in stratification, due to the DNC.

Chapter 7

Appendix

7.1 Derivation of model for a single channel configuration

7.1.1 Width averaging of starting equations

In these and the following sections a single channel is considered. In this section the basic equations will be averaged over width. In the next sections, from these width-averaged equations, the model that is used in this project is derived for a single channel. In Section 2.1 the model is generalised to a network model. A sketch of the situation in case of a single channel can be found in Figure 7.1. The bottom of the channel is located at $z = -H$ and the surface at $z = \eta$.

The starting equations are a set of equations including, the momentum balance in the x-direction[1], the salinity balance, mass balance, hydrostatic balance[2] and the equation of state. These basic Equations and their derivations can be found in multiple textbooks, for example *Gill* [1982] or *Cushman-Roisin and Beckers* [2011] and the equation of state can be found in for instance *MacCready* [2004]. For the x-momentum, mass and salt balance, the Boussinesq approximation (see for example *Cushman-Roisin and Beckers* [2011]) is applied. In this project these

[1]This equation will be written in conservative form (using the mass balance equation).

[2]This approximation can be used, because vertical length scales are a lot smaller than length scales in the x-direction, see for example *Cushman-Roisin and Beckers* [2011].

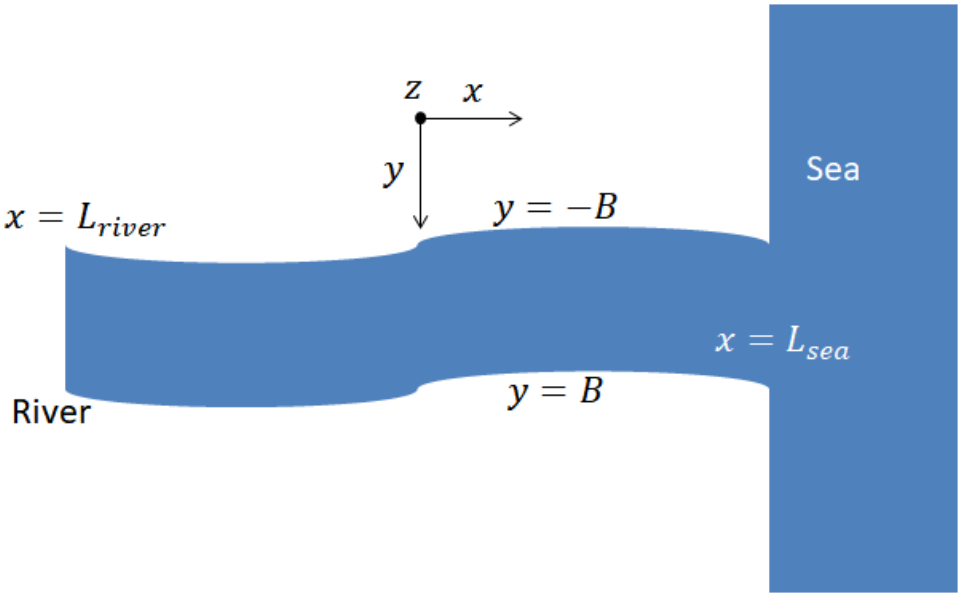

Figure 7.1: Sketch of the single channel.

equations are tidally-averaged. This set of equations is given by

$$\frac{\partial u_3}{\partial t} + \frac{\partial u_3 u_3}{\partial x} + \frac{\partial u_3 v_3}{\partial y} + \frac{\partial u_3 w_3}{\partial z} - f v_3 = -\frac{1}{\rho_0}\frac{\partial p_3}{\partial x} + \frac{\partial}{\partial x}(K_{HM3}\frac{\partial u_3}{\partial x}) + \frac{\partial}{\partial y}(K_{HM3}\frac{\partial u_3}{\partial y}) + \frac{\partial}{\partial z}(K_{M3}\frac{\partial u_3}{\partial z}), \tag{7.1a}$$

$$\frac{\partial s_3}{\partial t} + \frac{\partial}{\partial x}(u_3 s_3 - K_{HS3}\frac{\partial s_3}{\partial x}) + \frac{\partial}{\partial y}(v_3 s_3 - K_{HS3}\frac{\partial s_3}{\partial y}) + \frac{\partial}{\partial z}(w_3 s_3 - K_{S3}\frac{\partial s_3}{\partial z}) = 0, \tag{7.1b}$$

$$\frac{\partial u_3}{\partial x} + \frac{\partial v_3}{\partial y} + \frac{\partial w_3}{\partial z} = 0, \tag{7.1c}$$

$$\frac{\partial p_3}{\partial z} = -\rho_3 g, \tag{7.1d}$$

$$\rho_3 = \rho_0(1 + \beta s_3). \tag{7.1e}$$

In these equations u_3, v_3 and w_3 are the x-, y- and z-components of the 3-dimensional flow velocity, f is the Coriolis parameter, p_3 is the pressure, ρ_0 the reference density, K_{HM3} and K_{M3} the horizontal and vertical eddy viscosity's, ρ_3 the density, s_3 the salinity, K_{HS3} and K_{S3} the horizontal and vertical diffusion coefficients and β a constant describing the dependence of density on salinity. The subscript 3 indicates that the variable corresponds to the 3-dimensional formulation (in contrast to the width averaged formulation). Now, the equations are integrated over width, yielding

$$\begin{aligned}\int_{-B/2}^{B/2}\frac{\partial u_3}{\partial t}dy+\int_{-B/2}^{B/2}\frac{\partial u_3u_3}{\partial x}dy+\int_{-B/2}^{B/2}\frac{\partial u_3v_3}{\partial y}dy+\int_{-B/2}^{B/2}\frac{\partial u_3w_3}{\partial z}dy\\ -\int_{-B/2}^{B/2}fv_3dy=-\frac{1}{\rho_0}\int_{-B/2}^{B/2}\frac{\partial p_3}{\partial x}dy+\int_{-B/2}^{B/2}\frac{\partial}{\partial x}(K_{HM3}\frac{\partial u_3}{\partial x})dy\\ +\int_{-B/2}^{B/2}\frac{\partial}{\partial y}(K_{HM3}\frac{\partial u_3}{\partial y})dy+\int_{-B/2}^{B/2}\frac{\partial}{\partial z}(K_{M3}\frac{\partial u_3}{\partial z})dy,\end{aligned} \tag{7.2a}$$

$$\begin{aligned}\int_{-B/2}^{B/2}\frac{\partial s_3}{\partial t}dy+\int_{-B/2}^{B/2}\frac{\partial}{\partial x}(u_3s_3-K_{HS3}\frac{\partial s_3}{\partial x})dy\\ +\int_{-B/2}^{B/2}\frac{\partial}{\partial y}(v_3s_3-K_{HS3}\frac{\partial s_3}{\partial y})dy+\int_{-B/2}^{B/2}\frac{\partial}{\partial z}(w_3s_3-K_{S3}\frac{\partial s_3}{\partial z})dy=0,\end{aligned} \tag{7.2b}$$

$$\int_{-B/2}^{B/2}\frac{\partial u_3}{\partial x}dy+\int_{-B/2}^{B/2}\frac{\partial v_3}{\partial y}dy+\int_{-B/2}^{B/2}\frac{\partial w_3}{\partial z}dy=0, \tag{7.2c}$$

$$\int_{-B/2}^{B/2}\frac{\partial p_3}{\partial z}dy=-\int_{-B/2}^{B/2}\rho_3gdy, \tag{7.2d}$$

$$\int_{-B/2}^{B/2}\rho_3dy=\rho_0\int_{-B/2}^{B/2}(1+\beta s_3)dy. \tag{7.2e}$$

It is assumed that the wals are vertical and that $B=B(x)$. The Leibniz integral rule (see *Weisstein*), can be written as $\int_{g(x)}^{h(x)}\frac{\partial}{\partial x}f(x,t)dt=\frac{\partial}{\partial x}\big[\int_{g(x)}^{h(x)}f(x,y)dy\big]-f(x,h(x))\frac{dh(x)}{dx}+f(x,g(x))\frac{dg(x)}{dx}$. Now, this rule is applied to the set of equations and it is assumed that $\frac{\partial p_3}{\partial y}=0$ [3] and consequently $p_3=p$ is independent of y[4].

[3] *Winant* [2007] showed that this assumption can be made as long $\frac{B}{H}<<1$. In the case of this study the maximum value for $\frac{B}{H}\approx 0.55$, but this only holds for a very small part of the estuary. Most of the time it is a lot smaller, less than 0.3.

[4] In this work, the disappearance of the subscript 3 indicates that the variable is width averaged.

The result is

$$\begin{aligned}
&\frac{\partial}{\partial t}\int_{-B/2}^{B/2} u_3 dy + \frac{\partial}{\partial x}\int_{-B/2}^{B/2} u_3 u_3 dy \\
&-\frac{1}{2}\frac{\partial B}{\partial x}\big[(u_3u_3)\big|_{y=B/2} + (u_3u_3)\big|_{y=-B/2}\big] + (u_3v_3)\big|_{y=B/2} - (u_3v_3)\big|_{y=-B/2} \\
&+\frac{\partial}{\partial z}\int_{-B/2}^{B/2} u_3 w_3 dy - \int_{-B/2}^{B/2} f v_3 dy = -\frac{1}{\rho_0}\int_{-B/2}^{B/2}\frac{\partial p}{\partial x}dy \\
&+\frac{\partial}{\partial x}\big[\int_{-B/2}^{B/2}(K_{HM3}\frac{\partial u_3}{\partial x})dy\big] \\
&-\frac{1}{2}\frac{\partial B}{\partial x}\big[(K_{HM3}\frac{\partial u_3}{\partial x})\big|_{y=B/2} + (K_{HM3}\frac{\partial u_3}{\partial x})\big|_{y=-B/2}\big] \\
&+\big[K_{HM3}\frac{\partial u_3}{\partial y}\big]\big|_{y=B/2} - \big[K_{HM3}\frac{\partial u_3}{\partial y}\big]\big|_{y=-B/2} + \frac{\partial}{\partial z}\big[\int_{-B/2}^{B/2}(K_{M3}\frac{\partial u_3}{\partial z})dy\big],
\end{aligned} \tag{7.3a}$$

$$\begin{aligned}
&\frac{\partial}{\partial t}\int_{-B/2}^{B/2} s_3 dy + \frac{\partial}{\partial x}\big[\int_{-B/2}^{B/2}(u_3s_3 - K_{HS3}\frac{\partial s_3}{\partial x})dy\big] \\
&-\frac{1}{2}\frac{\partial B}{\partial x}\big[\big(u_3s_3 - K_{HS3}\frac{\partial s_3}{\partial x}\big)\big|_{y=B/2} + \big(u_3s_3 - K_{HS3}\frac{\partial s_3}{\partial x}\big)\big|_{y=-B/2}\big] \\
&+\big(v_3s_3 - K_{HS3}\frac{\partial s_3}{\partial y}\big)\big|_{y=B/2} - \big(v_3s_3 - K_{HS3}\frac{\partial s_3}{\partial y}\big)\big|_{y=-B/2} \\
&+\frac{\partial}{\partial z}\big[\int_{-B/2}^{B/2}(w_3s_3 - K_{S3}\frac{\partial s_3}{\partial z})dy\big] = 0,
\end{aligned} \tag{7.3b}$$

$$\begin{aligned}
&\frac{\partial}{\partial x}\big[\int_{-B/2}^{B/2} u_3 dy\big] - \frac{1}{2}\frac{\partial B}{\partial x}\big[u_3\big|_{y=B/2} + u_3\big|_{y=-B/2}\big] + v_3\big|_{y=B/2} - v_3\big|_{y=-B/2} \\
&+\frac{\partial}{\partial z}\big[\int_{-B/2}^{B/2} w_3 dy\big] = 0,
\end{aligned} \tag{7.3c}$$

$$B\frac{\partial p}{\partial z} = -\int_{-B/2}^{B/2}\rho_3 g dy, \tag{7.3d}$$

$$\int_{-B/2}^{B/2}\rho_3 dy = \rho_0\int_{-B/2}^{B/2}(1+\beta s_3)dy. \tag{7.3e}$$

Now, the following boundary conditions are used:

$$0 = v_3\big|_{y=\pm B/2} \mp \frac{1}{2}\frac{\partial B}{\partial x}u_3\big|_{y=\pm B/2}, \tag{7.4a}$$

$$\mp\frac{1}{2}\frac{\partial B}{\partial x}\big[K_{HM3}\frac{\partial u_3}{\partial x}\big]\big|_{y=\pm B/2} + \big[K_{HM3}\frac{\partial u_3}{\partial y}\big]\big|_{y=\pm B/2}, \tag{7.4b}$$

$$\mp\frac{1}{2}\frac{\partial B}{\partial x}\big[u_3 s_3 - K_{HS3}\frac{\partial s_3}{\partial x}\big]\big|_{y=\pm B/2} + \big[v_3 s_3 - K_{HS3}\frac{\partial s_3}{\partial y}\big]\big|_{y=\pm B/2} = 0. \tag{7.4c}$$

Physically, the first boundary condition means that the velocity normal to the side walls is zero (this boundary condition can be found in for instance *Gill* [1982]). The second boundary condition is the assumption that the friction component tangent to the wall is zero (free-slip). The third boundary condition states that the normal component of the salt flux is zero at the walls (see *Gill* [1982]). Applying these boundary conditions in Equation 7.3a-7.3e, yields

$$\begin{aligned}\frac{\partial}{\partial t}\int_{-B/2}^{B/2} u_3 dy + \frac{\partial}{\partial x}\int_{-B/2}^{B/2} u_3 u_3 dy + \frac{\partial}{\partial z}\int_{-B/2}^{B/2} u_3 w_3 dy - \int_{-B/2}^{B/2} f v dy \\ = -\frac{1}{\rho_0}\int_{-B/2}^{B/2}\frac{\partial p}{\partial x}dy + \frac{\partial}{\partial x}\big[\int_{-B/2}^{B/2}(K_{HM3}\frac{\partial u_3}{\partial x})\big]dy \\ + \frac{\partial}{\partial z}\big[\int_{-B/2}^{B/2}(K_{M3}\frac{\partial u_3}{\partial z})\big]dy,\end{aligned} \tag{7.5a}$$

$$\begin{aligned}\frac{\partial}{\partial t}\int_{-B/2}^{B/2} s_3 dy + \frac{\partial}{\partial x}\big[\int_{-B/2}^{B/2}(u_3 s_3 - K_{HS3}\frac{\partial s_3}{\partial x})dy\big] \\ + \frac{\partial}{\partial z}\big[\int_{-B/2}^{B/2}(w_3 s_3 - K_{S3}\frac{\partial s_3}{\partial z})dy\big] = 0,\end{aligned} \tag{7.5b}$$

$$\frac{\partial}{\partial x}\big[\int_{-B/2}^{B/2} u_3 dy\big] + \frac{\partial}{\partial z}\big[\int_{-B/2}^{B/2} w_3 dy\big] = 0, \tag{7.5c}$$

$$B\frac{\partial p}{\partial z} = -\int_{-B/2}^{B/2} \rho_3 g dy, \tag{7.5d}$$

$$\int_{-B/2}^{B/2} \rho_3 dy = \rho_0 \int_{-B/2}^{B/2} (1+\beta s_3) dy. \tag{7.5e}$$

Now, the following expansions are introduced: $s_3 = s + \hat{s}$, $\rho_3 = \rho + \hat{\rho}$, $\eta_3 = \eta + \hat{\eta}$, $H_3 = H + \hat{H}$, $u_3 = u + \hat{u}$, $v_3 = v + \hat{v}$ and $w_3 = w + \hat{w}$. Where s, ρ, η, H, u, v and w are width averaged quantities and $\hat{s}$, $\hat{\rho}$, $\hat{\eta}$, $\hat{H}$, $\hat{u}$, $\hat{v}$ and $\hat{w}$ the deviations from those width averaged quantities (the variables with the hat are zero when averaged over width). The approximation is made that the integrals over width of derivatives to x of the variables with a hat are zero as well (as $B = B(x)$ this is already true for derivatives to z and t of quantities with a hat). It can be concluded from *Winant* [2007] that variations of u with y are small in this derivation, because H is assumed to be (almost) independent of y.[5] Similarly, because H varies very little with y and there is no salt flux normal to the side walls of the channel (or other mechanism that can be responsible for the variation of s with y), it is assumed that $\hat{s}$ is very small as well. For these reasons it is assumed that $\frac{\partial \hat{u}}{\partial x}$ and $\frac{\partial \hat{s}}{\partial x}$ are very small and their with average is equal to zero. Substitution of the expansions in the system of three equations results in:

$$\begin{aligned}\frac{\partial Bu}{\partial t} + \frac{\partial}{\partial x}\big[Buu + \int_{-B/2}^{B/2} \hat{u}\hat{u} dy\big] + \frac{\partial}{\partial z}\big[Buw + \int_{-B/2}^{B/2} \hat{u}\hat{w} dy\big] - \int_{-B/2}^{B/2} fv dy \\ = -\frac{B}{\rho_0}\frac{\partial p}{\partial x} + \frac{\partial}{\partial x}\big[BK_{HM3}\frac{\partial u}{\partial x}\big] + \frac{\partial}{\partial z}\big[BK_{M3}\frac{\partial u}{\partial z}\big],\end{aligned} \tag{7.6a}$$

$$\begin{aligned}&\frac{\partial Bs}{\partial t} + \frac{\partial}{\partial x}\big[Bus + \int_{-B/2}^{B/2} \hat{u}\hat{s} dy - BK_{HS3}\frac{\partial s}{\partial x} - \int_{-B/2}^{B/2} K_{HS3}\frac{\partial \hat{s}}{\partial x} dy\big] \\ &\quad + \frac{\partial}{\partial z}\big[Bws + \int_{-B/2}^{B/2} \hat{w}\hat{s} dy - BK_{S3}\frac{\partial s}{\partial z} - \int_{-B/2}^{B/2} K_{S3}\frac{\partial \hat{s}}{\partial z} dy\big] = 0,\end{aligned} \tag{7.6b}$$

$$\frac{\partial Bu}{\partial x} + \frac{\partial Bw}{\partial z} = 0, \tag{7.6c}$$

$$\frac{\partial p}{\partial z} = -\rho g, \tag{7.6d}$$

[5] From *Winant* [2007] it can be concluded that u varies with y via H, as H is assumed to be (almost) independent of y, it can be assumed that $\hat{u}$ is small.

$$\rho = \rho_0(1 + \beta s). \tag{7.6e}$$

These equations can be simplified by assuming that K_{HM3}, K_{M3}, K_{HS3}, K_{S3}, f are independent of y. *Winant* [2007] showed that the effect of rotation on the flow in the x-direction is limited[6] and for this reason fv is neglected. Furthermore, the following parametrisations are used:

$$-\int_{-B/2}^{B/2} \hat{u}\hat{u}dy = BK_{HMR}\frac{\partial u}{\partial x}, \tag{7.7a}$$

$$-\int_{-B/2}^{B/2} \hat{w}\hat{u}dy = BK_{MR}\frac{\partial u}{\partial z}, \tag{7.7b}$$

$$\int_{-B/2}^{B/2} \hat{u}\hat{s}dy = -BK_{HSR}\frac{\partial s}{\partial x}, \tag{7.7c}$$

$$\int_{-B/2}^{B/2} \hat{w}\hat{s}dy = -K_{SR}\frac{\partial s}{\partial z}. \tag{7.7d}$$

Here K_{HMR}, K_{MR} are also eddy viscosity's and K_{HSR} and K_{SR} are also diffusion coefficients. The introduction of these parametrisations is actually analogous to what is done for Reynolds stresses, see for example *Cushman-Roisin and Beckers* [2011]. Effective eddy viscosity's and effective diffusion coefficients are defined as follows: $K_{HM} = K_{HMR} + K_{HM3}$, $K_M = K_{MR} + K_{M3}$, $K_{HS} = K_{HSR} + K_{HS3}$ and $K_S = K_{SR} + K_{S3}$. Their specific parametrizations are given in Section 2.3. Applying these simplifications to Equation 7.6a - 7.6e gives the following set of width averaged basic equations:

$$\begin{aligned}\frac{\partial Bu}{\partial t} + \frac{\partial}{\partial x}(Buu) + \frac{\partial}{\partial z}(Buw) = -\frac{B}{\rho_0}\frac{\partial p}{\partial x} + \frac{\partial}{\partial x}(BK_{HM}\frac{\partial u}{\partial x}) \\ + \frac{\partial}{\partial z}(BK_M\frac{\partial u}{\partial z}),\end{aligned} \tag{7.8a}$$

$$\frac{\partial Bs}{\partial t} + \frac{\partial}{\partial x}(Bus - BK_{HS}\frac{\partial s}{\partial x}) + \frac{\partial}{\partial z}(Bws - BK_S\frac{\partial s}{\partial z}) = 0, \tag{7.8b}$$

[6] *Winant* [2007] considered a long and narrow geometry, with the width smaller than the external Rossby radius of deformation. Using realistic values for the situation of this study, the external Rossby radius is estimated to be $R = \frac{\sqrt{gH}}{f} \approx 10^5$ m (see *Cushman-Roisin and Beckers* [2011] for more information). A maximum value for B in this study is $B \approx 3 \times 10^4$ m $< R$, so the effect of rotation on u can be assumed to be limited.

$$\frac{\partial Bu}{\partial x} + \frac{\partial Bw}{\partial z} = 0, \tag{7.8c}$$

$$\frac{\partial p}{\partial z} = -\rho g, \tag{7.8d}$$

$$\rho = \rho_0(1 + \beta s). \tag{7.8e}$$

7.1.2 Basic set of equations

Now, the model for a single channel configuration[7] will be derived with Equation (7.8b)-(7.8e) as starting points. Note that s, u, w and p are all subtidal and all variables are width-averaged. Later, the formulation will be adapted to model a network of channels. In order to close the system, boundary conditions are needed. These are given by

$$\text{at } z = -H\text{:} \qquad K_{HS}\frac{\partial s}{\partial x}\frac{\partial H}{\partial x} + K_S\frac{\partial s}{\partial z} = 0, \qquad u = 0, \qquad w = 0, \tag{7.9a}$$

$$\text{at } z = \eta\text{:} \qquad -K_{HS}\frac{\partial s}{\partial x}\frac{\partial \eta}{\partial x} + K_S\frac{\partial s}{\partial z} = 0, \qquad K_M\frac{\partial u}{\partial z} - K_{HM}\frac{\partial u}{\partial x}\frac{\partial \eta}{\partial x} = 0,$$
$$w = u\frac{\partial \eta}{\partial x}, \qquad p = p_{atm}, \tag{7.9b}$$

$$\text{at } x = L_{sea},\ z = -H\text{:} \quad s = s_{ocn}, \tag{7.9c}$$

$$\text{at } x = L_{river}\text{:} \qquad B\int_{-H}^{\eta}(us - K_{HS}\frac{\partial s}{\partial x})dz = 0, \qquad B\int_{-H}^{\eta} udz = Q, \tag{7.9d}$$

$$\text{at } x = L_{sea}, L_{river}\text{:} \qquad u = \lim_{K_{HM}\to 0} u. \tag{7.9e}$$

Here, η is the sea surface elevation, p_{atm} is the sea level pressure, s_{ocn} is the salinity of the adjacent ocean, which will be determined from observations, L_{sea} is the x coordinate where the estuary meets the ocean (see Figure 7.1), L_{river} is the x coordinate where the estuary meets the river (see Figure 7.1), H is the channel depth and Q is river discharge. Physically the boundary conditions at the bottom mean (in order they appear) no salt diffusion normal to the bottom (see *Gill* [1982]), no flow at the bottom (combination of no slip condition and no flow normal trough the bottom, these can be found in *Gill* [1982] and *Cushman-Roisin and Beckers* [2011]). At the surface the physical meaning of the boundary

[7]The single channel model in this thesis is comparable to the model of *MacCready* [2004]

conditions is no salt diffusion normal to the surface (*Gill* [1982]), the stress along the surface is zero (free-slip) (*Cushman-Roisin and Beckers* [2011]), no flow normal to the free surface (*Cushman-Roisin and Beckers* [2011]) and the pressure at the surface equals the pressure of the atmosphere (see *Cushman-Roisin and Beckers* [2011]). It is imposed that the salinity at the bottom and at the boundary between ocean and estuary must equal the salinity of the ocean (see Equation (7.9c), this was also done in *MacCready* [2004]). At $x = L_{river}$ (the head of the estuary), there is no salt transport and the total transport of the estuary equals the river discharge (see *Hansen and Rattray* [1965]). The last boundary condition makes sure that there are no diffusive boundary layers. It can be derived from continuity (Equation (7.8c)) that the second part of Equation (7.9d) holds for every x. Integration over depth of the continuity equation and applying Leibniz integral rule (see Section 7.1.1 for this rule) gives

$$\frac{\partial}{\partial x}\big[B\int_{-H}^{\eta} u dz\big] - \frac{\partial \eta}{\partial x} Bu\big|_{z=\eta} - \frac{\partial H}{\partial x} Bu\big|_{z=-H} + Bw\big|_{z=-H}^{z=\eta} = 0. \tag{7.10}$$

Thereafter, boundary conditions Equation (7.9a) and (7.9b) are applied and the result is

$$\frac{\partial}{\partial x}\big[B\int_{-H}^{\eta} u dz\big] = \frac{\partial \eta}{\partial x} Bu\big|_{z=\eta} - \frac{\partial \eta}{\partial x} Bu\big|_{z=\eta} = 0. \tag{7.11}$$

This equation shows that $\int_{-H}^{\eta} Bu dz$ is independent of x. Combining this conclusion with Equation (7.9d) yields

$$B\int_{-H}^{\eta} u dz = Q \qquad \forall x \tag{7.12}$$

Similarly, from the salt balance (Equation (7.8b)), it can be derived that the depth integrated salt transport is constant. First, the salt balance is integrated over depth and Leibniz integral rule (see Section 7.1.1 for the Leibniz rule) is applied:

$$\begin{aligned} &\frac{\partial}{\partial x}\big[B\int_{-H}^{\eta}(us - K_{HS}\frac{\partial s}{\partial x})dz\big] - B\big[us - K_{HS}\frac{\partial s}{\partial x}\big]\big|_{z=\eta}\frac{\partial \eta}{\partial x} \\ &-B\big[us - K_{HS}\frac{\partial s}{\partial x}\big]\big|_{z=-H}\frac{\partial H}{\partial x} + B\big[ws - K_S\frac{\partial s}{\partial z}\big]\big|_{z=-H}^{z=\eta} = 0. \end{aligned} \tag{7.13}$$

Multiple applications of boundary conditions Equation (7.9a) and (7.9b) results in

$$\frac{\partial}{\partial x}\big[B\int_{-H}^{\eta}(us - K_{HS}\frac{\partial s}{\partial x})dz\big] = 0. \tag{7.14}$$

Integration of this equation with respect to x yields

$$B\int_{-H}^{\eta}(us - K_{HS}\frac{\partial s}{\partial x})dz = T. \tag{7.15}$$

Here, T is a constant. Physically this equation means that the horizontal salt transport is equal to a constant. In a single channel model, this constant will equal zero, as there is no horizontal salt transport at the boundary between the river and the estuary (this is also expressed in boundary condition Equation (7.9d)). However, for a network T might not equal zero for the seaward branches after branching point of the estuary channels. For, this reason it is chosen to maintain T into Equation (7.15).

Now, the set of five equations is simplified further and reduced to a set of three equations. To do this, Equation (7.8d) and Equation (7.8e) are combined to: $\frac{\partial p}{\partial z} = -\rho_0(1+\beta s)g$. Integration of this equation over depth, application of Equation (7.9b), and taking the derivative to x, gives

$$\frac{\partial p}{\partial x} \approx \rho_0 g\frac{\partial \eta}{\partial x} + \rho_0\beta g\int_z^{\eta}\frac{\partial s}{\partial x}dz'. \tag{7.16}$$

This equation, together with Equation (7.8e), is substituted into Equation (7.8a). The resulting system of equations is

$$\begin{aligned}\frac{\partial Buu}{\partial x} + \frac{\partial Buw}{\partial z} = -Bg\frac{\partial \eta}{\partial x} - B\beta g\int_z^{\eta}\frac{\partial s}{\partial x}dz' + \frac{\partial}{\partial x}(BK_{HM}\frac{\partial u}{\partial x})\\ +\frac{\partial}{\partial z}(BK_M\frac{\partial u}{\partial z}),\end{aligned} \tag{7.17a}$$

$$\frac{\partial}{\partial x}\big[Bus - BK_{HS}\frac{\partial s}{\partial x}\big] + \frac{\partial}{\partial z}\big[Bws - BK_s\frac{\partial s}{\partial z}\big] = 0, \tag{7.17b}$$

$$\frac{\partial Bu}{\partial x} + \frac{\partial Bw}{\partial z} = 0. \tag{7.17c}$$

7.1.3 Scaling

In order to estimate the relative magnitudes of the different terms in Equation (7.17a) - (7.17c), the following dimensionless variables (indicated with $\tilde{}$) are introduced: $u = U\tilde{u}$, $w = W\tilde{w}$, $z = H_0\tilde{z}$, $x = \mathcal{L}\tilde{x}$, $p = P\tilde{p}$, $s = s_{ocn}\tilde{s}$, $\eta = N\tilde{\eta}$, $B = B_0\tilde{B}$, $H = H_0\tilde{H}$, $K_{HM} = [K_{HM}]\tilde{K_{HM}}$, $K_M = K\tilde{K_M}$, $K_{HS} = [K_{HS}]\tilde{K_{HS}}$

and $K_S = K\tilde{K_S}$. Substitution of these expressions into Equation (7.17a) - (7.17c), yields the following dimensionless equations:

$$\begin{aligned}\frac{U^2}{\mathcal{L}}\frac{\partial \tilde{B}\tilde{u}\tilde{u}}{\partial \tilde{x}} + \frac{UW}{H_0}\frac{\partial \tilde{B}\tilde{u}\tilde{w}}{\partial \tilde{z}} = &-\frac{gN}{\mathcal{L}}\tilde{B}\frac{\partial \tilde{\eta}}{\partial \tilde{x}} - \frac{\beta s_{ocn} g H_0}{\mathcal{L}}\tilde{B}\int_{\tilde{z}}^{\frac{N}{H_0}\tilde{\eta}} \frac{\partial \tilde{s}}{\partial \tilde{x}} d\tilde{z} \\ &+\frac{[K_{HM}]U}{\mathcal{L}^2}\frac{\partial}{\partial \tilde{x}}(\tilde{B}\tilde{K_{HM}}\frac{\partial \tilde{u}}{\partial \tilde{x}}) + \frac{KU}{H_0^2}\frac{\partial}{\partial \tilde{z}}(\tilde{B}\tilde{K_M}\frac{\partial \tilde{u}}{\partial \tilde{z}}),\end{aligned} \tag{7.18a}$$

$$\begin{aligned}&\frac{\partial}{\partial \tilde{x}}\Big[\frac{U s_{ocn}}{\mathcal{L}}\tilde{B}\tilde{u}\tilde{s} - \frac{[K_{HS}]s_{ocn}}{\mathcal{L}^2}\tilde{B}\tilde{K_{HS}}\frac{\partial \tilde{s}}{\partial \tilde{x}}\Big] \\ &+\frac{\partial}{\partial \tilde{z}}\Big[\frac{W s_{ocn}}{H_0}\tilde{B}\tilde{w}\tilde{s} - \frac{K s_{ocn}}{H_0^2}\tilde{B}\tilde{K_S}\frac{\partial \tilde{s}}{\partial \tilde{z}}\Big] = 0,\end{aligned} \tag{7.18b}$$

$$\frac{U}{\mathcal{L}}\frac{\partial \tilde{B}\tilde{u}}{\partial \tilde{x}} + \frac{W}{H_0}\frac{\partial \tilde{B}\tilde{w}}{\partial \tilde{z}} = 0. \tag{7.18c}$$

Also, the boundary conditions (Equation (7.9a)-(7.9e)) are made dimensionless, using the same dimensionless variables as before. The result is

$$\text{at } \tilde{z} = -\tilde{H}: \qquad \frac{[K_{HS}]H_0}{\mathcal{L}^2}\tilde{K_{HS}}\frac{\partial \tilde{s}}{\partial \tilde{x}}\frac{\partial \tilde{H}}{\partial \tilde{x}} + \frac{K}{H_0}\tilde{K_S}\frac{\partial \tilde{s}}{\partial \tilde{z}} = 0, \quad \tilde{u} = 0, \tag{7.19a}$$

$$\begin{aligned}\text{at } \tilde{z} = \frac{N}{H_0}\tilde{\eta}: \qquad &-\frac{[K_{HS}]N}{\mathcal{L}^2}\tilde{K_{HS}}\frac{\partial \tilde{s}}{\partial \tilde{x}}\frac{\partial \tilde{\eta}}{\partial \tilde{x}} + \frac{K}{H_0}\tilde{K_S}\frac{\partial \tilde{s}}{\partial \tilde{z}} = 0, \\ &\frac{KU}{H}\tilde{K_M}\frac{\partial \tilde{u}}{\partial \tilde{z}} - \frac{[K_{HM}]UN}{L^2}\tilde{K_{HM}}\frac{\partial \tilde{u}}{\partial \tilde{x}}\frac{\partial \tilde{\eta}}{\partial \tilde{x}} = 0, \\ &W\tilde{w} = \frac{UN}{\mathcal{L}}\tilde{u}\frac{\partial \tilde{\eta}}{\partial \tilde{x}},\end{aligned} \tag{7.19b}$$

$$\text{at } \tilde{x} = \frac{L_{sea}}{\mathcal{L}},\ \tilde{z} = -\tilde{H}: \qquad \tilde{s} = 1, \tag{7.19c}$$

$$\text{at } \tilde{x} = \frac{L_{river}}{\mathcal{L}}: \qquad \int_{-\tilde{H}}^{\frac{N}{H_0}\tilde{\eta}} (U\tilde{u}\tilde{s} - \frac{[K_{HS}]}{\mathcal{L}}\tilde{K_{HS}}\frac{\partial \tilde{s}}{\partial \tilde{x}})d\tilde{z} = 0, \tag{7.19d}$$

$$\text{at } \tilde{x} = \frac{L_{sea}}{\mathcal{L}}, \frac{L_{river}}{\mathcal{L}}: \qquad \tilde{u} = \lim_{K\tilde{_{HM}}\to 0} \tilde{u}. \tag{7.19e}$$

Now, several assumptions are made about the scales of W, N, $\mathcal{L}$ and U. Firstly, a scale for W is easily found by assuming that the two terms in Equation (7.18c) are of equal order of magnitude. Secondly, it is taken into consideration that the slope in surface elevation is regulated by the average outflow (see *Geyer* [2010]).

The assumption is made that, in this outflow, the river flow is smaller or equal to the flow that is driven by density gradients. Consequently, the surface slope is mainly determined by the density gradients (see *Geyer* [2010]). From balancing the term with the surface slope with the the density gradient (the two pressure gradient terms) in the momentum balance (Equation (7.18a)) and assuming that $N << H_0$, a scale for N is found. Thirdly, in literature (see *MacCready* [2004]), it is suggested that the pressure gradient term and the vertical friction contribute most to the horizontal momentum balance. Mathematically, this means that the second term on the right hand side has the same order of magnitude as the last term on the right hand side of Equation (7.18a)[8]. As a consequence, a scale for $\mathcal{L}$ can be found. Likewise, it is known from literature that the advection terms are much smaller than the pressure gradient term, therefore the first term on the left hand side in Equation (7.18a) is a lot smaller than the first term on the right hand side. These assumptions lead to the estimates

$$W = \frac{UH_0}{\mathcal{L}}, \tag{7.20a}$$

$$N = \beta s_{ocn} H_0, \tag{7.20b}$$

$$\mathcal{L} = \frac{\beta s_{ocn} g H_0^3}{KU}, \tag{7.20c}$$

$$U^2 << gN. \tag{7.20d}$$

Using Equations (7.20d) and (7.20b), it is found that $\frac{U^2}{gH_0} << \beta s_{ocn}$ (note that $\beta s_{ocn} << 1$[9]). Because of this inequality, the order of magnitude of U is estimated to be

$$U = \beta s_{ocn} \sqrt{gH_0}. \tag{7.21}$$

Next, Equations (7.18a)-(7.18c) are rewritten, using the scales from Equation (7.20a)-(7.20c) and (7.21). Also, Equation (7.18a) is divided by $\frac{KU}{H_0^2}$, Equation (7.18b) by $\frac{Ks_{ocn}}{H_0^2}$ and Equation (7.18c) by $\frac{U}{\mathcal{L}}$. As a result, the following scaled

[8]Note that the first and the second term on the right hand side of Equation (7.18a) have the same order of magnitude.

[9]Filling out realistic values $\beta = 7.7 \times 10^{-4}$ psu^{-1} and $s_{ocn} = 35$ psu, gives $\epsilon = \beta s_{ocn} \approx 2.7 \times 10^{-2} << 1$.

equations are found:

$$\begin{aligned}\epsilon\frac{\partial\tilde{B}\tilde{u}\tilde{u}}{\partial\tilde{x}}+\epsilon\frac{\partial\tilde{B}\tilde{u}\tilde{w}}{\partial\tilde{z}}&=-\tilde{B}\frac{\partial\tilde{\eta}}{\partial\tilde{x}}-\tilde{B}\int_{\tilde{z}}^{\epsilon\tilde{\eta}}\frac{\partial\tilde{s}}{\partial x}d\tilde{z}\\&+\epsilon_H\frac{\partial}{\partial\tilde{x}}(\tilde{B}\tilde{K_{HM}}\frac{\partial\tilde{u}}{\partial\tilde{x}})+\frac{\partial}{\partial\tilde{z}}(\tilde{B}\tilde{K_M}\frac{\partial\tilde{u}}{\partial\tilde{z}}),\end{aligned}\tag{7.22a}$$

$$\frac{\partial}{\partial\tilde{x}}\big[\epsilon\tilde{B}\tilde{u}\tilde{s}-\epsilon_{HS}\tilde{B}\tilde{K_{HS}}\frac{\partial\tilde{s}}{\partial\tilde{x}}\big]+\frac{\partial}{\partial\tilde{z}}\big[\epsilon\tilde{B}\tilde{w}\tilde{s}-\tilde{B}\tilde{K_s}\frac{\partial\tilde{s}}{\partial\tilde{z}}\big]=0,\tag{7.22b}$$

$$\frac{\partial\tilde{B}\tilde{u}}{\partial\tilde{x}}+\frac{\partial\tilde{B}\tilde{w}}{\partial\tilde{z}}=0.\tag{7.22c}$$

The corresponding scaled boundary conditions are

at $\tilde{z}=-\tilde{H}$:

$$\begin{aligned}&\epsilon_{HS}\tilde{K_{HS}}\frac{\partial\tilde{s}}{\partial\tilde{x}}\frac{\partial\tilde{H}}{\partial\tilde{x}}+\tilde{K_S}\frac{\partial\tilde{s}}{\partial\tilde{z}}=0,\qquad\tilde{u}=0,\\&\tilde{w}=0,\end{aligned}\tag{7.23a}$$

at $\tilde{z}=\epsilon\tilde{\eta}$:

$$\begin{aligned}&-\epsilon\epsilon_{HS}\tilde{K_{HS}}\frac{\partial\tilde{s}}{\partial\tilde{x}}\frac{\partial\tilde{\eta}}{\partial\tilde{x}}+\tilde{K_S}\frac{\partial\tilde{s}}{\partial\tilde{z}}=0,\\&\tilde{K_M}\frac{\partial\tilde{u}}{\partial\tilde{z}}-\epsilon\epsilon_H\tilde{K_{HM}}\frac{\partial\tilde{u}}{\partial\tilde{x}}\frac{\partial\tilde{\eta}}{\partial\tilde{x}}=0,\\&\tilde{w}=\epsilon\tilde{u}\frac{\partial\tilde{\eta}}{\partial\tilde{x}},\end{aligned}\tag{7.23b}$$

at $\tilde{x}=\dfrac{L_{sea}}{\mathcal{L}}$, $\tilde{z}=-\tilde{H}$:

$$\tilde{s}=1,\tag{7.23c}$$

at $\tilde{x}=\dfrac{L_{river}}{\mathcal{L}}$:

$$\int_{-\tilde{H}}^{\epsilon\tilde{\eta}}(\epsilon\tilde{u}\tilde{s}-\epsilon_{HS}\tilde{K_{HS}}\frac{\partial\tilde{s}}{\partial\tilde{x}})d\tilde{z}=0,\tag{7.23d}$$

at $\tilde{x}=\dfrac{L_{sea}}{\mathcal{L}},\dfrac{L_{river}}{\mathcal{L}}$:

$$\tilde{u}=\lim_{\tilde{K_{HM}}\to 0}\tilde{u}.\tag{7.23e}$$

The scaled depth integrated mass balance and salt balance (scaled versions of Equation (7.12) and (7.15)) read

$$\tilde{B}\int_{-\tilde{H}}^{\epsilon\tilde{\eta}}\tilde{u}d\tilde{z}=\epsilon_Q\qquad\forall\tilde{x},\tag{7.24}$$

$$\tilde{B}\int_{-\tilde{H}}^{\epsilon\tilde{\eta}}(\epsilon\tilde{u}\tilde{s}-\epsilon_{HS}\tilde{K_{HS}}\frac{\partial\tilde{s}}{\partial\tilde{x}})d\tilde{z}=T_n.\tag{7.25}$$

Equation (7.22a)-(7.22c), (7.24), (7.25) and (7.23a)-(7.23e) contain the following dimensionless variables:

$$\epsilon = \beta s_{ocn} \quad , \tag{7.26a}$$

$$\epsilon_H = \frac{[K_{HM}]H_0^2}{K\mathcal{L}^2}, \tag{7.26b}$$

$$\epsilon_Q = \frac{Q}{B_0 H_0 U}, \tag{7.26c}$$

$$\epsilon_{HS} = \frac{[K_{HS}]H_0^2}{K\mathcal{L}^2}, \tag{7.26d}$$

$$T_n = \frac{TH_0}{B_0 K s_{ocn} \mathcal{L}}. \tag{7.26e}$$

Clearly, by filling out numbers, ϵ is a small parameter, $\epsilon << 1$. Likewise, and by assuming that $[K_{HM}] \approx [K_{HS}]$, it follows that $\epsilon_H = \mathcal{O}(\epsilon)$.[10] The order of magnitude of ϵ_{HS} and ϵ_Q can vary within a certain range, this range will be estimated later using physical reasoning. For now, it is only is estimated from Equation (7.25) that ϵ_{HS} should be $\mathcal{O}(\epsilon)$ or smaller. If $\epsilon_{HS} = \mathcal{O}(1)$, then, according to Equation (7.25), the horizontal diffusion is dominant in the depth averaged salt balance.[11] The horizontal diffusion provides import of salt from to ocean to the estuary and the estuary will become fully salty, which is not an interesting situation for this thesis.[12] The order of magnitude of T_n is unknown yet. The dimensional version of this constant will be calculated in the model.

7.1.4 Leading-order and next-to-leading order equations

Subsequently, the following expansions are introduced:

$$\tilde{s} = \tilde{s_0} + \epsilon\tilde{s_1} + \epsilon^2\tilde{s_2} + \mathcal{O}(\epsilon^3), \tag{7.27a}$$

$$\tilde{u} = \tilde{u_0} + \epsilon\tilde{u_1} + \epsilon^2\tilde{u_2} + \mathcal{O}(\epsilon^3), \tag{7.27b}$$

$$\tilde{w} = \tilde{w_0} + \epsilon\tilde{w_1} + \epsilon^2\tilde{w_2} + \mathcal{O}(\epsilon^3), \tag{7.27c}$$

$$\tilde{\eta} = \tilde{\eta_0} + \epsilon\tilde{\eta_1} + \epsilon^2\tilde{\eta_2} + \mathcal{O}(\epsilon^3). \tag{7.27d}$$

[10] An example of an estimation is that $\epsilon_H \approx 10^{-3}$.

[11] Note that $\epsilon_Q \leq \mathcal{O}(1)$ (at least for cases in this study). This can be concluded from filling out typical numbers in Equation (7.26c).

[12] Alternatively, for $\tilde{K_{HS}}$ independent of z and one channel (then $T_n = 0$), the x-derivative of the largest component of the depth averaged salinity is zero in this situation (as the horizontal diffusion term is the only dominant term in Equation (7.25) in that case). As there is a high salinity at the estuary mouth, where the estuary meets the sea, the whole estuary will get very salty in that situation.

After substitution of these expansions into Equations (7.22a)-(7.22c) an $\mathcal{O}(1)$ set of dimensionless equations is found:

$$0 = -\frac{\partial \eta_0}{\partial x} + \frac{\partial s_0}{\partial x} z + \frac{\partial}{\partial z}(K_M \frac{\partial u_0}{\partial z}), \tag{7.28a}$$

$$\frac{\partial}{\partial z}(K_s \frac{\partial s_0}{\partial z}) = 0, \tag{7.28b}$$

$$\frac{\partial B u_0}{\partial x} + \frac{\partial B w_0}{\partial z} = 0. \tag{7.28c}$$

Note that the variables are dimensionless and the ˜sign is omitted in the equations, this will also be done in the subsequent equations (unless stated else, the following equations are dimensionless).
The $\mathcal{O}(1)$ boundary conditions are

at $z = -H$: $$K_S \frac{\partial s_0}{\partial z} = 0, \quad u_0 = 0, \quad w_0 = 0, \tag{7.29a}$$

at $z = 0$: $$K_S \frac{\partial s_0}{\partial z} = 0, \quad \frac{\partial u_0}{\partial z} = 0, \quad w_0 = 0, \tag{7.29b}$$

at $x = \frac{L_{sea}}{\mathcal{L}}$, $z = -H$: $$s_0 = 1, \tag{7.29c}$$

at $x = \frac{L_{sea}}{\mathcal{L}}$ and at $x = \frac{L_{river}}{\mathcal{L}}$: $$u_0 = \lim_{K_{HM} \to 0} u_0. \tag{7.29d}$$

The $\mathcal{O}(1)$ depth averaged mass balance ($\mathcal{O}(1)$ version of Equation (7.24)) is

$$B \int_{-H}^{0} u_0 dz = \delta_{n,0} \epsilon_Q \qquad \forall x, \tag{7.30}$$

In this equation the order of magnitude of ϵ_Q is not known yet, but it is assumed that $\epsilon_Q = \mathcal{O}(\epsilon^n)$. For this reason, $\delta_{n,0}$ is introduced into the equation, $\delta_{n,0} = 1$ if $n = 0$ and $\delta_{n,0} = 0$ else. There is no $\mathcal{O}(1)$ depth averaged salt balance equation. Note that, to arrive at Equation (7.28a), a consequence of Equation (7.28b) is used. From combining Equation (7.28b) with Equation (7.29a), it can be concluded that $s_0 = s_0(x)$ is independent of depth[13] and consequently $\int_z^0 s_0 dz' = -s_0 z$. This last result is used for deriving Equation (7.28a).

[13]This does not necessarily mean that s_0 equals the depth-averaged salinity. In fact it will be found later that s_1 also contains a part of the depth-averaged salinity.

Similarly, by substitution of the expansions into Equations (7.22a)-(7.22c), an $\mathcal{O}(\epsilon)$ set equations of equations is found:

$$\begin{aligned}\frac{\partial Bu_0u_0}{\partial x}+\frac{\partial Bu_0w_0}{\partial z}=&-B\frac{\partial \eta_1}{\partial x}-B\int_z^0\frac{\partial s_1}{\partial x}dz'-Bs_0\eta_0\\&+\frac{\epsilon_H}{\epsilon}\frac{\partial}{\partial x}(BK_{HM}\frac{\partial u_0}{\partial x})+\frac{\partial}{\partial z}(BK_M\frac{\partial u_1}{\partial z}),\end{aligned}\tag{7.31a}$$

$$\frac{\partial}{\partial x}\big[Bu_0s_0-\frac{\epsilon_{HS}}{\epsilon}BK_{HS}\frac{\partial s_0}{\partial x}\big]+\frac{\partial}{\partial z}\big[Bw_0s_0-BK_s\frac{\partial s_1}{\partial z}\big]=0,\tag{7.31b}$$

$$\frac{\partial Bu_1}{\partial x}+\frac{\partial Bw_1}{\partial z}=0.\tag{7.31c}$$

The corresponding boundary conditions are

at $z=-H$:
$$\frac{\epsilon_{HS}}{\epsilon}K_{HS}\frac{\partial s_0}{\partial x}\frac{\partial H}{\partial x}+K_s\frac{\partial s_1}{\partial z}=0,\qquad u_0=0,$$
$$w_0=0,\tag{7.32a}$$

at $z=0$:
$$K_S\frac{\partial s_1}{\partial z}=0,\qquad \frac{\partial u_1}{\partial z}=0,$$
$$w_1=\epsilon\frac{\partial \eta_0}{\partial x},\tag{7.32b}$$

at $x=\dfrac{L_{sea}}{\mathcal{L}}$, $z=-H$:
$$s_1=0,\tag{7.32c}$$

at $x=\dfrac{L_{river}}{\mathcal{L}}$:
$$\int_{-H}^0(u_0s_0-\frac{\epsilon_{HS}}{\epsilon}K_{HS}\frac{\partial s_0}{\partial x})dz=0,\tag{7.32d}$$

at $x=\dfrac{L_{sea}}{\mathcal{L}}$ and $\dfrac{L_{river}}{\mathcal{L}}$:
$$u_1=\lim_{K_{HM}\to 0}u_1.\tag{7.32e}$$

The $\mathcal{O}(\epsilon)$ depth integrated mass balance and salt transport equation ($\mathcal{O}(\epsilon)$ version of Equation (7.24) and (7.25)) are

$$B\int_{-H}^0u_1dz+Bu_0\big|_{z=0}\eta_0=\delta_{n,1}\frac{\epsilon_Q}{\epsilon}\qquad\forall x,\tag{7.33}$$

$$s_0\delta_{n,0}\epsilon_Q-\frac{\epsilon_{HS}}{\epsilon}BHK_{HS}\frac{\partial s_0}{\partial x}=T_n.\tag{7.34}$$

Here, $\delta_{n,1} = 1$ if $n = 1$ ($\epsilon_Q = \mathcal{O}(\epsilon)$) and else, $\delta_{n,0} = 0$. Note that Equation (7.30) (and a Taylor expansion) is used for deriving Equation (7.33). Equation (7.30) (the $\mathcal{O}(1)$ integrated mass balance) and $s_0 = s_0(x)$ are used for deriving Equation (7.34). It is possible that some terms containing ϵ_Q or ϵ_{HS} in the previous $\mathcal{O}(\epsilon)$ equations disappear. The reason is that the exact order of magnitudes of ϵ_Q and ϵ_{HS} are unknown yet. Consequently, when the order of magnitudes of ϵ_Q and ϵ_{HS} are known, the terms containing ϵ_Q and ϵ_{HS}, might appear to be smaller than the other terms in the equation they are in.

7.1.5 Order of magnitude of ϵ_Q and ϵ_{HS}

Now, to estimate the order of magnitudes of ϵ_Q and ϵ_{HS}, the depth integrated continuity equation (Equation (7.24)) and the salt transport equation (Equation (7.25)) are expanded. All terms that are $\mathcal{O}(\epsilon)$ or larger for the continuity equation and $\mathcal{O}(\epsilon^2)$ or larger for the salt transport equation are maintained. This gives

$$B\int_{-H}^{0} u_0 dz + \epsilon\int_{-H}^{0} u_1 dz + \epsilon B u_0\big|_{z=0}\eta_0 = \epsilon_Q \qquad \forall x, \tag{7.35}$$

$$\begin{aligned} B\int_{-H}^{0}(\epsilon u_0 s_0 + \epsilon^2 u_1 s_0 + \epsilon^2 u_0 s_1 - \epsilon_{HS}K_{HS}\frac{\partial s_0}{\partial x} - \epsilon_{HS}\epsilon K_{HS}\frac{\partial s_1}{\partial x})dz \\ +\epsilon^2 B s_0 u_0\big|_{z=0}\eta_0 - \epsilon_{HS}\epsilon B K_{HS}\frac{\partial s_0}{\partial x}\eta_0 = T_n. \end{aligned} \tag{7.36}$$

Note that for deriving this equation, a Taylor expansion is made of the integral in Equation (7.25) and it is used that $s_0 = s_0(x)$. Equation (7.36) can be simplified further by substitution of Equation (7.35), this gives

$$\begin{aligned} \epsilon\epsilon_Q s_0 + \epsilon^2 B\int_{-H}^{0} u_0 s_1 dz - \epsilon_{HS}K_{HS}H\frac{\partial s_0}{\partial x} - \epsilon_{HS}\epsilon K_{HS}\int_{-H}^{0}\frac{\partial s_1}{\partial x}dz \\ -\epsilon_{HS}\epsilon B K_{HS}\frac{\partial s_0}{\partial x}\eta_0 = T_n. \end{aligned} \tag{7.37}$$

Again, terms containing ϵ_Q and ϵ_{HS} might disappear later.

Physically the first term in the salt transport equation (Equation (7.37)) is salt transport due to river discharge. So, the transport due to river discharge is $\mathcal{O}(\epsilon\epsilon_Q)$. The second term in Equation (7.37) represents the exchange flow, this term is always $\mathcal{O}(\epsilon^2)$. The third, the fourth and the fifth terms in Equation (7.37) are due to diffusion of salt. The fourth and the fifth term (which are of order $\mathcal{O}(\epsilon_{HS}\epsilon)$) are

smaller than the third term (which is of order $\mathcal{O}(\epsilon)$) and are neglected. The result is

$$\epsilon\epsilon_Q s_0 + \epsilon^2 B \int_{-H}^{0} u_0 s_1 dz - \epsilon_{HS} K_{HS} H \frac{\partial s_0}{\partial x} = T_n. \tag{7.38}$$

Now, depending on the order of magnitudes of ϵ_Q and ϵ_{HS} there are several possible balances. This is illustrated in Figure 7.2. In this figure it is shown (in white) which process(es) dominate (river flow, horizontal diffusion and/or exchange flow). River flow results in export of salt from the estuary and both horizontal diffusion and exchange flow lead to import of salt into the estuary. Consequently, if river flow is dominant, most of the salt will be exported away and the resulting estuary will consist of fresh water. This range of ϵ_Q and ϵ_{HS} where this is the case is colored red in the figure. If horizontal diffusion and/or exchange flow dominate(s), no term can balance the import of salt and the estuary will get fully salty (green area in the figure). If river flow and one or two of the other processes dominate, there can be balance between import and export of salt (blue area in the figure). For this study only the last case is of interest and only the ranges for ϵ_Q and ϵ_{HS} that are colored blue are considered. So if only terms of $\mathcal{O}(\epsilon^2)$ or bigger are considered, the combinations that are considered are $\epsilon_Q = \mathcal{O}(1)$ while $\epsilon_{HS} = \mathcal{O}(\epsilon)$ and $\epsilon_Q = \mathcal{O}(\epsilon)$ with $\epsilon_{HS} = \mathcal{O}(\epsilon^2)$.

7.1.6 Solving the equations

Next, an equation for s_1 can be found by substitution of the $\mathcal{O}(\epsilon)$ salt transport equation (Equation (7.34)) and the $\mathcal{O}(1)$ mass balance (Equation (7.28c)) in the $\mathcal{O}(\epsilon)$ salt balance (Equation (7.31b)), leading to

$$B(u_0 - \delta_{n,0}\frac{\epsilon_Q}{BH})\frac{\partial s_0}{\partial x} + (\frac{T_n}{\epsilon} - s_0\delta_{n,0}\epsilon_Q)\frac{\partial}{\partial x}\big[\frac{1}{H}\big] - \frac{\partial}{\partial z}\big[BK_s\frac{\partial s_1}{\partial z}\big] = 0. \tag{7.39}$$

From results of the network model T_n always appears to be very small, so T_n is estimated to be of $\mathcal{O}(\epsilon^2)$. Furthermore, $\frac{\partial}{\partial x}\big[\frac{1}{H}\big] = -\frac{1}{H^2}\frac{\partial H}{\partial x} = -DH$, with $DH = \frac{1}{H}\frac{\partial H^2}{\partial x}$. The dimensionless parameter DH is found to be small (about 0.025 maximum) and therefore it is estimated to be $\mathcal{O}(\epsilon)$. Neglecting all the terms of $\mathcal{O}(\epsilon)$ or smaller, Equation (7.39) can be further simplified to

$$K_s\frac{\partial^2 s_1}{\partial z^2} = (u_0 - \delta_{n,0}\frac{\epsilon_Q}{BH})\frac{\partial s_0}{\partial x}. \tag{7.40}$$

Note that $B = B(x)$ is independent of z. Later, this equation can be used to find an expression for s_1 in terms of $\frac{\partial s_0}{\partial x}$. But first, an Equation for u_0 is derived,

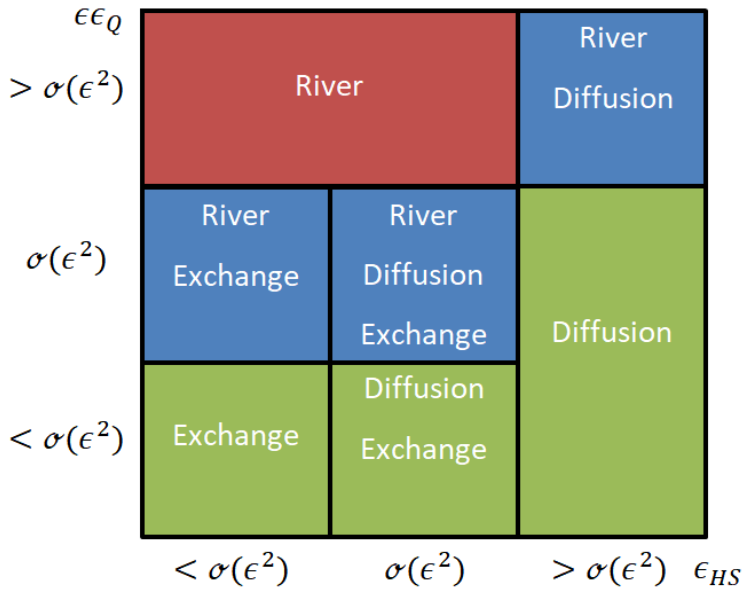

Figure 7.2: Diagram illustrating the physical meaning of different order of magnitudes of ϵ_Q and ϵ_{HS}. The dominant processes (river flow, horizontal diffusion and/or exchange flow) are given in white. For the ranges of ϵ_Q and and ϵ_{HS} that are colored red in the figure, there will be a fresh water estuary, similarly a green color indicates a fully salty estuary and blue indicates that there is a balance between import of salt and export of salt. Only the situations corresponding with the blue area's are considered in this study.

using the $\mathcal{O}(1)$ momentum balance (Equation (7.28a)) as starting point. Taking the z-derivative of Equation (7.28a), gives:

$$\frac{\partial^3 u_0}{\partial z^3} = -\frac{1}{K_M}\frac{\partial s_0}{\partial x}. \tag{7.41}$$

Thereafter an equation for u_0 is found by integrating Equation (7.41) several times over z, applying the boundary conditions Equation (7.29a) and (7.29b) and using Equation (7.30) (the $\mathcal{O}(1)$ depth integrated mass balance), the result is:

$$u_0 = u_E f_1 + \delta_{n,0} u_Q f_2. \tag{7.42}$$

With,

$$u_E = \frac{H^3}{48K_M}\frac{\partial s_0}{\partial x}, \tag{7.43a}$$

$$u_Q = \frac{\epsilon_Q}{BH}, \tag{7.43b}$$

$$f_1 = 1 - 9\zeta^2 - 8\zeta^3, \tag{7.43c}$$

$$f_2 = \frac{3}{2} - \frac{3}{2}\zeta^2. \tag{7.43d}$$

Physically, u_E gives the strength of the exchange flow (see *MacCready* [2004]) and u_Q is the velocity due to river flow. In these Equations ζ is given by

$$\zeta \equiv \frac{z}{H}. \tag{7.44}$$

In order to find an expression for s_1, Equation (7.42) is substituted into Equation (7.40) and the resulting equation is integrated multiple times with respect to z. Equation (7.32b) and (7.32c) are used as boundary conditions. The result is:

$$s_1 = \frac{H^2}{K_S}\frac{\partial s_0}{\partial x}(u_E f_3 + \delta_{n,0} u_Q f_4). \tag{7.45}$$

Here,

$$f_3 = -\frac{3}{20} + \frac{1}{2}\zeta^2 - \frac{3}{4}\zeta^4 - \frac{2}{5}\zeta^5, \tag{7.46a}$$

$$f_4 = -\frac{1}{8} + \frac{1}{4}\zeta^2 - \frac{1}{8}\zeta^4. \tag{7.46b}$$

Until now, solutions for s_1 and u_0 are obtained, but a solution for s_0 is needed as well. This can be found using the salt transport equation (Equation (7.38)). This equation can be simplified further, now that it is assumed that $K_{HS} = K_{HS}(x)$, leading to

$$\epsilon\epsilon_Q s_0 + \epsilon^2 B \int_{-H}^{0} u_0 s_1 dz - \epsilon_{HS} B H K_{HS} \frac{\partial s_0}{\partial x} = T_n. \tag{7.47}$$

It depends on the order of magnitude of ϵ_Q and ϵ_{HS} which terms remain in the equation. In the case that $\epsilon_Q = \mathcal{O}(1)$ and $\epsilon_{HS} = \mathcal{O}(\epsilon)$, only the first and the third terms (and T_n) in the equation are relevant. If $\epsilon_Q = \mathcal{O}(\epsilon)$ and $\epsilon_{HS} = \mathcal{O}(\epsilon^2)$, all the terms remain in the equation. It is chosen to keep all terms. There is a chance that you leave a relatively small term into the equation, but at least all dominant terms are taken into account then. For the same reason it is decided to take $\delta_{n,0} = 1$ in Equation (7.30), (7.40), (7.42) and (7.45), resulting in the following equations for u_0 and s_1:

$$u_0 = u_E f_1 + u_Q f_2, \tag{7.48}$$

$$s_1 = \frac{H^2}{K_S}\frac{\partial s_0}{\partial x}(u_E f_3 + u_Q f_4). \tag{7.49}$$

In order to be able to solve Equation (7.47), the integral term should be evaluated. This is done by substitution of Equation (7.48) and (7.49) in this term and then calculating the integral. The contribution of the depth averaged part[14] of s_1, $\overline{s_1} = \frac{1}{H}\int_{-H}^{0} s_1 dz = \frac{H^2}{K_S}\frac{\partial s_0}{\partial x}(-\frac{1}{15}u_E - \frac{1}{15}u_Q)$, gives the following contribution to that integral: $\epsilon^2 B\int_{-H}^{0} u_0\overline{s_1}dz = \epsilon^2\overline{s_1}\delta_{n,0}\epsilon_Q$. This term is of $\mathcal{O}(\epsilon)$ compared to the first term in Equation (7.47) (the term due to river discharge) and is neglected for that reason. Evaluation of the resulting integral gives:

$$\begin{aligned}
\int_{-H}^{0} u_0(s_1 - \overline{s_1})dz &= \int_{-H}^{0} \frac{H^2}{K_S}\frac{\partial s_0}{\partial x}(u_E f_1 + u_Q f_2)(u_E f_3 + u_Q f_4)dz \\
= \frac{H^2}{K_S}\frac{\partial s_0}{\partial x}\big[u_E^2\int_{-H}^{0} f_1 f_3 dz + u_E u_Q\int_{-H}^{0}(f_1 f_4 + f_2 f_3)dz + u_Q^2\int_{-H}^{0} f_2 f_4\big]dz \\
&\approx \frac{H^3}{K_S}\frac{\partial s_0}{\partial x}\big[-0.030u_E^2 - 0.045u_E u_Q - 0.019u_Q^2\big] \\
= -\frac{0.030}{48^2}\frac{H^9}{K_S K_M^2}(\frac{\partial s_0}{\partial x})^3 - \frac{0.045}{48}\frac{H^6 u_Q}{K_S K_M}(\frac{\partial s_0}{\partial x})^2 - 0.019\frac{H^3 u_Q^2}{K_S}\frac{\partial s_0}{\partial x}.
\end{aligned} \tag{7.50}$$

The definition of u_E is used in the last step. Substitution of this result in Equation (7.47) yields

$$\begin{aligned}
\epsilon\epsilon_Q s_0 - \frac{0.030}{48^2}\epsilon^2\frac{BH^9}{K_S K_M^2}(\frac{\partial s_0}{\partial x})^3 - \frac{0.045}{48}\epsilon^2\frac{BH^6 u_Q}{K_S K_M}(\frac{\partial s_0}{\partial x})^2 \\
-0.019\epsilon^2\frac{BH^3 u_Q^2}{K_S}\frac{\partial s_0}{\partial x} - \epsilon_{HS}BHK_{HS}\frac{\partial s_0}{\partial x} = T_n.
\end{aligned} \tag{7.51}$$

This equation can be solved for s_0.

7.1.7 Dimensional equations

For convenience, scales are placed back into the model equations. From now on, variables with ˜are dimensionless and the variables without ˜are dimensional. The

[14]Here the integral is evaluated at $z = 0$ in stead of $z = \eta$. The reason is that, as before, (using a Taylor expansion) it can be shown that the extra contribution due to evaluation at $z = \eta$ is $\mathcal{O}(\epsilon)$ relative to the rest of the integral.

dimensional s_0, s_1 and u_0 are defined in a slightly different way, than the dimensionless equivalents, namely

$$u = u_0, \tag{7.52}$$

$$s = s_0 + s_1. \tag{7.53}$$

Using these definitions and the relation $s = s_{ocn}\tilde{s_0} + \epsilon s_{ocn}\tilde{s_1}$ (and, of course, the scales that where defined in Section 7.1.3), Equation (7.48), (7.49) and (7.51) are made dimensional. The result is

$$u_0 = u_E f_1 + u_Q f_2, \tag{7.54}$$

$$s_1 = \frac{H^2}{K_S}\frac{\partial s_0}{\partial x}(u_E f_3 + u_Q f_4), \tag{7.55}$$

$$\gamma_3(\frac{\partial s_0}{\partial x})^3 + \gamma_2(\frac{\partial s_0}{\partial x})^2 + (\gamma_1 + \gamma_{dif})\frac{\partial s_0}{\partial x} - s_0 = -\frac{T}{Q}. \tag{7.56}$$

The dimensional expressions for u_E and u_Q are $u_E = \frac{\beta g H^3}{48 K_M}\frac{\partial s_0}{\partial x}$ and $u_Q = \frac{Q}{BH}$. The expressions for the polynomials are $f_1 = 1 - 9\zeta^2 - 8\zeta^3$, $f_2 = \frac{3}{2} - \frac{3}{2}\zeta^2$, $f_3 = -\frac{3}{20} + \frac{1}{2}\zeta^2 - \frac{3}{4}\zeta^4 - \frac{2}{5}\zeta^5$ and $f_4 = -\frac{1}{8} + \frac{1}{4}\zeta^2 - \frac{1}{8}\zeta^4$, with $\zeta \equiv \frac{z}{H}$. The expressions for the γ's in Equation (7.56) (these are constant in z, but functions of x) read

$$\gamma_3 = C_3\frac{H^8\beta^2 g^2}{K_S K_M^2 u_Q}, \tag{7.57a}$$

$$\gamma_2 = C_2\frac{H^5\beta g}{K_S K_M}, \tag{7.57b}$$

$$\gamma_1 = C_1\frac{H^2 u_Q}{K_S}, \tag{7.57c}$$

$$\gamma_{dif} = \frac{K_{HS}}{u_Q}. \tag{7.57d}$$

The constants are $C_3 = \frac{0.030}{48^2}$, $C_2 = \frac{0.045}{48}$ and $C_1 = 0.019$.

These equations can be rewritten equations similar to what was found by *MacCready* [2004], except for an extra term containing T. This term is absent in the

model of *MacCready* [2004], because this model is for a single channel configuration and then $T = 0$ psu. In this derivation it is kept in mind that the model will be extended to a network and for the distributaries (smaller channels after a branching point in the main channel, see *Lambert and Group* [2007]) $T \neq 0$ psu. To do this, the following definitions are introduced:

$$s = \overline{s} + s', \tag{7.58}$$

$$u = u_Q + u'. \tag{7.59}$$

In these definitions, $\overline{s}$ and u_Q are averages over depth. Using Equation (7.52) and (7.53), it can be concluded that $u' = u_0 - u_Q$ and $s' = s_1 - \overline{s_1}$ (note that s_0 is independent of z). In this equation $\overline{s_1} = \frac{H^2}{K_S}\frac{\partial s_0}{\partial x}(-\frac{1}{15}u_E - \frac{1}{15}u_Q)$ (see Section 7.1.6 for the calculation of the dimensionless equivalent). Furthermore, it is used that $\overline{\tilde{s}} = \tilde{s_0} + \epsilon\overline{\tilde{s_1}} \approx \tilde{s_0}$, where, again, the bar denotes averaging over depth. The dimensional version of this equation is $\overline{s} \approx s_0$. Using these definitions and results, Equation (7.42)-(7.56) can be rewritten to a similar form as the model by *MacCready* [2004] and the result is

$$u' = u_E F_1 + u_Q F_2, \tag{7.60}$$

$$s' = \frac{H^2}{K_S}\frac{\partial s_0}{\partial x}(u_E F_3 + u_Q F_4), \tag{7.61}$$

$$L_{E3}(\frac{\partial \Sigma}{\partial x})^3 + L_{E2}(\frac{\partial \Sigma}{\partial x})^2 + (L_{E1} + L_D)\frac{\partial \Sigma}{\partial x} - \Sigma = -\frac{T}{Q s_{ocn}}. \tag{7.62}$$

Here, $s = \overline{s} + s'$, with $\overline{s}$ s averaged over depth, $u = u_Q + u'$ and u_E and u_Q defined as before. The functions F_1-F_4 are given by $F_1 = 1 - 9\zeta^2 - 8\zeta^3$, $F_2 = \frac{1}{2} - \frac{3}{2}\zeta^2$, $F_3 = -\frac{1}{12} + \frac{1}{2}\zeta^2 - \frac{3}{4}\zeta^4 - \frac{2}{5}\zeta^5$ and $F_4 = -\frac{7}{12} + \frac{1}{4}\zeta^2 - \frac{1}{8}\zeta^4$. In Equation 7.62, the different length scales and Σ are given by

$$\Sigma = \frac{\overline{s}}{s_{ocn}}, \tag{7.63a}$$

$$L_{E3} = C_3\frac{H^8\beta^2 s_{ocn}^2 g^2}{K_S K_M^2 u_Q}, \tag{7.63b}$$

$$L_{E2} = C_2\frac{H^5\beta s_{ocn} g}{K_S K_M}, \tag{7.63c}$$

$$L_{E1} = C_1 \frac{H^2 u_Q}{K_S}, \tag{7.63d}$$

$$L_D = \frac{K_{HS}}{u_Q}. \tag{7.63e}$$

7.1.8 Calculating the sea surface height at the branching point

As indicated in Section 2.5, in order to determine Q_2 (and thereby Q_3), an expression for the sea surface height at the branching point is needed. The starting point for deriving this expression is the dimensional version of Equation (7.28a) (the $\mathcal{O}(1)$ momentum balance in the x-direction). This dimensional equation is

$$0 = -g\frac{\partial \eta}{\partial x} + \beta g \frac{\partial \overline{s}}{\partial x} z + K_M \frac{\partial^2 u}{\partial z^2}. \tag{7.64}$$

Here, it is used that K_M is independent of z, $u \approx u_0$ and that $\overline{s} \approx s_0$ (with s_0 dimensional). This equation can be rewritten to obtain an expression for u. This expression is integrated several times and the dimensional version of Equation (7.30) ($B\int_{-H}^{0} u dz = Q$) and the dimensional versions of the boundary conditions Equation (7.29a) and (7.29b) (at $z = -H$: $u = 0$ and at $z = 0$: $\frac{\partial u}{\partial z} = 0$ respectively) are applied. The result is

$$\frac{\partial \eta}{\partial x} = -\frac{3K_M Q}{gBH^3} - \frac{3\beta H}{8}\frac{\partial \overline{s}}{\partial x}. \tag{7.65}$$

This equation can be integrated from $x = 0$ to $x = L_{sea}$ and in this way, η at the branching point can be determined. The expression for $\eta\big|_{x=0}$ is

$$\eta\big|_{x=0} = \eta\big|_{x=L_{sea}} + \int_{x=0}^{x=L_{sea}} \frac{3K_M Q}{gBH^3} dx + \int_{x=0}^{x=L_{sea}} \frac{3\beta H}{8}\frac{\partial \overline{s}}{\partial x} dx. \tag{7.66}$$

7.1.9 Expressions for Q_{SP} and Q_{NP} in case of constant depth

In order to estimate the relative change between Q_{SP} and Q_{NP}, it is useful to obtain an approximate expression for their ratio. In order to obtain this expression, first approximate expressions should be obtained for Q_{SP} and Q_{NP} themselves.

As explained in Section 2.5, there are two conditions that determine Q_{SP} (and T_{SP}). These conditions are that at the branching point $\eta_{SP} = \eta_{NP}$ and $\overline{s}_{SP} = \overline{s}_{NP}$,

or in other words η and $\overline{s}$ should be continuous at the branching point. When Q_{SP} is determined, Q_{NP} is easily determined by using $Q_{SC} = Q_{SP} + Q_{NP}$, with Q_{SC} imposed in the model. From test experiments it is expected that Q_{SP} is mainly determined by the condition $\eta_{SP} = \eta_{NP}$. For that reason an exact expression that gives the approximate value of Q_{SP} will be derived from this condition in this section.

In the previous section an expression was found for η at the branching point, namely Equation (7.66). In order to be able to calculate the integrals in this equation, the assumptions are made that (only for finding this approximate expression for Q_{SP}, not in the rest of the model) H is constant and K_M is constant (this can be for example be achieved by assuming that Ri_L =0). After making these approximations, substituting Equation (2.29) (the exponential parametrisation for B) for B and calculation if the integrals in Equation (7.66), the following expression is found for η:

$$\eta\big|_{x=0} = \eta\big|_{x=L_{sea}} - \frac{3K_M Q L_s}{gB_0H^3}(\exp\big[-\frac{(L_{sea}-x_0)}{L_s}\big] - \exp\big[\frac{x_0}{L_s}\big])) + \frac{3\beta H}{8}(\overline{s}\big|_{x=L_{sea}} - \overline{s}\big|_{x=0}). \tag{7.67}$$

A few more approximations are made. One is that $\eta\big|_{x=L_{sea}} = 0$, as in the model $z = 0$ is chosen to be at sea surface height at the boundary between estuary and coast and it is assumed that this sea surface height at the coast is constant and equal for the North Passage and the South Passage. Another is that $\exp\big[-\frac{(L_{sea}-x_0)}{L_s}\big]$ =1. The reason is that L_{sea} is (almost) equal to x_0 for all channels. Additionally, for convenience, it is defined that $ds_x = \overline{s}\big|_{x=L_{sea}} - \overline{s}\big|_{x=0}$ and $E = 1 - \exp\big[\frac{x_0}{L_s}\big]$. The result is

$$\eta\big|_{x=0} = \frac{3K_M Q L_s}{gB_0H^3}E + \frac{3\beta H}{8}ds_x. \tag{7.68}$$

Now, from the condition that, at $x = 0$, $\eta_{SP} = \eta_{NP}$, an expression for Q_{SP} can be derived. In this derivation it is used that $Q_{SC} = Q_{SP} + Q_{NP}$. The result is

$$Q_{SP} = \frac{\big[\frac{3\beta}{8}(H_{SP}ds_{x,SP} - H_{NP}ds_{x,NP}) + \frac{3K_{M,NP}Q_{SC}L_{s,NP}}{gB_{0,NP}H_{NP}^3}E_{NP}\big]}{\big[\frac{3K_{M,SP}Q_{SC}L_{s,SP}}{gB_{0,SP}H_{SP}^3}E_{SP} + \frac{3K_{M,NP}Q_{SC}L_{s,NP}}{gB_{0,NP}H_{NP}^3}E_{NP}\big]}. \tag{7.69}$$

In a similar way it can be derived that

$$Q_{NP} = \frac{\left[\frac{3\beta}{8}(H_{NP}ds_{x,NP} - H_{SP}ds_{x,SP}) + \frac{3K_{M,SP}Q_{SC}L_{s,SP}}{gB_{0,SP}H_{SP}^3}E_{SP}\right]}{\left[\frac{3K_{M,SP}Q_{SC}L_{s,SP}}{gB_{0,SP}H_{SP}^3}E_{SP} + \frac{3K_{M,NP}Q_{SC}L_{s,NP}}{gB_{0,NP}H_{NP}^3}E_{NP}\right]}. \tag{7.70}$$

From these two equations, an approximation for $\frac{Q_{SP}}{Q_{NP}}$ can be obtained. The result is

$$\frac{Q_{SP}}{Q_{NP}} = \frac{\left[\frac{3\beta}{8}(H_{SP}ds_{x,SP} - H_{NP}ds_{x,NP}) + \frac{3K_{M,NP}Q_{SC}L_{s,NP}}{gB_{0,NP}H_{NP}^3}E_{NP}\right]}{\left[\frac{3\beta}{8}(H_{NP}ds_{x,NP} - H_{SP}ds_{x,SP}) + \frac{3K_{M,SP}Q_{SC}L_{s,SP}}{gB_{0,SP}H_{SP}^3}E_{SP}\right]}. \tag{7.71}$$

Acknowledgements

Finally, I would like to thank Huib de Swart for guiding and advising me during the project. It was nice to have the opportunity to ask a lot of questions and I learned a lot from him. Also, I like to thank Jinyang Wang for kindly providing me with results of his model and missing information on the Yangtze Estuary.

Bibliography

https://www.merriam-webster.com/dictionary/diffusion%20coefficient, accessed: 2019-07-10, last updated: unknown.

http://www.mit.edu/course/1/1.061/www/dream/SEVEN/SEVENTHEORY.PDF, accessed: 2019-07-10, last updated: unknown.

Alebregtse, N., and H. de Swart, Effect of river discharge and geometry on tides and net water transport in an estuarine network, an idealized model applied to the yangtze estuary, *Continental Shelf Research*, *123*, 29 – 49, doi:10.1016/j.csr.2016.03.028, 2016.

Bourrichon, File:columbia estuary map-fr.svg, https://commons.wikimedia.org/wiki/File:Columbia_estuary_map-fr.svg, accessed: 2019-07-05, last updated: 2017-03-16, at 15:05.

Burchard, H., and R. D. Hetland, Quantifying the contributions of tidal straining and gravitational circulation to residual circulation in periodically stratified tidal estuaries, *Journal of Physical Oceanography*, *40*(6), 1243–1262, doi:10.1175/2010JPO4270.1, 2010.

Cameron, W., and D. Pritchard, Estuaries. In M.N. Hill (ed.), *The Sea*, *2*, 306 – 324, John Wiley and Sons, New York, 1963.

Chant, R. J., and R. E. Wilson, Secondary circulation in a highly stratified estuary, *Journal of Geophysical Research: Oceans*, *102*(C10), 23,207–23,215, doi:10.1029/97JC00685, 1997.

Chen, W., Dynamics of currents and sediment in estuaries with different density stratifications, Ph.D. thesis, Institute for Marine and Atmospheric reseatch Utrecht (IMAU) Utrecht University, 2018.

Cushman-Roisin, B., and J.-M. Beckers, *Introduction to Geophysical Fluid Dynamics, Physical and Numerical Aspects (International Geophysics Volume 101)*, second ed., Academic Press, 2011.

Dörrbecker, M., File:shanghai landsat-7 2005-08-15.jpg, https://commons.wikimedia.org/wiki/File:Map_of_the_annual_average_discharge_of_Rhine_and_Maas_2000-2011_(EN).png, accessed: 2019-06-30, last updated: 2017-04-06, at 19:01.

Dyer, K. R., *Estuaries: a physical introduction*, second ed., John Wiley & Son, Chichester, 1997.

Geyer, W. R., *Estuarine salinity structure and circulation*, p. 12–26, Cambridge University Press, doi:10.1017/CBO9780511676567.003, 2010.

Geyer, W. R., and P. MacCready, The estuarine circulation, *Annual Review of Fluid Mechanics*, *46*, 175–197, doi:10.1146/annurev-fluid-010313-141302, 2014.

Gill, A. E., *Atmosphere-Ocean Dynamics (International Geophysics Series Volume 30)*, Academic Press, 1982.

Guha, A., and G. A. Lawrence, Estuary classification revisited, *Journal of Physical Oceanography*, *43*(8), 1566–1571, doi:10.1175/JPO-D-12-0129.1, 2013.

Hansen, D. V., and M. Rattray, Junior, Gravitational circulation in straits and estuaries, *Journal of Marine Research*, *23*, 104–122, 1965.

Huijts, K., H. Schuttelaars, H. E. de Swart, and C. Friedrichs, Analytical study of the transverse distribution of along-channel and transverse residual flows in tidal estuaries, *Continental Shelf Research*, *29*, 89–100, doi:10.1016/j.csr.2007.09.007, 2009.

Jiang, C., J. Li, and H. E. de Swart, Effects of navigational works on morphological changes in the bar area of the yangtze estuary, *Geomorphology*, *139-140*, 205 – 219, doi:10.1016/j.geomorph.2011.10.020, 2012.

Kärnä, T., A. M. Baptista, J. E. Lopez, P. J. Turner, C. McNeil, and T. B. Sanford, Numerical modeling of circulation in high-energy estuaries: A columbia river estuary benchmark, *Ocean Modelling*, *88*, 54 – 71, doi:10.1016/j.ocemod.2015.01.001, 2015.

Lambert, D., and D. Group, *The Field Guide to Geology*, new ed., Checkmark Books, 2007.

MacCready, P., Toward a unified theory of tidally-averaged estuarine salinity structure, *Estuaries*, *27*(4), 561–570, 2004.

MacCready, P., Estuarine adjustment, *J. Phys. Ocean.*, *37*(8), 2133–2145, doi:10.1175/jpo3082.1, 2007.

McCarthy, R. K., Residual currents in tidally dominated, well-mixed estuaries, *Tellus A: Dynamic Meteorology and Oceanography*, *45*(4), 325–340, doi:10.3402/tellusa.v45i4.14896, 1993.

Monismith, S. G., J. R. Burau, and M. T. Stacey, Stratification dynamics and gravitational circulation in northern san francisco bay, 1996.

Munk, W., and E. Anderson, Notes on a theory of the thermocline, *Jour Marine Res*, *7*(3), 276–295, 1948.

NASA, File:shanghai landsat-7 2005-08-15.jpg, `https://commons.wikimedia.org/wiki/File:Shanghai_Landsat-7_2005-08-15.jpg`, accessed: 2019-06-30, last updated: 2019-03-16, at 17:23.

Navionics, Navionics chartviewer, `https://webapp.navionics.com/?lang=en#boating@7&key=_tz_EowycV`, accessed: 2019-06-15, last updated: unknown.

Savenije, H. H. G., A one-dimensional model for salinity intrusion in alluvial estuaries, *Journal of Hydrology*, *85*, 1986.

Savenije, H. H. G., Predictive model for salt intrusion in estuaries, *Journal of Hydrology*, *148*(1-4), 203 – 218, doi:10.1016/0022-1694(93)90260-G, 1993.

Savenije, H. H. G., Salinity and tides in alluvial estuaries, second ed., pp. 145, 155, Delft, version 2.4–2.5, accessible via: `https://hubertsavenije.files.wordpress.com/2016/12/salinityandtides2_53.pdf`, 2012.

Simpson, J. H., J. Brown, J. Matthews, and G. Allen, Tidal straining, density currents, and stirring in the control of estuarine stratification, *Estuaries*, *13*(2), 125—132, doi:10.2307/1351581, 1990.

Sun, T., Z. Yang, Z. Shen, and R. Zhao, Environmental flows for the yangtze estuary based on salinity objectives, *Communications in Nonlinear Science and Numerical Simulation*, *14*(3), 959–971, doi:10.1016/j.cnsns.2007.10.006, 2009.

Uncles, R. J., R. C. A. Elliott, and S. A. Weston, Dispersion of salt and suspended sediment in a partly mixed estuary, *Estuaries*, *8*(3), 256–269, doi:10.2307/1351486, 1985.

Valle-Levinson, A., *Definition and classification of estuaries*, pp. 1—11, Cambridge University Press, doi:10.1017/CBO9780511676567.002, 2010.

Valle-Levinson, A., *Classification of Estuarine Circulation.*, vol. 1, pp. 75–86, Academic Press, doi:10.1016/B978-0-12-374711-2.00106-6, 2011.

Webster, M., Saltwater invasion, https://scienceline.org/2007/06/env_webster_salt-water-global-warming/, accessed: 2019-06-30, date of publication: 2017-06-22.

Wei, X., M. Kumar, and H. M. Schuttelaars, Three-dimensional salt dynamics in well-mixed estuaries: Influence of estuarine convergence, coriolis, and bathymetry, *Journal of Physical Oceanography*, *47*, 1843–1871, doi:10.1175/JPO-D-16-0247.1, 2017.

Weisstein, E. W., "leibniz integral rule." from mathworld–a wolfram web resource., http://mathworld.wolfram.com/LeibnizIntegralRule.html, accessed: 2019-03-06, last updated: 2019-02-11.

Winant, C. D., Three-dimensional tidal flow in an elongated, rotating basin, *Journal of Physical Oceanography*, *37*(9), 2345–2362, doi:10.1175/jpo3122.1, 2007.

Zhang, E., H. H. Savenije, H. Wu, Y. Kong, and J. Zhu, Analytical solution for salt intrusion in the yangtze estuary, china, *Estuarine, Coastal and Shelf Science*, *91*, 492–501, doi:10.1016/j.ecss.2010.11.008, 2011.

Zhu, J., H. Wu, L. Li, and C. Qiu, Saltwater intrusion in the changjiang estuary, in *Coastal Environment, Disaster, and Infrastructure - A Case Study of Chinas Coastline*, IntechOpen, doi:10.5772/intechopen.80903, 2018.

Zhu, P. . Z. L. . W. H. . C. H., J. Ding, *Influence of the Deep Waterway Project on the Changjiang Estuary*, pp. 79—-92, Springer, doi:10.1007/1-4020-3655-8_6, 2006.